SCUOLA DI DOTTORATO
UNIVERSITÀ DEGLI STUDI DI MILANO-BICOCCA

Dipartimento di / Department of MATERIALS SCIENCE

Dottorato di Ricerca in / PhD program MATERIALS SCIENCE AND NANOTECHNOLOGY
Ciclo / Cycle XXXVIII

DESIGN OF HYBRID PLASMONIC NANOPORES FOR ENGINEERED ELECTROMAGNETIC FIELD CONFINEMENT

Cognome / Surname **Sapunova** Nome / Name **Anastasiia**

Matricola / Registration number **906936**

Tutore / Tutor: PROF. SERGIO BROVELLI

Supervisor: PROF. DENIS GAROLI

Coordinatore / Coordinator: PROF. FRANCESCO CIMBRO MATTIA MONTALENTI

ANNO ACCADEMICO / ACADEMIC YEAR 2024/2025

Abstract

This work presents a multiphysical study of processes in three-dimensional plasmonic and magneto-plasmonic nanopores. The distribution of the electromagnetic field, photothermal effects, ion transport, and the dynamics of nanoscale objects within nanopores were investigated in detail.

The influence of nanopore geometry on the rectification of ion current, localization of plasmon modes, and distribution of the electromagnetic field has been studied. The simulation of plasmonic and hybrid Au/Si nanopores has been performed, and the photothermal effects arising from the absorption of electromagnetic radiation by the metallic part of the structure have been investigated.

To analyze the enhancement of fluorescence in 3D plasmonic nanopores, we calculated the change in the overall decay rate of dipole radiation near a metal surface. We found that there is an optimal distance between the fluorophore and the plasmonic surface, determined by the balance between local field enhancement and non-radiative losses.

The main part of the work is devoted to the study of a magneto-plasmonic trap for Fe_3O_4@Au nanoparticles in a magneto-plasmonic nanopore. A multiphysics approach was implemented, combining calculations of the electromagnetic field distribution, optical and magnetic traps, plasmonic heating, thermophoretic effects, and particle dynamics.

It has been shown that the stability of the capture is determined by the competition between optical force, magnetic force, viscous resistance, and thermophoretic transport, and an increase in laser power can lead to thermophoretic destabilization of the capture mode. These results expand our understanding of plasmonic and magnetoplasmonic nanoporous systems and can be used in the development of nanopore-based biosensors, nanofluidic devices, and systems for controlled capture of nanoscale objects.

Acknowledgments

I would like to express my gratitude to all those who have been by my side throughout this time. My colleagues, friends, family, and favorite ones – each of you is unique and has made an incredible contribution to this work. Your support has been invaluable, your experiences have motivated me every day, and your joy for living has allowed me to keep going after every setback.

Спасибо!

Contents

Table of figures

1. Introduction

1.1 Nanopores for nanoscale transport and manipulation

Typically, when we talk about nanopores, it often refers to a nanoscale hole which is between 1 and 100 nm in size (Figure 1) [1]. These tiny pores, which have become a topic of great scientific interest among many other nanoscale structures, are characterized by their primary ability to transport nanoscale objects for applications in a wide range of fields, including the light-matter interaction under nanoscale[2], ionic current rectification[3], single molecule detection[4], sensing[5] and many others.

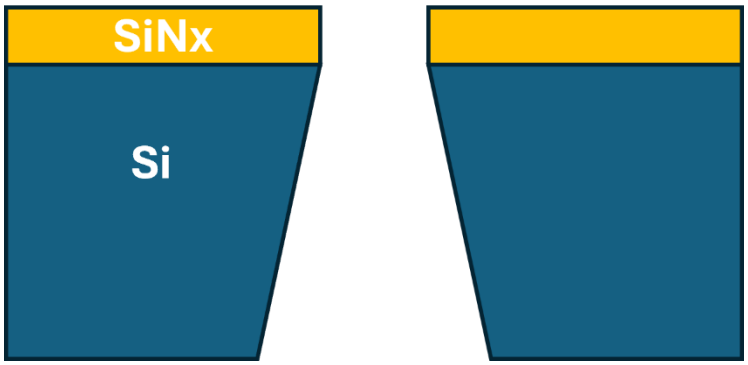

Figure 1 Solid state nanopore

At the macroscopic level, fluid motion and transport of the objects are usually described by classical hydrodynamics[6]. At the nanoscale, however, the situation becomes more complex: in addition to bulk properties of the medium, a significant role is played by interactions at the interfaces between different materials. This gives rise to distinct transport mechanisms that do not appear in larger-scale systems.

Initially, systems resembling nanopores, were first discovered and studied in biological systems, as they perform functions such as the selective transport of ions and molecules[1]. For example, the membranes of cells, organelles, and other biological structures consist of nanoscale channels that maintain physiological conditions, transmit signals, and perform various functional tasks[1]. These naturally occurring systems are characterized by high efficiency and selectivity in transport, which has inspired scientists to develop artificial nanopores.

Thus, nanopores are divided into two main categories (Figure 2): *biological* and *solid-state*[7]. Biological nanopores are represented by protein channels in lipid membranes for selective transport of ions and molecules[8]. Their notable selectivity and sensitivity contribute to their widespread use in molecule sequencing and recognition. However, biological nanopores are also limited by their low mechanical stability, sensitivity to external conditions, and limited control over their geometry and properties[9]. The development of nanotechnologies has made it possible to create artificial nanopores with specified geometry, materials, and functional properties.

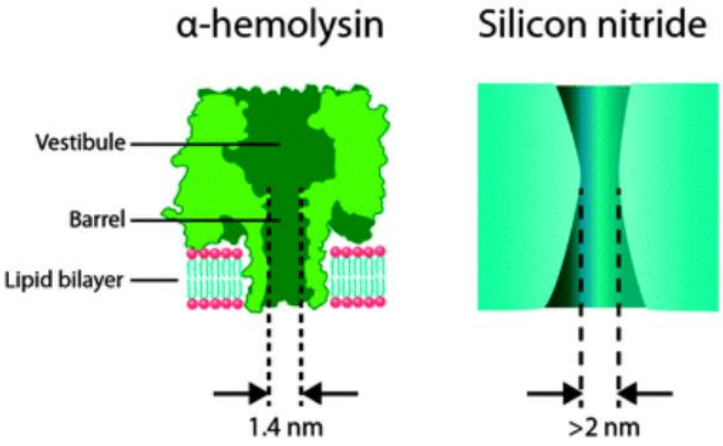

Figure 2 Comparison of biological α-hemolysin nanopores and solid-state silicon nitride nanopores used for nanopore sensing applications[10]

In opposite with biological nanopores, solid-state nanopores, as mentioned earlier, made by nanofabrication, allow to create more customizable and manageable systems. Typically, the materials that make up solid-state nanopores are silicon, dielectrics, and metals, and the channel geometry is often cylindrical, but it can be any and varies depending on the purpose of using the nanopores[11]. These properties have opened up opportunities for a comprehensive study of the effect of nanopore parameters on transport processes for the development of devices with specified functional characteristics[12].

One of the key advantages of solid-state nanopores lies in their ability to be integrated with additional physical effects[13]. While biological nanopores have limited functionality, solid-state nanopores can be designed in such a way that it is possible to use more than just one mechanism to control transport inside the channel. These mechanisms usually include electrical, optical, and

magnetic effects[14]. These properties make nanopores a promising platform for the study of hybrid nanostructures with a wide range of applications at the nanoscale.

Another main characteristic of nanopores is that the transport of investigating objects significantly depends on the properties of the nanopore walls surface. Often, the diameter of the channel is comparable to the characteristic lengths of interparticle interactions, therefore, the influence of such forces as the Coulomb interaction, Van der Waals forces, as well as hydrophilic and hydrophobic effects are critically determining[15]. In this case, it is extremely necessary to take into account the complexity of interaction between the object of study inside the pore and its surface.

Transport through nanopores occurs via several fundamental mechanisms: diffusion, drift driven by an external electric field, and convective flow[16]. However, at the nanoscale, these processes turn out to be highly interconnected. Thus, the distribution of ion concentrations critically affects the local electric field, which, at the same time, is a mechanism that determines the movement of charged particles. Thus, transport in nanopores is a complex process that is sensitive to geometry, material, and external conditions.

The charge of the nanopore surface is a key parameter that directly determines the interaction of ions with the channel walls[17] (Figure 3). It leads to the formation of an electric double layer consisting of fixed charges on the surface of the pore and counterions compensating them in the adjacent solution[18]. Despite the fact that the thickness of the double layer (or in other words, the Debye length) is small on a macroscopic scale, but in nanopores it can be comparable to the channel size. These conditions significantly affect the ion distribution inside the pore and lead to its asymmetry.

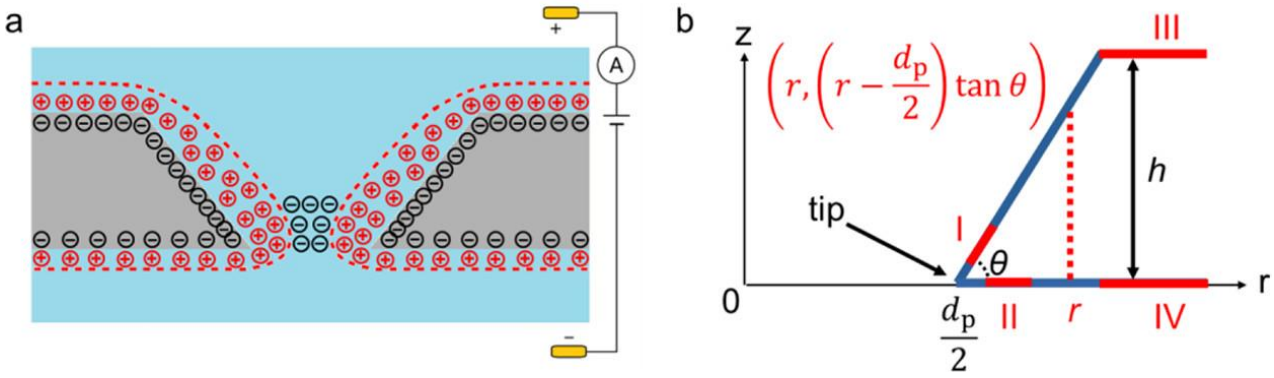

Figure 3 Model for the truncated-conical nanopore. (a) Schematic net charge distribution on the surface with the nanopore membrane immersed in an aqueous solution (electrolyte) when a positive bias voltage is applied. (b) Cylindrical coordinates (r, z) for the nanopore, where h is the thickness of the membrane, θ is the angle of the sloped sidewall, and d_p is the diameter of the smaller opening of the nanopore[19]

The above-mentioned effects lead to ion selectivity, current asymmetry, and a nonlinear dependence of conductivity on the applied voltage. One of the most well-known effects is the ionic current rectification (ICR), which is characterized by the fact that the current passing through the pore directly depends on the direction of the applied potential[20]. The main parameters forming this phenomenon are a combination of geometric asymmetry and an uneven distribution of charges inside the channel[21].

Transport sensitivity within the pore can be strongly influenced by external factors, including optical excitation[22] (Figure 4). By illuminating metallic or metallized nanostructures with a certain wavelength, it is possible to induce the excitation of localized surface plasmons, and, as is already well known, this physical effect leads to an increase in the electromagnetic field near the pore[23]. This gain, in turn, can affect both charge distribution and local temperatures due to optical absorption.

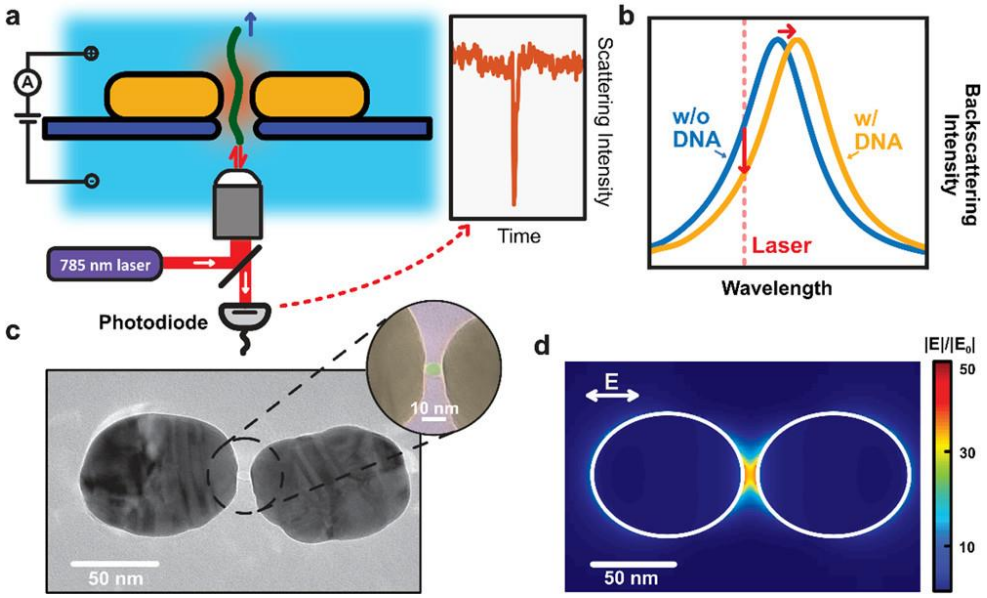

Figure 4 Plasmonic nanopores for single-molecule optical sensing. (a) Schematic side-view of electrophoretically driven DNA translocation through a plasmonic nanopore detected via optical backscattering from the plasmonic antenna. (b) DNA sensing principle. (c) TEM image of the plasmonic nanopore device. (d) Simulated electromagnetic field distribution for longitudinal excitation at 785 nm[24]

Optical absorption in metal layers leads to energy dissipation and intense local heating of the structure. In nanopores, this heating is highly localized, since due to the geometry of the pores, the maximum energy density of the field is concentrated near the edges and walls of the pore[25]. An increase or decrease in temperature critically affects the transport properties of the system, changing the mobility of ions, the viscosity of the medium and the concentration distribution[26]. Thus, temperature effects become an integral part of the description of nanofluidic processes.

These and other processes occurring in nanopores make it possible to develop new functional devices capable of performing complex tasks of transport control, sensing and signal processing at the level of individual particles and molecules.

One of the most popular and sought-after applications of nanopores is biosensing, where nanopores are used as a device for detecting biomolecules, including proteins, DNA and RNA[27]. The basic principle of operation is to register the change in ICR as the molecule passes through the channel.

This makes it possible to identify individual objects, which is why nanopores are known for their high sensitivity for medical diagnostics and biological research[1].

Any discussion of DNA and RNA would be incomplete without considering DNA and RNA sequencing, which is indeed one of the key applications of nanopores (Figure 5). Sequencing is performed by passing a nucleic acid molecule through a nanopore, while an external electric field is applied to the pore[28]. Thus, it becomes possible to evaluate differences in the ion current signal and detect individual nucleotides.

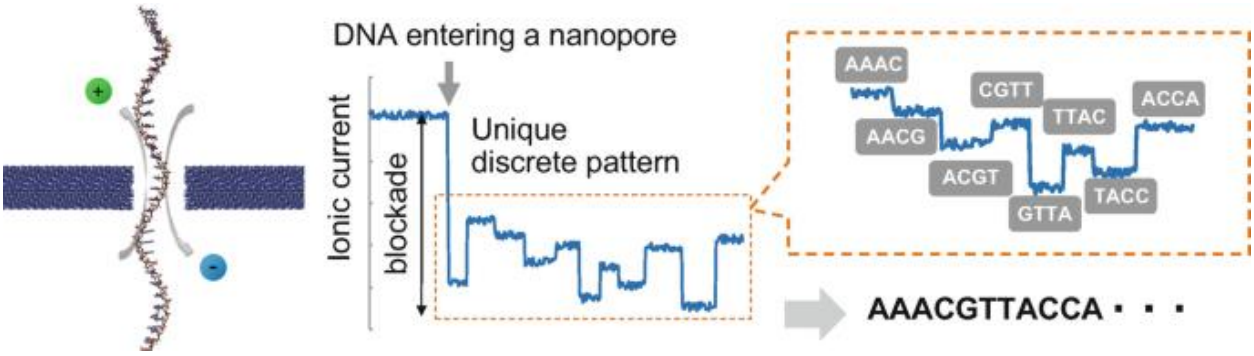

Figure 5 Schematic concept of the sensing mechanism for the ionic blockade current from nanopore DNA sequencing. When a DNA molecule is driven through a nanopore, the steady ionic current flux is blocked by the geometric exclusion due to DNA. Since this blockade depends on a sequence of several nucleotides, the DNA translocation generates unique discrete patterns. The original DNA sequence can be determined by deciphering the ionic current pattern[29]

Nanopores are widely used for the detection[30] and analysis[31] of nanoparticles and the study of their properties. As the particle moves through the pore, the recorded electrical signal changes, making it possible to determine the particle size, shape, and concentration[32]. This property makes it possible to use nanopores for environmental monitoring[33], analysis of colloidal systems[34], and development of new nanomaterials[35–37]. Moreover, nanopores are also used for filtration and separation of substances[38], desalination of water[39], energy storage[40], as well as nanoreactors[41], which emphasizes their versatility and technological importance.

The most important and most attractive feature of nanopores is their size, which is often comparable to the size of individual molecules (about a few nanometers). In this case, the transport

of molecules through the pore becomes strictly discrete: at a certain point in time, either one molecule or none passes through the nanopore[42]. This fundamental difference makes nanopores a unique sensor, unlike macroscopic systems, where the average flow of a large number of particles is measured.

During the passage of a single molecule through the pore opening, there is a rapid change in the ionic current flowing through the channel[43]. These changes have a specific characteristic and are critically dependent on the properties of the molecule (size, charge, and structure)[43]. This property allows for the detection of events at the single particle/molecule level. As a result, the signal is not averaged over an ensemble but rather reflects the behavior of a specific molecule of interest.

The high sensitivity of nanopores is caused by surface effects and interactions at the pore-wall-fluid interface play a significant role in nanopores[1]. When the channel size is small enough to be comparable to the ion screening length, even small changes in the system can lead to instantaneous changes in transport properties. This enhances the system's response and allows for the detection of individual events with high accuracy.

In a short summary, factors such as geometric constraints, discrete transport behavior, and high sensitivity to local changes make nanopores suitable for single-molecule detection, which is a major advantage and key factor in their widespread use in modern nanotechnology.

1.2 Plasmonic field confinement in nanopores

Plasmonics

The interaction of metal nanostructures with electromagnetic radiation differs substantially from that observed in bulk materials. The main reason for this is the presence of free electron gas in metals, which can collectively respond to an external electromagnetic field at specific frequencies (or wavelengths)[44] (Figure 6). When an electromagnetic wave interacts with a metal, it drives a collective displacement of the conduction electrons with respect to the positively charged ionic background[44]. This shift results in a restoring force due to Coulomb attraction, leading to collective oscillations in the electron density[45].

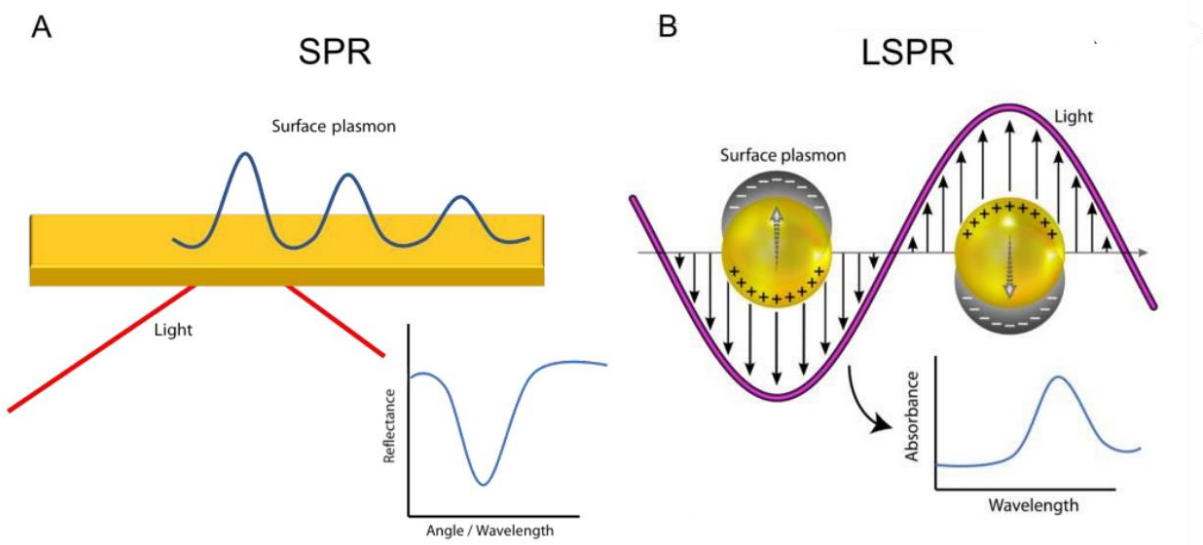

Figure 6 a) Prism coupling configuration of SPR, where a light beam impinges on a thin metallic film deposited on a prism. P-polarized light absorbed by the surface plasmon is seen from a minimum in the reflection spectra. b) Representation of the localized surface plasmon on nanoparticles and absorbance spectra obtained for binding events on nanoparticles[46]

The described oscillations are known as plasmons and are a consequence of the fundamental excitation of the electronic subsystem of the metal[47]. When these effects occur at a surface, they are usually related to propagating surface plasmons[48]. In three-dimensional structures, however, localized surface plasmons (LSPs) are formed, where the electromagnetic field is strongly confined and localized near a metallic nanostructure[48]. All these modes are of particular interest for nanopores, as they collectively enable the localization of electromagnetic energy into volumes well below the diffraction limit[49].

Resonance occurring during the interaction between a metal and electromagnetic radiation implies that, under certain conditions, energy accumulates progressively from one cycle to the next during optical excitation[50]. However, at the same time, there are mechanisms of dissipation, for example, ohmic losses in metal and losses spent on radiation. The amplitude of the local field is determined by the balance between accumulation and loss[50]. As a result, highly localized near fields with high spatial inhomogeneity are formed when excited by a resonant wavelength.

As a result, the main advantage of plasmon resonance is the strong amplification of the electromagnetic field at the metal-dielectric interface (Figure 7). This amplification is caused by

the redistribution of surface charge, which is particularly pronounced in areas with high heterogeneity or sharp transitions, such as sharp edges, vertices, and gaps and cavities between elements[51]. These areas contribute to the accumulation of induced charges, which causes the formation of extremely high electric field gradients.

Such areas, which are characterized by a high localization of the electric field, are commonly referred to as "hot spots"[52]. The main feature is that at these points the field amplitude can exceed the incident field by several orders of magnitude. When it comes to single-molecule detection, it is the spatial localization of the field, not just its amplitude, that determines the effectiveness of interaction with individual molecules or particles[52].

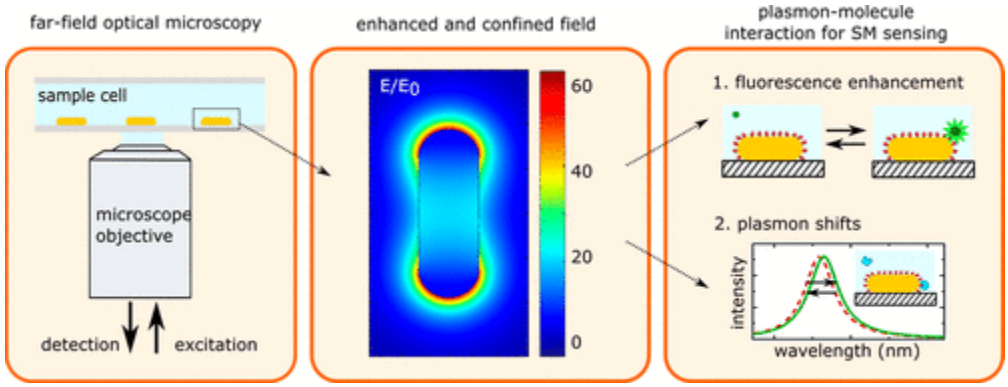

Figure 7 Principle of plasmon-enhanced single-molecule sensing using nanoparticles. (left) Far-field optical probing of individual nanoparticles. (middle) The plasmon resonance generates strongly enhanced and confined local electromagnetic fields around the particles. (right) These local fields mediate plasmon–molecule interactions, enabling single-molecule detection through plasmon-induced molecular changes (e.g., fluorescence enhancement) or molecule-induced plasmon changes (e.g., resonance frequency shifts)[53]

Plasmon enhancement occurs in metallic nanostructures is determined by the local intensity of the electromagnetic field, which is proportional to the square of the electric field amplitude $|E|^2$ [54]. At the same time, at certain wavelengths, according to the resonance conditions, the optical absorption in the metal increases, the processes of elastic and inelastic scattering intensity, and the contribution of nonlinear optical effects grows.

In experiments where plasmonic enhancement is used for Raman scattering, the signal intensity is estimated as $|E|^4$ [55]. This is the reason why plasmonics is widely used for Raman scattering, as it

dramatically increases the sensitivity of the method, as mentioned earlier[56]. As a result, this method is often used to detect signals from individual molecules near "hot spots." This is what makes plasmonic resonance in surface-enhanced Raman scattering in plasmonic nanostructures so valuable for detection applications.

At the same time, in addition to the direct enhancement, there are also processes such as increased energy absorption in the metal, which results in the dissipation of unabsorbed energy as heat, leading to significant local heating[57]. This process contributes to the formation of a thermal field that significantly influences the dynamics of nanoscale processes.

Nanopore's geometry

As mentioned above, any inhomogeneities or, in other words, the geometric features of the metal structure are one of the key factors that critically affect the characteristics of the plasmonic response and its spectral position (along with the metal material)[51]. In the case of nanopores, the size of which is significantly small, even nanometer scale changes lead to noticeable changes.

The confinement effects are directly dependent on the diameter of the nanopores, thereby affecting the spatial confinement of the field[58]. As the diameter decreases, the localization of the field within the pore and near its edges becomes stronger. This directly affects the gradients of the field, which in turn influences the interaction of light with particles/molecules or other objects near the pore entrance.

In addition to the nanopore diameter, the thickness of the metal layers plays an important role, as it also determines the conditions for the excitation of plasmon modes [59]. Depending on the intended purpose, the thickness of the layers can be adjusted to ensure the localization and efficient excitation of plasmons at specific wavelengths.

Finally, in the context of geometry, the last factor that affects the position of the plasmonic resonance is the periodicity of the structure, which determines how far apart the nano-holes are and how often they are spaced [60]. In such systems, surface and localized plasmons are excited, and their combined effects can significantly alter the position of the resonance and the distribution of the field compared to when these effects are considered separately. The periodicity can shift the plasmonic resonance and either enhance or degrade the plasmonic effects[61].

In this work (a nanopore with a diameter of 250 nm and a period of 550 nm, and a multilayer structure of Au/Co/Au/SiN), the electromagnetic field was amplified by a combination of all these mechanisms: gold as a plasmonic material, localization of the field at the edges of the pore, and collective plasmonic interaction between the array elements.

Thus, plasmonic localized enhancement of the electromagnetic field in nanopores plays an important role in creating systems for detecting and investigating processes at the nanoscale. Local field amplification increases the sensitivity of optical methods, and light absorption promotes local heating, creating a temperature gradient near hotspots. Heating directly affects properties such as particle diffusion, medium viscosity, ion transport through nanopores, particle capture, and magnetic field distribution.

In addition, the localized enhanced field affects the optical capture and manipulation of particles. In combination with a certain pore geometry, it is possible to control the movement of particles. As a result, nanopores with plasmonic properties have become a particularly attractive platform for single-molecule detection and trapping.

Optical trapping

In the context of single molecule detection, plasmonic holes are actively used as a platform for particle trapping[58]. For example, the use of highly localized electromagnetic fields helps to trap individual molecules and nanoparticles[58] (Figure 8). Conventional optical trapping is limited by the diffraction limit, while using plasmonic pores, forming hot spots, it is possible to directly affect individual molecules and particles inside the nanopore[62].

The physics of plasmonic trapping is based on the effect of an optical gradient force on an object, which occurs in a non-uniform electromagnetic field. Near the hot spots of plasmonic nanostructures, the field intensity increases dramatically, forming an enhanced electromagnetic field $|E|^2$, where a force acts to capture a nanoobject with a specific value of polarizability[62]. In the dipole interaction approximation, this force is proportional to the gradient of the field intensity $F_{opt} \sim \nabla |E|^2$, leading to the localization of particles directly within the plasmonic hot spot[62].

When considering nanopores, hot spots are usually located at the edges of the pore or between the gaps of the metal elements[60]. This is often achieved using so-called bowtie antennas[63]. Recently it

was demonstrated that these structures focus the electromagnetic field within a nanoscale volume, allowing for direct interaction with DNA molecules[64]. As a result, plasmonic forces can compete with electrophoretic transfer and even completely stop the translocation of a molecule through a nanopore.

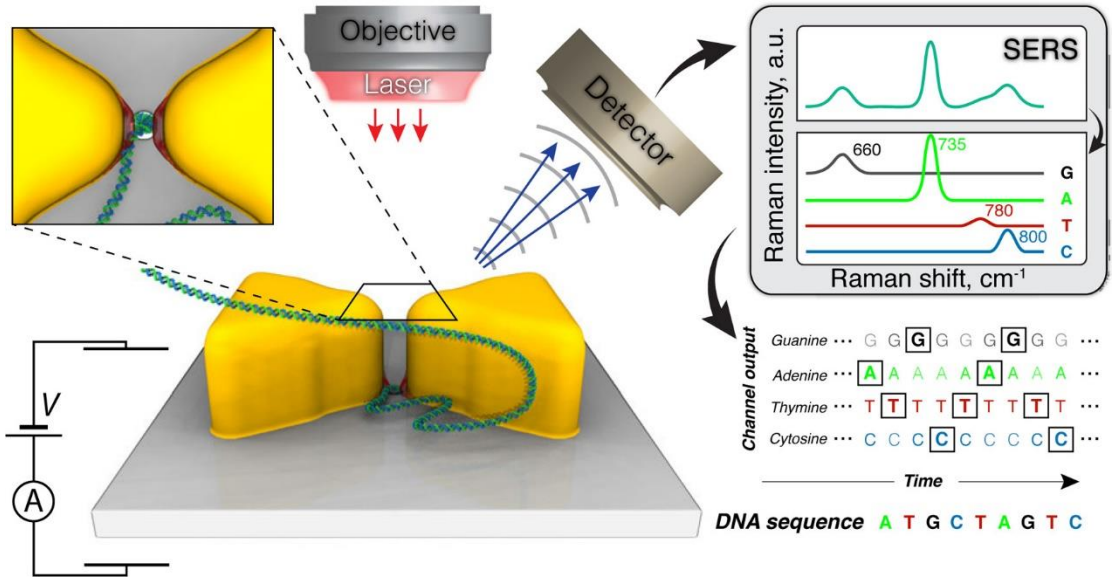

Figure 8 Plasmonic bowtie antenna–nanopore. Electromagnetic field at bowtie antenna structure with narrow gap (about a few nanometers) controls DNA translocation velocity, enhances optical signal of DNA and fabricates self-aligned nanopores[64]

Thus, using plasmonic nanopores, translocation can be suppressed or even stopped[64]. Without plasmonic excitation, DNA moves uncontrollably at high speed through the nanopore and is mainly determined by the applied electric field. Due to plasmonics, local optical forces attract the molecule to the region of maximum intensity of the EM field, leading to a sharp decrease in the speed of movement or even a potential complete stop[64].

One of the other applications of plasmon trapping is the discrete (stepwise) movement of molecules. Working in the on and off mode of the plasmonic enhancement, like the operation of a switch, the phases of capture and free movement of the molecule/particle alternate. In this application, the object moves through the nanopore stepwise, with the ability to control the step, which is set by field parameters and manual modulation of the laser signal[64]. This mode is especially important for sequencing, as it allows for sequential exposure of different sections of the molecule in the detection zone.

Unlike conventional optical traps, in plasmonic nanopores it is possible to trap the molecule/particle directly near the surface of the pore, in the area where the EM field is maximally amplified. The formation of such nanocavities, where the particle is trapped between the metal layers of the structure, contributes to the achievement of extreme field amplification, which significantly increases the sensitivity of optical methods such as fluorescence[65] or SERS[66,67].

Plasmonic trapping using nanopores has many advantages. Firstly, it increases the molecule's residence time in the detection region, which is critically important for improving the signal-to-noise ratio[68]. Secondly, the molecule/particle is localized in a certain predictable area of the field, increasing the reproducibility of measurements. Finally, due to the enhanced field in hot spots, the optical signal from the molecule is amplified several times, allowing the implementation of single-molecule spectroscopy methods[58].

As it was mentioned earlier, illumination of plasmonic materials is often accompanied by effects as heating and thermophoresis[69,70]. The absorption of light in metal layers leads to temperature gradients that can affect the movement of molecules and particles. Sometimes it helps to strengthen the trapping, while in other cases it leads to additional stochastic movement[71]. Thus, the behavior of the system is dictated not only by optical forces, but also by thermohydrodynamic processes.

Despite the abundance of benefits, plasmon trapping has a number of limitations. Thermal fluctuations are so significant that they limit the capture efficiency, especially for small particles and molecules. Moreover, a highly intense EM field can lead to structural changes in biomolecules and intense heating of the medium, which is crucial for biomolecules. Nevertheless, varying the parameters of the geometry of the nanostructures and optical excitation makes it possible to optimize the system and reduce undesirable effects, realizing stable trapping at the nanoscale.

1.3 Ionic current rectification in nanopores

The ion transport at the macroscale and microscale differs fundamentally in that the nanoscale hole through which the ion flow passes is often comparable in size to the scale of interionic interactions or the Debye length, that is, the length at which the electric field is shielded due to the effect of redistribution of surrounding ions[72]. An important role is played by the surface charge, as well as the electric double layer (EDL) formed on the walls of the nanopore when the electrolyte interacts with the charged surface of the pore, and this leads to such an interesting phenomenon as ion

current rectification (ICR)[72]. ICR is a direct consequence of the asymmetric current response to the applied voltage to the nanopore.

During measurements, ICR looks like a nonlinear and asymmetrical volt-ampere characteristic I(V), often similar to what occurs when measuring I(V) of a semiconductor diode[73]. In other words, the current passing through the nanopore behaves differently at a positive voltage of a certain amplitude from the current at a negative voltage, but with the same amplitude[74]. The main condition determining the degree of rectification is the asymmetry of the nanochannel in the system in combination with EDL on the walls[75] (Figure 9).

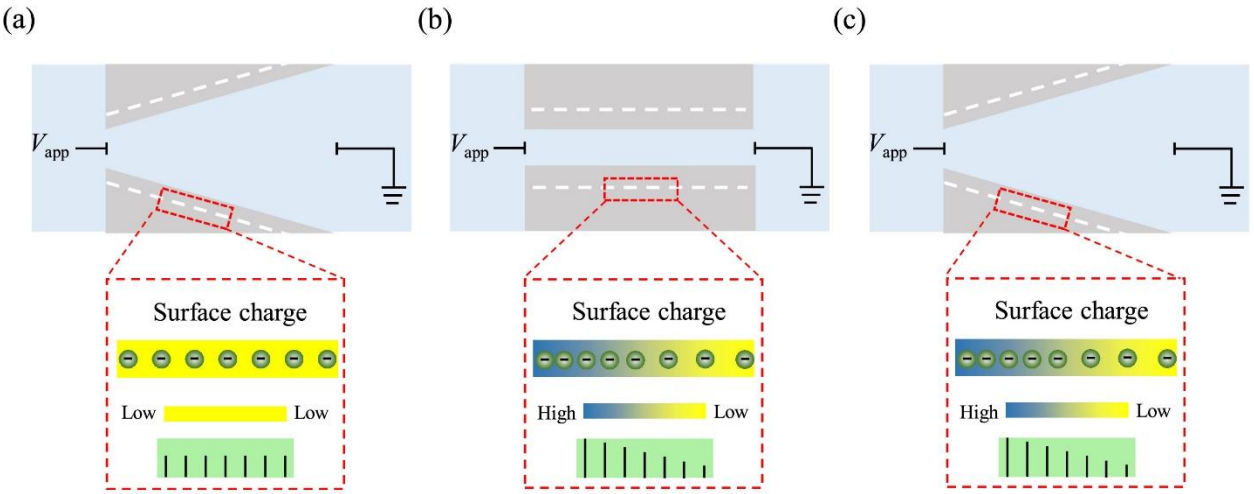

Figure 9 The diagram of (a) homogeneous charged conical nanochannel, (b) non-homogeneous charged cylindrical nanochannel and (c) coupling asymmetric charged nanochannel[75]

Thus, the degree of rectification (RR) is determined by the ratio of the measured current at a positively applied voltage to the current measured at a negative one:

$$RR = \frac{I_{forward}}{I_{reversed}} \qquad (1)$$

As can be seen from Figure 9, for symmetrical cylindrical nanopores, the degree of rectification is usually about 1. Strongly asymmetric pores (for example, conical ones) exhibit values in the range of 10-100[76].

The description of ionic current in nanopores, where ions are provided in a solution of electrolytes in the volume of the nanopore, is standardly described by the Poisson-Nernst-Planck (PNP) and Navier-Stokes (NS) equations[77]. These equations describe the electric potential, the flow of ions and liquids in the system. The solution of this system of equations allows to see the distribution of ions inside the nanopore, as well as to determine the degree of rectification of ionic current.

$$\vec{J}_i = -D_i \nabla c_i + \frac{z_i F}{RT} D_i c_i \nabla \varphi + c_i \vec{u} \tag{2}$$

$$\nabla^2 \varphi = -\frac{F}{\varepsilon} \sum_i z_i c_i \tag{3}$$

$$\rho \left(\frac{\partial \vec{u}}{\partial t} + (\vec{u} \cdot \nabla) \vec{u} \right) = -\nabla p + \mu \nabla^2 \vec{u} - F \nabla \varphi \sum_i z_i c_i \tag{4}$$

$$\nabla \cdot \vec{u} = 0 \tag{5}$$

In these equations $\vec{J}_i$ denotes as the ion flux, D_i is the diffusion coefficient, c_i is the ion concentration, z_i is the ion valence, F is ну the Faraday constant, R is the universal gas constant, T is the temperature, φ is the potential, ε is the dielectric constant of medium, ρ is the fluid density, μ is the viscosity of electrolyte solution and $\vec{u}$ is the fluid velocity, p is the pressure[78].

As mentioned earlier, EDL is critical when it comes to ICR. The surface-charged walls of the nanopore attract counterions and repel ions of the same sign as those on the pore walls, resulting in a redistribution of charges near the pore walls. This leads to a highly concentrated distribution of ions near the pore walls, which differs significantly from the bulk solution[79].

In addition to the surface charge, an asymmetry condition is required, which is achieved by forming a certain geometry (for example, a conical pore), or by forming an inhomogeneous charge distribution. Often, the shape of the pores is conical, since its radius varies along the length, which

directly leads to a spatially inhomogeneous distribution of the electric field and ion concentration[79] (Figure 10).

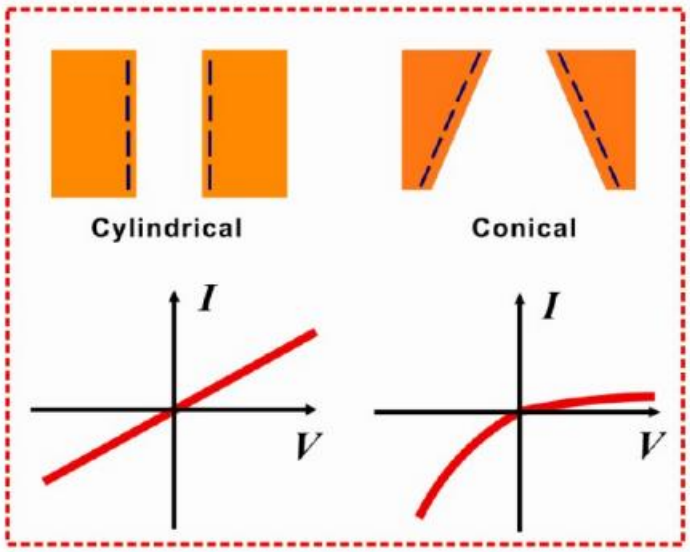

Figure 10 Linear I(V) behavior is found in cylindrical nanopores, even if they bear surface charge, but diode-like I(V) behavior is found in charged conical nanopores[79]

The physical phenomenon of ICR can be described by a model of ion accumulation and depletion[80]. Thus, if a conical nanopore with a negative charge and a KCl electrolyte solution is considering, when a negative voltage is applied to the inner electrode, the cations move inside the pore, while the anions begin to move in the opposite direction. With negatively charged walls, the anions are repelled and their movement is suppressed. In this case, cations accumulate inside the pore, and the total ion concentration increases, increasing the conductivity and increasing the current, respectively[77].

By changing the voltage polarity, the ion distribution and rectification change. When the applied voltage is positive, the cations tend to leave the channel, and the anions, on the contrary, try to enter it, but at the same time experience resistance from the walls[81]. As a result, the channel is depleted of charge carriers, which means a decrease in conductivity and a decrease in current, respectively. Thus, the same system can be counted to work in two modes. One of the modes leads to charge accumulation and is highly conductive, and the other to depletion, which gives an asymmetry in the volt-ampere characteristics[81].

Thus, the accumulation and depletion modes affect not only the electric current, but also the associated transfer processes. A change in the charge concentration leads to a modification of the electroosmotic flow formed during the movement of ions in the electric double layer[82]. Thus, the hydrodynamic response of the system depends on the ion transport mode, thereby enhancing the asymmetry of behavior during voltage polarity reversal.

Another factor that significantly influences the behavior of the system is temperature. Since the ion distribution in the EDL depends on the balance of thermal motion and electrostatic interaction, the temperature gradient can change the ion distribution[83]. First of all, this affects ion mobility, diffusion coefficient, and EDL thickness, changing the conductivity of the nanopore[84]. For example, in the accumulation mode, an increase in temperature contributes to faster ion transfer, and in the depletion mode, temperature contributes to a decrease in the amount of charge carrier concentration and a greater sensitivity of the system to thermal fluctuations.

Thus, ICR in nanopores is formed mainly due to the surface charge of the channel and its geometry, ion distribution, and the surrounding electric field. As a result, the local conductivity of the pore changes due to the redistribution of charge carriers, which facilitates the transition between high and low conductivity modes when the voltage is reversed.

1.4 Magnetic trapping in nanopores

As mentioned earlier, plasmonic nanopores, characterized by high localization of the EM field due to the excitation of surface plasmons, exhibit extreme field amplification and are a powerful tool for single-molecule spectroscopy, detection, and analysis of biomolecules. However, despite their numerous advantages, a significant limitation remains the lack of control over particle dynamics. For example, molecules and nanoparticles pass through the channel so quickly that the interaction time with the amplified EM field is limited, resulting in reduced measurement accuracy[58].

Due to this, much interest has been devoted to the development of possible methods for controlling the motion of particles near nanopores. One of the most promising methods is magnetic field control, as it is not affected by EDL and is effective even in highly concentrated electrolyte solutions. Another significant advantage over optical methods is that magnetic forces do not require high-intensity fields and do not directly affect the motion of ions. The magnetic force

implements a force effect without significantly changing the thermodynamic state of the system, providing a more controlled effect on the particles[85].

Another benefit of this trapping method is its scalability for magnetic control. Magnetic fields can be easily set by external sources, and external changes in the experimental conditions do not require modification of the nanostructure, whereas in plasmonic systems, the trapping conditions are explicitly defined by the geometry and illumination conditions. This allows for real-time reconfiguration of the trapping and transport conditions[85].

Finally, the main advantage of magnetic control is that this method can be easily and effectively combined with other physical mechanisms (electrical and optical). Thus, in hybrid systems, the magnetic field is usually used as a mechanism for stabilizing the position of a particle, and the optical field for its non-natural detection and excitation. This separation of functions helps to create more controlled multiphysical platforms for biosensing.

From a physical point of view, the magnetic trapping force is determined by the magnetic energy gradient[86]. For particles with an induced magnetic moment, the force is proportional to the gradient of the square of the magnetic induction, which leads to the attraction of the particle in the region with a maximum value of B^2. In cases with optical forces, where the capture is directly related to the field intensity $|E|^2$, the magnetic capture force is determined by the spatial heterogeneity of the magnetic field[87]. Therefore, the main condition for effective control of particle capture is the formation of strong local gradients.

For example, a similar effect can be achieved by integrating ferromagnetic materials directly into the nanopore structure. Thus, it was shown that a thin cobalt layer in a multilayer Au/Co/Au structure leads to the formation of a magnetic field gradient, and regions with high magnetic energy density appear at the edges of the pore[88] (Figure 11). These areas act as nanoscale magnetic traps, spots where potentially the particle can be trapped with high precision. Calculations confirm that in such systems the magnetic field gradients reach values of 10^8 T/m, which contributes to the occurrence of forces up to tens of piconewtons for very small particles of the order of 10 nm[88]. Such values significantly exceed the forces acting on nanoparticles in hybrid magneto-plasmonic traps, opening up the possibility of trapping particles near the nanopore.

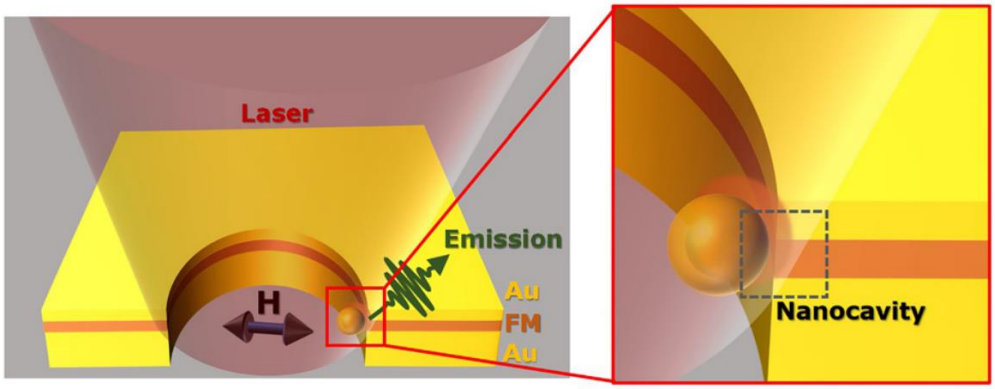

Figure 11 Left panel: geometry of the proposed experiment: a nanopore made of Au[5 nm]/Co[5 nm]/Au[100 nm] immersed in water is illuminated with a laser at 780 nm. A magnetic core–shell (Fe_2O^3-Au) nanoparticle is trapped due to the efficient force induced by the magnetic building block after the application of a static magnetic field H. Right panel: zoom on the nanoparticle-nanopore gap (magneto-plasmonic nanocavity)[88]

One of the main advantages of magnetic trapping compared to other methods is the ability to dynamically control particles. By changing the external magnetic field, the distribution of magnetization in the ferromagnetic layer can be controlled, allowing for the movement of local minima in the magnetic potential. This technique enables the manipulation of particle motion along the pore boundary or the alternation of retention and release[88]. This functionality is particularly useful for controlled interactions between particles and localized regions of enhanced field.

In addition to particle trapping and retention, magnetic nanopores have a number of other applications in the context of particle trapping.

Figure 12 Applications of magnetic trapping in nanopores

As it can be seen from Figure 12, magnetic traps can slow down the movement of particles or (possibly) stop them near the pore, reducing the speed at which particles pass through the pore. This property provides more time for the particle to interact with the detection region, which has a significant impact on sequencing and optical spectroscopy studies. Fixing the particle in a well-defined region, where the localization of the electromagnetic field is maximized, helps to effectively measure the particle with the highest accuracy. By keeping the particle close to the walls of the nanopore, it creates nanocavities, where the electromagnetic field is strongly amplified due to plasmonic interactions.

Since the particles are magnetically susceptible, it is possible to selectively affect particles with different magnetic properties. This opens up possibilities for selecting, filtering, and targeted particle management in multicomponent systems. For anisotropic particles (such as Janus particles), the magnetic field can be used not only for translational motion, but also for controlling the particle's orientation[89]. This is important for systems where the physical properties depend on the particle's orientation relative to the field or surface. By combining magnetic trapping with optical heating, it is possible to vary the temperature locally, affecting not only the magnetic properties but also the dynamics of particles through changes in the viscosity of the medium, diffusion, magnetic properties of materials, and controlling the temperature, which is crucial for biological molecules[87].

In the context of hybrid magneto-plasmon trapping, magnetoplasmic structures and Janus particles are of particular interest, in which particles with directional magnetic-optical properties can be created by combining materials[89]. Such systems provide multiphysical control, where the magnetic force is responsible for positioning and capturing, and the optical force is responsible for signal excitation and detection, additionally creating hot spots in certain places of interest of the nanostructure. Combining these effects is an essential step in the creation of new nanoplatforms capable of adaptively exploring biomolecular detection[89].

The effectiveness of magnetic trapping depends on a number of factors. The first thing that critically affects the magnetization is thermal fluctuations. It is known that the magnetic field can affect the efficiency of particle trapping[90]. This is especially important to consider for very small particle sizes, where thermal effects critically affect the stability of capture. It is equally important to note that in hybrid magneto-plasmon systems, the temperature critically affects the magnetization, since the higher the temperature, the weaker the magnetization[91]. However, by varying the heating conditions, it is possible to control the temperature increase, preventing degradation of the system properties during measurements.

When the physics of the magnetic capture process is considered, particles with an induced magnetic moment are usually considered, which is determined by their magnetic susceptibility and the value of magnetic induction[92]. The magnetic moment is defined as

$$m = V\chi \boldsymbol{H} \qquad (6)$$

where V is the volume of the particle, χ is the magnetic susceptibility, and $\boldsymbol{H}$ is the magnetic field. This expression describes the particle's susceptibility to a magnetic field through the polarization of its internal structure. The external magnetic field causes a redistribution of magnetic moments within the particle, resulting in an effective dipole.

To encourage the particle to move, the magnetic field must be inhomogeneous. In this case, we talk about the magnetophoretic force, which is directed towards increasing the magnetic energy.

In the simplest approximation, this force is proportional to the gradient of the square of the magnetic induction[93]:

$$F_m \approx \frac{V\chi}{2\mu_0}\nabla B^2 \qquad (7)$$

In simple words, this expression means that the particle tends to go to the region of a strong magnetic field[93]. This occurs because the energy of the interaction of the magnetic dipole with the field is proportional to B^2, and the force is determined by the spatial variation of this energy. Thus, as mentioned above, it is the field gradient that determines the possibility of particle movement and trapping.

The formation of significant gradients in hybrid nanopores is possible due to a certain geometry and the use of materials with magnetic properties. Near the edges and corners, there are regions where the field changes rapidly in space, resulting in high values of ∇B^2. This makes nanopores an effective tool for magnetic traps that can capture particles with sizes ranging from a few to tens of nanometers.

In the context of nanopores, it is usually assumed that the particle is moving in a liquid. Therefore, in addition to the magnetic force, the particle is also affected by thermal fluctuations due to Brownian motion and, of course, the flow rate. Brownian motion is associated with the thermal energy k_BT and can lead to random movement of the particle. The viscosity of the medium in which the particle is located can limit the speed of movement, and the dynamics are described by a balance between force and resistance.

Thus, the magnetic energy of a particle in a field is described as

$$U_m \approx \frac{V\chi}{2\mu_0}B^2 \qquad (8)$$

Thus, the efficiency of trapping is determined by the magnitude of the magnetic field, the geometry of the particle, and its magnetic susceptibility.

In practice, it is often more difficult to trap small particles than large particles. Since the magnetic energy is proportional to the volume of the particle, reducing its size also reduces the force and depth of the potential well. However, in the case of thermal effects, the thermal energy remains constant, which can lead to the dominance of Brownian motion. This means that significant magnetic field gradients are required to compensate for thermal fluctuations.

An important limitation is the distance from the potential trap to the magnetic field source. The gradients of the magnetic field rapidly decrease as it moves away from the magnetic element. This means that the effective range of the magnetic trap is limited and localized near the field source. In nanopores, the geometry must be designed in such a way that capture is only possible near the edges.

There are other factors that can limit the particle's movement in the pore, such as geometric constraints. While these constraints help to keep the particle near the high-gradient region of the field, they also increase the hydrodynamic resistance and can alter the particle's trajectory. Therefore, the trapping behavior is influenced not only by the magnitude of the magnetic force but also by the complex interactions with the channel geometry.

Thus, magnetic trapping in nanopores is possible and is the result of an interaction between the directional action of magnetic forces and thermal motion. The effectiveness of this interaction is determined by a combination of parameters, including the magnetic properties of the particle, the magnitude and gradient of the field, temperature, and geometry. This makes magnetic trapping a controllable method, but it also requires a specific approach for effective operation at the nanoscale.

1.5 Temperature-dependent magnetism in hybrid nanopores

Ferromagnetic materials such as iron, cobalt, nickel, etc., are characterized by a strong dependence of their magnetization on temperature and affect single molecule detection in hybrid plasmon-magnetic nanopores[94–96]. As mentioned earlier, local optical heating caused by plasmon absorption in metal layers at a resonant wavelength leads to a change in the magnetic state of the ferromagnetic component. This directly affects the distribution of the magnetic field and its gradients, which determine the forces acting on the particles near the nanopore.

The magnetization of ferromagnetic materials is characterized by the collective orientation of the magnetic moments of electrons[97]. In this case, each atom contributes to the total magnetic moment, and the emergence of macroscopic magnetization is facilitated by moments oriented mostly in the same direction[98]. The low temperature contributes to the orientation of the spins, where they are maximally consistent, and the magnetization, in turn, reaches a value close to saturation[98]. However, an increase in temperature leads to thermal fluctuations, which lead to a deviation of the magnetic moments from their usual equilibrium direction at low temperatures. Such deviations are collective in nature and lead to a change in the orientation of the spins[98].

Sometimes, very small deviations of individual magnetic moments reduce their projection onto the direction of collective magnetization[96]. The macroscopic magnetization, being the sum of these projections, decreases under the influence of the effect of a large number of small deviations[97]. Thus, the magnitude of the magnetic moment of individual atoms remains almost unchanged, and the degree of their coordinated orientation decreases.

The deviations increase with increasing temperature, which gradually leads to a monotonous decrease in magnetization[99]. It is worth noting that at a given temperature range (significantly lower than the Curie temperature), the ferromagnetic order is preserved, but the magnetic moments are less aligned, which is observed in a decrease in the macroscopic magnetic response[99]. As a result, the magnetization becomes temperature-dependent $M(T)$, decreasing monotonously as it increases. In the range of temperatures significantly lower than the Curie temperature, this behavior can be described within the framework of Bloch's law[100]:

$$M(T) = M_0\left(1 - \beta T^{\frac{3}{2}}\right) \qquad (9)$$

where β is determined by the properties of the material. Thus, the main mechanism says the number of thermally excited spin waves increases with increasing temperature[100].

Thus, temperature fluctuations affect the magnetization by smoothly disrupting the consistent orientation of the spins[101]. This is especially critical for nanostructures, as such changes affect local magnetic fields and related forces.

In thin ferromagnetic films, surface and interface effects enhance the magnetization's sensitivity to temperature changes. Because a large proportion of atoms are located near the edges, thermal vibrations can more easily disrupt spin alignment compared to bulk materials. Nevertheless, even in ultra-thin films, moderate heating to temperatures below the Curie point does not cause a fast and dramatic loss of magnetization. The system maintains its ferromagnetic state, and the resulting changes in local magnetic fields and magnetic force distributions remain relatively constrained.

In hybrid magneto-plasmonic nanopores, optical heating mainly occurs due to plasmonic absorption in the noble metal layers. In this case, the ferromagnetic layer is indirectly heated by heat transfer through the multilayer structure. Even if this process increases the local temperature near the nanopores, the final temperatures are typically much lower than the Curie temperature of cobalt (or other similar ferromagnetic materials). This means that the magnetic field gradients that facilitate particle capture and manipulation are largely preserved. In this case, moderate plasmonic-induced heating may slightly alter the magnetic response, but it does not critically suppress the system's ability to magnetic trapping.

1.6 Motivation for hybrid magneto-plasmonic nanopores

Particle control in a nanopore is very well exploring nowadays and is only becoming more interesting. Nowadays, external fields are actively used to control the transport of particles and molecules not only in the pore, but in general they have found wide application. In the context of nanopores, the most common and effective approaches are based on using plasmonic and magnetic forces[58]. Each of these approaches is characterized by fundamentally different physical mechanisms. While plasmonic structures localize and amplify the electromagnetic field in areas sometimes even shorter than the wavelength, magnetic systems, under the influence of an external field, form magnetic field gradients that allow the particle to be trapped[102]. Each of these methods has its own advantages and disadvantages, which must be taken into account. Thus, for more effective trapping, the obvious step is to combine them into hybrid platforms that includes these two methods simultaneously using their advantages to the maximum and trying to offset the disadvantages.

Due to their plasmonic properties, metal nanostructures provide extreme amplification of the electromagnetic field near the metal surface. In this way, localized regions with high field intensity

are formed in nanopores, in which significant electric field gradients occur[103]. These gradients affect the polarizability of particles and molecules[103]. As mentioned earlier, field amplification is indispensable in experimental optical measurements such as fluorescence and Raman scattering, which has already shown plasmonic nanopores to be a powerful detection tool[104].

At the same time, plasmon amplification is always characterized by the inevitable absorption of energy in the metal and losses leading to local heating[105]. Heating is heterogeneous and mainly concentrated near the areas of the maximum field. As a result, temperature gradients affect all properties of the medium, including viscosity, diffusion, and electrical conductivity[106]. It should also not be excluded from consideration that temperature effects can lead to additional forces, such as thermophoresis, which complicates particle dynamics and makes the system less predictable[107,108].

Magnetic methods, in turn, are characterized by a controlled control mechanism that does not require high powers and does not depend much on the properties of the structure. If the system under study contains a solution of electrolytes, then the magnetic field is not shielded by the electrolyte and practically does not depend on its properties, which is a great advantage in nanofluidics. Magnetic forces arise in inhomogeneous fields and are directed along the magnetic energy gradient, which makes it possible to form stable traps by setting the necessary properties to direct the field in the needed direction[109]. Magnetic trapping itself is not accompanied by significant heating, which, combined with optical methods, does not complicate the system.

Like optical traps, magnetic traps also have their limitations. The effectiveness of magnetic trapping is determined by the magnitude of the field gradient and the magnetic properties of the particle[110]. As mentioned earlier, small particles may not have sufficient ability to overcome thermal fluctuations or be controlled by magnetic force, which limits the scope of such methods[111]. Moreover, magnetic traps are usually less localized than plasmonic hot spots, which reduces the spatial resolution of the control.

Thus, combining plasmonic and magnetic methods, it is possible to create hybrid platforms with a number of advantages and minimizing disadvantages. Due to plasmonics, it is possible to achieve strong localization of the field, as well as high sensitivity, but inevitably lead to heating. Magnetic

trapping is controllable, but limited in magnitude of forces and spatial resolution. By combining these methods into one system, it becomes possible to take advantage of each approach.

Even this combination has its drawbacks. Plasmonic excitation, leading to local heating, affects the magnetic properties of ferromagnetic materials, which, as previously described, are sensitive to temperature. The magnetization of the ferromagnetic layer decreases with increasing temperature, leading to a decrease in the intensity of magnetic field gradients and a decrease in the probability of particle trapping[112]. Thus, there is a possibility that plasmon heating can weaken magnetic trapping.

To summarize, the main stumbling block in the described system is the complex interaction between several physical processes. The amplification of the electromagnetic field increases the optical strength and sensitivity of the system. And the resulting heating changes the magnetic properties of the material and, consequently, the magnetic forces and, additionally, causes some thermophoretic effects. As a result, the behavior of the system is determined by the balance between field amplification, thermal effects, and magnetic response.

Thus, the main scientific question is the behavior of the system in the simultaneous presence of a strong localized field, significant heating and a magnetic layer? First of all, it is necessary to understand how temperature changes affect the magnetic field and its gradients, and how this affects the forces acting on the particles. All this implies considering the system as a single multiphysical object in which optical, thermal and magnetic processes are closely related.

It is necessary to consider the totality of all forces acting on the system. Firstly, the main contribution is made by optical forces proportional to the gradient E^2, and magnetic forces are determined by the gradient B^2. In addition to these forces, drag force acts on the system, which is always taken into account when considering fluid flow and trapping. If necessary, such forces as thermophoresis and hydrodynamic effects can be considered. Thus, the trapping force looks like

$$F_{trap} = F_{opt} + F_{magn} + F_{drag} + F_{thermoph} \qquad (10)$$

It is especially important to take into account the geometry of the structure, in which forces will not compete, trying to trap the particle in different spots. Proper geometry selection ensures trapping of the particle in places where the optical enhancement coincides with the maximum

magnetic field gradient, ensuring the maximum possible capture efficiency[85]. It is also important to select the particle that is affected by the forces. It is necessary to consider the plasmonic component at the same time, which means that the particle must contain a metal part, but also not to forget about the magnetic one. Core-shell or Janus particles are excellent for such purposes.

It is worth noting that considering such a system together provides many advantages, since most of the works devoted to plasmonic and magnetic nanopores or magneto-plasmonic nanopores usually consider the mentioned physical mechanisms of particle trapping separately. For plasmonic systems, the main focus is on calculating the distribution of the electromagnetic field and its amplification, while for magnetic systems, attention is focused on calculating the distribution of magnetic induction, its square and gradient. At the same time, the structure is considered as a purely static system in which the multiphysical interaction is greatly simplified or completely ignored.

In real experiments, the laser power significantly affects the local temperature in the plasmonic hot-spots, resulting in pronounced temperature gradients in the surrounding fluid[113,114]. Although the increase in temperature does not significantly affect the magnetic field distribution itself, it significantly influences the particle dynamics through thermophoretic drift and local fluid flows.

By increasing the laser power, plasmonic heating can induce thermophoretic motion, which literally pushes the particles out of the trapping region[115]. In this case, the trapping efficiency is determined not only by optical and magnetic forces, but also by the competition between conservative trapping mechanisms and thermally induced transport. Therefore, models that do not account for thermal effects may overestimate the stability of trapping and the efficiency of particle capture compared to the actual behavior of the system.

Thus, the existing approach based on a separate consideration of optical, thermal, and magnetic effects is insufficient to describe hybrid plasmon-magnetic nanopore systems. Ignoring thermophoretic transport and temperature-induced flows limits the interpretation of experimental results and complicates the optimization of nanopore structure.

In this regard, there is a need for a more comprehensive multiphysics description that takes into account the relationship between optical heating, thermophoretic transport, and trapping dynamics.

Incorporating thermal effects into the model allows for a more accurate assessment of the impact of laser heating on particle trajectories, trapping stability, and capture efficiency. This approach is essential for understanding the behavior of hybrid nanopore systems and for developing nanopores with tailored functional properties.

1.7 Objectives of the Thesis

Main research objective

The main objective of this work is to develop and implement a comprehensive multiphysics modeling framework for hybrid plasmonic–magnetic nanopores using COMSOL Multiphysics, enabling the analysis of coupled electromagnetic, thermal, magnetic, and particle transport phenomena, and to quantify how their interplay governs nanoscale trapping and transport processes.

Research tasks

1. Electromagnetic field enhancement and optically induced heating in plasmonic nanopores (Au/Co/Au–SiN)

- To compute the spatial distribution of the electromagnetic field in multilayer plasmonic nanopores and evaluate the resulting field enhancement under optical excitation.
- To quantify optical absorption in metallic layers and determine the resulting temperature distribution, including spatial gradients and maximum temperature increase, as a function of geometry and illumination conditions.

2. Magnetic response of the hybrid structure

- To incorporate magnetization M(T) of the ferromagnetic layer and analyze its impact on the magnetic field distribution.
- To evaluate how thermally induced changes in magnetization modify the magnetic flux density.

3. Particle trapping and trajectory analysis under combined forces

- To model particle dynamics in the nanopore environment under the combined influence of magnetic, optical, and thermal effects.

- To compute trapping potentials, evaluate the balance between magnetic forces and thermal fluctuations, and simulate particle trajectories to determine capture conditions, stability of trapping, and transport behavior.

4. Ionic current rectification (ICR) and electromagnetic field enhancement in 3D nanopores

- To investigate electromagnetic field enhancement in three-dimensional nanopores without magnetic components.

- To analyze ionic current rectification (ICR) and its modulation by local electric fields and temperature distribution, treating this subsystem independently from the hybrid plasmonic–magnetic framework.

2. Methods and modeling workflow

In this work, all calculations were performed using the COMSOL Multiphysics software[116], which is based on the finite element method for solving multiphysics-related problems. This software allows for simultaneous calculation of electromagnetic, thermal, magnetic, and transport processes, making it an indispensable tool for modeling the physical processes of hybrid plasmon-magnetic nanopores. This chapter provides a description of the calculations, boundary conditions, mesh generation, and more.

2.1 Electromagnetic field simulations

Geometry

Chapter 3 is devoted to the study of the optical properties of a hybrid Au/Co/Au/SiNx (5/5/100/100 nm thickness) nanopore array with a hole diameter of 250 nm and a periodicity of 550 nm. The 3D geometry is presented in the form of a simulated box (10 um) containing the multilayer system under study (Figure 13).

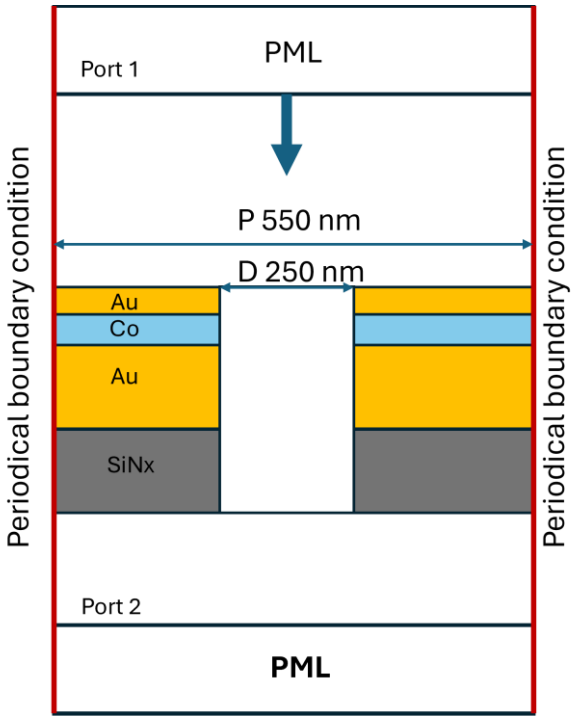

Figure 13 Schematic representation of Au/Co/Au/SiN_x nanopore system

The hole passes through the entire structure, forming a through-channel. The simulation was performed for a single elementary cell with periodic boundary conditions in the plane of the structure.

All the simulations were calculated in water. Standard parameters were used: thermal conductivity, density, heat capacity, and viscosity corresponded to reference values (which are contained in the Comsol library[116]). The heat transfer coefficient with the liquid for further temperature calculations varied from 0 to 500 W/(m^2K).

The electromagnetic field was calculated in the *Electromagnetic Waves, Frequency Domain* physics module. To calculate the transmission spectrum, the spectral range was set from 400 to 1000 nm, while all other calculations of the EM field amplification were performed at a wavelength of 780 nm as a plane wave propagating along the x-axis. This wavelength was chosen based on the maximum plasmonic resonances in the structure, as determined by the transmission spectrum calculation.

The Electromagnetic Waves, Frequency Domain section solves Maxwell's equations:

$$\nabla \times (\mu_r^{-1} \nabla \times \mathbf{E}) - k_0^2 \varepsilon_r \mathbf{E} = 0 \qquad (11)$$

where $\mathbf{E}$ is electric field vector, $\nabla \times$ is curl operator, μ_r is relative magnetic permeability, ε_r is relative permittivity, k_0 is wave vector ($k_0 = 2\pi f/c$). Optical properties are determined by the dielectric constant ε_r for metals (Au, Co) and take into account absorption at different wavelengths. At the upper and lower boundaries, scattering conditions or PML (perfectly matched layers) were applied (Figure 13) to prevent unwanted reflections.

To calculate the locally enhanced field E^2 in a nanopore, the parameter was considered as:

$$E^2 = \frac{E^2_{calculated}}{E^2_{background}} \qquad (12)$$

This parameter characterizes the degree of field amplification compared to the field specified as background.

2.2 Heat generation

Optical absorption and heat generation

The absorption of electromagnetic energy in metals inevitably leads to the generation of heat, which is described by the expression:

$$Q = \frac{1}{2} \omega \varepsilon_0 \mathrm{Im}(\varepsilon_r) \mid E \mid^2 \qquad (13)$$

where Q is power dissipation density, ω is angular frequency, ε_0 is devoted to permittivity in vacuum, $\mathrm{Im}(\varepsilon_r)$ is imaginary part of the relative permittivity (responsible for for losses), $\mid \mathbf{E} \mid$ is magnitude of the electric field

The main contribution to heating comes from gold, as it is responsible for plasmon excitation. The generated heat spreads throughout the structure, including the cobalt layer.

Heat transfer modeling

To correctly calculate the temperature distribution, the heat conduction equation was solved in the *Heat Transfer in Solids and Fluids* physics section:

$$\nabla \cdot (k\nabla T) + Q = 0 \qquad (14)$$

where $\nabla \cdot$ is divergence operator, k is thermal conductivity, ∇T is temperature gradient, T is temperature, Q is volumetric heat source (power density).

The incident radiation power varied from 0.5 to 5 mW, concentrated in a 20-μm-diameter beam, which set the boundary conditions for the intensity.

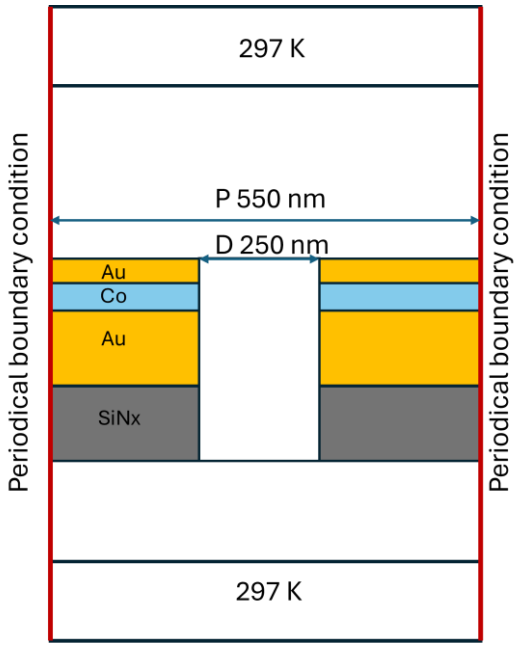

Figure 14 Heat boundary conditions

The temperature value corresponding to the ambient temperature was set at the upper and lower boundaries of the simulated box to ensure proper heat exchange.

The *Heat Transfer in Solids and Fluids* section was multiphysically coupled to the *Electromagnetic Waves, Frequency Domain* section, as the energy loss data in gold was used to calculate the temperature. This resulted in a spatially heterogeneous temperature distribution, T.

2.3 Magnetic field distribution

Magnetic field modeling

The magnetic field was calculated in the *Magnetic Fields (No Currents)* interface. In the model, cobalt was used as a material with magnetic properties. The magnetization was set to approximately 0.1 T, and the distribution of B, B^2 and ∇B^2 were calculated.

It has been shown that a change in temperature does not lead to a significant change in the magnetization of the system, which is important for studying the properties of hybrid nanopores.

2.4 Magneto-plasmonic core-shell nanoparticles

Magneto-plasmonic trapping was performed using core-shell magnetic-plasmonic nanoparticles, which consist of a magnetic core Fe_3O_4 and a gold shell Au. These particles were chosen due to their widespread application in nanosensing[117]. Three characteristic particle sizes were considered: 14 nm, 50 nm, and 100 nm, with shell thicknesses of 2 nm, 10 nm, and 20 nm, respectively[117]. This geometry reflects small, medium, and large particles that can potentially be used for nanotrapping, as they combine the magnetic properties of the core with the plasmonic properties of the metal shell.

Geometrical characteristics

The total radius of the particle R and the core radius were defined as:

$$R_{core} = R - t_{shell} \tag{15}$$

where t_{shell} is shell thickness.

Particle volume:

$$V = \frac{4}{3}\pi R^3 \tag{16}$$

Core volume:

$$V_{core} = \frac{4}{3}\pi R_{core}^3 \quad (17)$$

Shell volume:

$$V_{shell} = V - V_{core} \quad (18)$$

Effective particle density

The effective particle density was determined as:

$$\rho_{eff} = \frac{\rho_{core}V_{core} + \rho_{shell}V_{shell}}{V} \quad (19)$$

where $\rho_{core} \approx 5200$ kg/m^3 is density of Fe_3O_4, $\rho_{shell} \approx 19300$ kg/m^3 is density of Au.

Thus, calculated densities values for three nanoparticles are:

14 nm: $\rho \approx 9500$ kg/m^3

50 nm: $\rho \approx 14800$ kg/m^3

100 nm: $\rho \approx 14800$ kg/m^3

Magnetic properties of nanoparticles

The magnetic properties of particles are determined primarily by the particle core Fe_3O_4. The effective magnetic susceptibility was used for nanoparticles χ, corresponding to superparamagnetic behavior:

$$\chi \sim 0.1 - 1.$$

Then relative magnetic permeability:

$$\mu_r = 1 + \chi \tag{20}$$

In the calculations it was assumed $\mu_r \approx 1.5 - 2$, which corresponds to nanoscale magnetic particles.

The magnetic force acting on a particle is determined by the magnetophoretic mechanism:

$$\boldsymbol{F}_{mag} = \frac{V\chi}{2\mu_0}\nabla B^2 \tag{21}$$

Optical properties and polarizability

The optical response of particles is determined by the gold shell that supports localized plasmonic resonances. In the dipole approximation, the optical force is expressed through the polarizability of the particle:

$$\boldsymbol{F}_{opt} = \frac{1}{2}Re(\alpha)\nabla \mid E \mid^2 \tag{22}$$

Polarizability of a spherical particle:

$$\alpha = 4\pi\varepsilon_0 R^3 \frac{\varepsilon_p - \varepsilon_m}{\varepsilon_p + 2\varepsilon_m} \tag{23}$$

where ε_p is effective dielectric function of the particle, ε_m is dielectric constant of the environment.

For core–shell particles, the effective polarizability is determined by the contribution of the shell and the core, but for the calculation and due to the complex multiphysics settings in Comsol, the contribution of the gold shell dominates, so the polarizability of the particles was simplified to consider the polarizability of the gold particle.

2.5 Magneto-plasmonic particle trapping

Drag force and fluid interaction

This section describes a numerical model of the motion of magnetoplasmon particles in a liquid under the influence of magnetic, optical, and viscous forces.

The motion of particles in a fluid was considered as a multiphysics system in the Newtonian approximation mode. In this case, the inertial forces were not neglected, and the particle motion was defined as Eq.10:

$$\boldsymbol{F}_{total} = \boldsymbol{F}_{mag} + \boldsymbol{F}_{opt} + \boldsymbol{F}_{therm} + \boldsymbol{F}_{drag}$$

Brownian motion was not taken into account in this model, as the main goal was to analyze the deterministic trajectories of particles under the influence of external fields. Its influence is discussed at the level of estimation through thermal energy $k_B T$.

Forces implementation in Particle Tracing for Fluid Flow

Particle Tracing for Fluid Flow physics section was used to calculate the forces that affect the capture and trajectory of particles.

The magnetic force was set in the same interface using the built-in Magnetophoretic Force module, and was defined as a force proportional to the gradient of the square of the magnetic field. The magnetic field was pre-calculated in *Magnetic Fields (No Currents)* section and multiphysically coupled with this section.

Due to the technical features of the software, the optical force was connected separately through the External Force node after the preliminary calculation of the electromagnetic field. It was determined in the dipole approximation (Eq. 22) using the particle's polarizability and the gradient of the square of the electric field.

The components of the external force were specified as coordinates:

$$F_x = \frac{1}{2}\mathrm{Re}(\alpha)\frac{\partial \mid E \mid^2}{\partial x} \quad (24)$$

$$F_y = \frac{1}{2}\mathrm{Re}(\alpha)\frac{\partial \mid E \mid^2}{\partial y} \quad (25)$$

$$F_z = \frac{1}{2}\mathrm{Re}(\alpha)\frac{\partial \mid E \mid^2}{\partial z} \quad (26)$$

Thermophoretic effects

First of all, the temperature distribution in the system is determined by the heating of the gold layers (due to their plasmonic properties) with different power densities of laser radiation at a wavelength of 780 nm in the nanopore. Thus, an increase in power contributes to an increase in temperature and an increase in its gradients in the simulated box.

The thermophoretic force due to temperature gradients acting on a particle can be written as:

$$\mathbf{F}_{th} \propto -\nabla T \quad (27)$$

This force promotes the directional movement of particles from areas of higher temperature to areas of lower temperature.

Thus, the temperature gradient is directly related to plasmon excitation, as the absorption of electromagnetic radiation determines the local heating. By increasing the laser power, the temperature field changes, but the EM field has a more significant effect on trapping under the considered conditions.

Viscous drag and fluid interaction

The motion of particles in a liquid characterized by viscous resistance is described by Stokes' law:

$$\boldsymbol{F}_{drag} = 6\pi\eta R\boldsymbol{v} \quad (28)$$

where η is dynamic viscosity of the liquid, R is particle radius, $\boldsymbol{v}$ is a velocity of liquid.

In the conditions under consideration, the liquid is initially stationary and its velocity is equal to 0. In this regime, inertial effects are negligible, and the particle's motion is determined by the balance of the forces acting on it.

Viscous drag has a significant impact when considering the motion of objects in a liquid. Viscosity can limit their speed, altering their motion. Unlike magnetic and optical forces that determine the direction of motion, drag force does not affect the equilibrium position, but it can determine the speed at which the trapping region is reached.

Important approximations

In the Comsol software, in the Particle Tracing in section, the particle is not present in geometry as a physical object, but is modeled within the point-particle approximation, where dimensions are not explicitly taken into account, and the influence of fields is calculated at fixed points in space.

This approach is justified by the fact that the characteristic sizes of the particles under consideration (10-100 nm) are significantly smaller than the spatial scales of changes in the magnetic and optical fields. In this case, the particle can be considered as a point dipole, and the forces acting on it are determined by the values of the fields and their gradients at the particle's position.

In addition, this approach makes it possible to significantly simplify the computational task, since it does not require recalculation of fields when moving a particle and eliminates the need to take into account the inverse effect of the particle on the field distribution.

The approximation used introduces a number of limitations. The following are the effects that are not considered in the simulated system:

- the final particle size and interaction with the nanopore walls;

- hydrodynamic effects near walls;
- the effect of a particle on the distribution of electromagnetic and magnetic fields;
- nonlinear effects under high fields;
- Brownian motion of the particle.

In particular, the point-dipole approximation is expected to be least accurate for the largest particle (100 nm in diameter), since its size approaches the characteristic length scale over which the plasmonic near-field decays near the gold surface, based on the field distributions shown in Figure 18. For a particle of this size, a substantial fraction of its volume can experience a field magnitude appreciably different from the value evaluated at a single point (its center), and the particle's own presence may locally perturb the field distribution to a degree the model does not capture. For the smaller particles (14 nm and 50 nm), whose dimensions remain small relative to this decay length, the point-particle approximation is expected to hold more accurately.

Brownian motion was deliberately excluded from this model. Including it would require a stochastic (Langevin) approach to particle dynamics, with multiple independent realizations calculated for each combination of particle size and laser power to obtain statistically significant trapping probabilities. This approach would add computational overhead to the already complex four-way coupling between electromagnetic, thermal, magnetic, and particle tracing physics. The deterministic model used here was chosen as a necessary first step: it characterizes the location of traps, potential wells, and the competition between forces. Within this model, a computed trajectory remaining in a trap should be understood as demonstrating the absence of a net deterministic force ejecting the particle from the trap, rather than as a guarantee of stability with respect to real thermal fluctuations.

Interpretation of trapping time

Within the framework of this calculation, the characteristic time for which the particle reaches the trap is determined. However, it is important to note that calculated time is not equal to the trapping time!

There are a number of factors that are not taken into account in these calculations, affecting the real dynamics:

- Brownian motion;
- random fluctuations in the liquid;
- particle-surface interaction;
- adhesive effects.

As a result, the resulting time characterizes the deterministic motion of a particle under the action of forces and can be considered as a characteristic drift time, rather than as a trapping time.

Time stepping and numerical considerations

The particle trajectories were calculated during the time integration. The time step should be chosen in such a way that it determines the correctness and stability of the calculation.

For example, a too large time step can cause the trajectory to lose its shape, miss areas where the force gradients change rapidly, incorrectly determine the capture point, and finally cause the particle to pass through an opening.

In a situation where the step is very small, computational costs increase without a significant gain in accuracy.

In this work, the time step was selected from 10^{-5} to 10^{-9} seconds, to correctly resolve the regions with maximum field gradients near the nanopore walls. To verify the correctness of the calculation, a convergence analysis was performed on the time grid, where reducing the step size did not significantly change the trajectories.

Workflow description

The full computational process is implemented as a sequential multiphysics chain:

1. Calculation of the electromagnetic field

2. Calculation of absorption and heat generation
3. Calculation of temperature distribution
4. Calculation of temperature-dependent magnetization
5. Magnetic field calculation
6. Determination of forces
7. Particle trajectory calculation

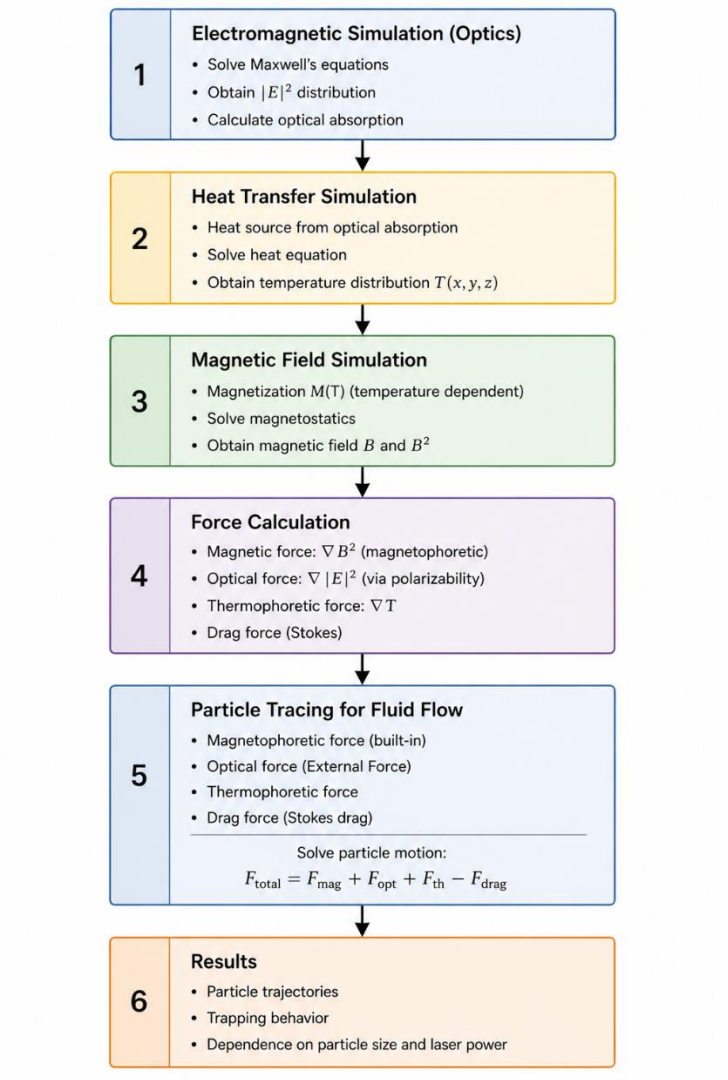

Figure 15 Modeling workflow

2.6 Ionic current rectification calculations

An analysis of ion transport in 3D nanopores composed of dielectric materials was performed to calculate rectification. The structures described are 3D nanopores fabricated from materials such as aluminum and silicon and were considered separately from the hybrid nanopore described above. The purpose of this calculation was to investigate the effect of ionic current rectification (ICR) and its relationship to the pore geometry, electric field distribution, and local environmental conditions.

The simulations were performed in COMSOL Multiphysics using the Electrostatics and Transport of Diluted Species interfaces, which allowed for the coupled solution of the Poisson–Nernst–Planck equations (Eq. 2, 3, 4, 5).

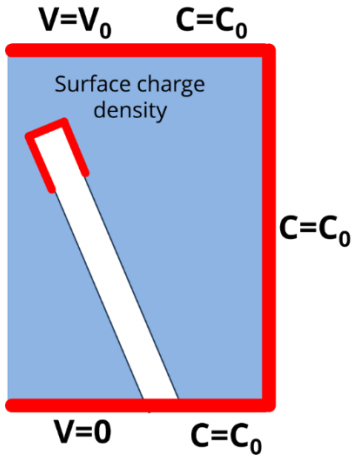

Figure 16 Boundary conditions for ICR estimation in 3D nanopores

The boundary axisymmetric conditions (as shown on Figure 16) for ICR modeling standardly include a fixed potential at the input and output of the nanopore (the upper and lower boundaries of the box) to model the system's current-voltage characteristics. The calculated distributions of ion concentration and electrical potential allow for the calculation of the total ion current through the pore. The analysis was performed for opposite polarities of the applied voltage, which is a standard approach for evaluating rectification characterized by the asymmetry of currents under different polarities:

$$r = \frac{I(-V)}{I(+V)} \tag{29}$$

It should be emphasized that this section was considered independently of the hybrid plasmon-magnetic system. That is, magnetic and optical effects were not included in the ion transport model, but these results are important for the behavior of nanopores in general, as they demonstrate how the electromagnetic field and geometry can affect transport processes at the nanoscale.

Numerical implementation, mesh strategy and convergence

To ensure detailed accuracy of calculations, an adaptive finite element grid with local thickening in areas where strong gradients of physical quantities are expected was used in all physical modules. In particular, the maximum grid thickening was implemented:

- near the edges of the nanopore,
- at metal–dielectric interfaces,
- in the ferromagnetic layer (Co), where magnetic field gradients are formed,
- in all the areas with tiny dimensions.

The minimum grid element size in extremely small regions was 0.1–2 nm for accurate calculations near narrow geometric regions. A coarser grid was used in the fluid volume and away from the structure to optimize computational resources.

The validation of the results was carried out as a mesh convergence study. The grid was consistently reduced until the change in key values was less than 2-3%. This ensured the numerical stability of the results and their independence from discretization.

3. Electromagnetic Field Enhancement in Plasmonic Nanopores

Optical absorption in hybrid magneto-plasmonic nanopores is determined by the distribution of the EM field and is a source of structure heating. This section discusses the effect of radiation on the spectral characteristics of a hybrid pore in the presence and absence of a particle, as well as the enhancement of the EM field and the spatial distribution of temperature.

3.1 Optical response and transmission spectra

Before proceeding to the direct particle trapping, it is necessary to determine the areas where hot spots are formed and how the particle interacts with the hybrid nanopore. Therefore, the first step is to analyze the plasmonic properties of the nanopore array, determine the resonant wavelength at which the field is amplified, evaluate the field enhancement in the presence of a particle at different distances from the nanopore walls and without the particle, and finally, calculate the temperature inside the pore for subsequent use in the context of magnetic fields.

The transmission spectrum of an array of hybrid nanopores (with a diameter of 250 nm and a pitch of 550 nm) was calculated in the wavelength range of 400-1000 nm, which covers the visible and near-infrared regions. This calculation was performed without the presence of a particle, in order to accurately assess the intrinsic resonance characteristics of the system.

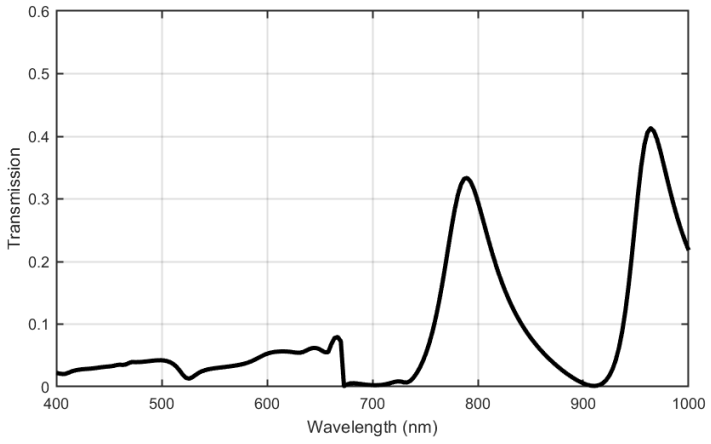

Figure 17 Transmission spectrum of bare hybrid nanopore (D=250 nm, P=550 nm)

As can be seen from Figure 17, the transmission spectrum shows pronounced resonances at wavelengths of 780 nm and 960 nm, indicating the excitation of plasmons in the gold layer. In this

case, the spectrum of a three-layer structure with a period of 550 nm and a hole diameter of 250 nm is formed due to the extraordinary transmission effect, which occurs when light passes through an array of holes. Since the non-perforated metal layer does not directly transmit light, the periodicity of the pores allows for the excitation of surface plasmon waves, which are re-emitted at the exit of the holes, creating transmission maxima.

For further calculations of temperature distribution and evaluation of EM field amplification, a wavelength corresponding to 780 nm was selected[85], as this wavelength is successfully used in experiments involving fluorescence and Raman spectroscopy (which are also actively used in experiments with solid-state nanopores).

3.2 Electromagnetic field distribution at resonance wavelength

At the resonant wavelength, the spatial amplification of the EM field $|E|^2$was estimated without the presence of a particle, as the assessment of how much the field is amplified at a given location can indicate the potential capture of a particle at that point.

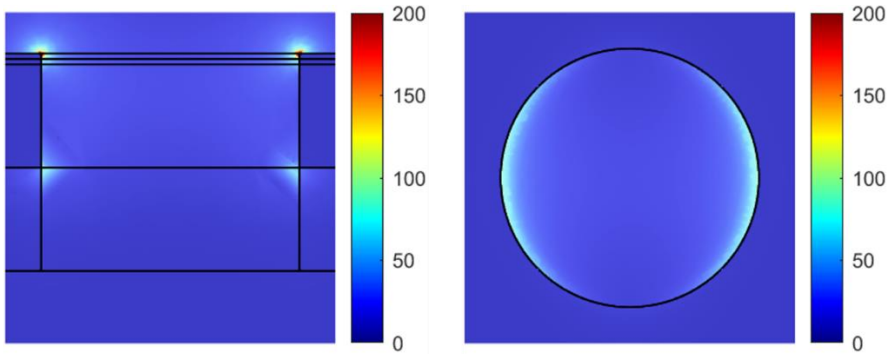

Figure 18 EM field enhancement $\frac{E^2}{E_0^2}$ in bare hybrid nanopore distribution in XY and XZ planes (D=250 nm, P=550 nm)

This distribution of the EM field intensity near the nanopore is determined by the boundary conditions at the Au/Co and Au/SiN interfaces. Near the edges of the nanopore, the maximum values of $|E|^2$ are localized at the edge of the hole and along its walls, forming a region with a highly localized EM field.

The excitation occurs with the electric field oriented along the x-axis, which is why the field charges are distributed asymmetrically, resulting in an asymmetry in the spatial distribution of $|E|^2$ and an enhancement of the field in specific regions.

3.3 Effect of particle on optical response

The introduction of a magnetic core–shell (Fe_2O_3-Au) particle near the nanopore inevitably leads to a change in the distribution of the EM field and, as a result, to visible changes in the spectrum. In the original system, the distribution of the field was primarily determined by the geometry of the pore and the optical properties of the materials, but the presence of the particle creates a local perturbation in the dielectric medium. It is assumed that the particle has already been attracted to the walls of the nanopore by the optical force, which simplifies the task and calculation of the optical response, as if the particle had already been trapped.

Implementation of the particle causes it to interact with the walls of the nanopore, especially in areas where there are metal layers. This interaction is reflected in the transmission spectrum as a shift in the resonant wavelength and a change in the intensity of the resonance compared to the nanopore alone. The magnitude of the shift (how much the maximum is displaced) is determined by the distance of interaction between the particle and the surface. Typically, the closer the particle is to the walls of the pore, the greater its impact on the local field and, consequently, on the spectral response.

To evaluate the contribution of a particle in the system under consideration, particles with diameters of 14, 50, and 100 nm were selected. This allows us to study the optical response of the system, as the size of the particle directly determines its polarizability and, consequently, its interaction with the electromagnetic field. As the particle size decreases, the perturbation caused by its small volume becomes less significant. Consequently, the spectral characteristics remain relatively unchanged (Figure 19).

As the particle diameter increases, it can significantly redistribute the field near the surface, causing more pronounced shifts in the resonance peaks or changes in their shape. For particles with a diameter of 100 nm, the interaction becomes even stronger, as the local conditions for

excitation of plasmon modes also change due to the particle size. In this case, the spectrum can significantly change.

It is also worth paying attention to the magnetic properties. An increase in the core diameter can lead to an increase in magnetization and, consequently, an increase in interaction with the magnetic field. Thus, particles of different sizes have different magnetic moments and react differently to magnetic gradients.

Figure 19 shows the transmission spectra of a hybrid nanopore, which demonstrate a complex dependence on two main parameters: the size of the particle (14, 50, and 100 nm) and the distance between the particle and the surface (0.5, 5, and 10 nm). Firstly, it is worth noting that two characteristic regions can be identified for all cases: a region with a weak response in the short-wavelength part (400–700 nm) and resonant peaks in the long-wavelength range (750–1000 nm). The resonances correspond to the excitation of plasmonic modes, which arise due to the specific geometry of the nanopore with a gold plasmonic layer particle. Without the particle, the position and shape of the resonances are solely determined by the structural parameters.

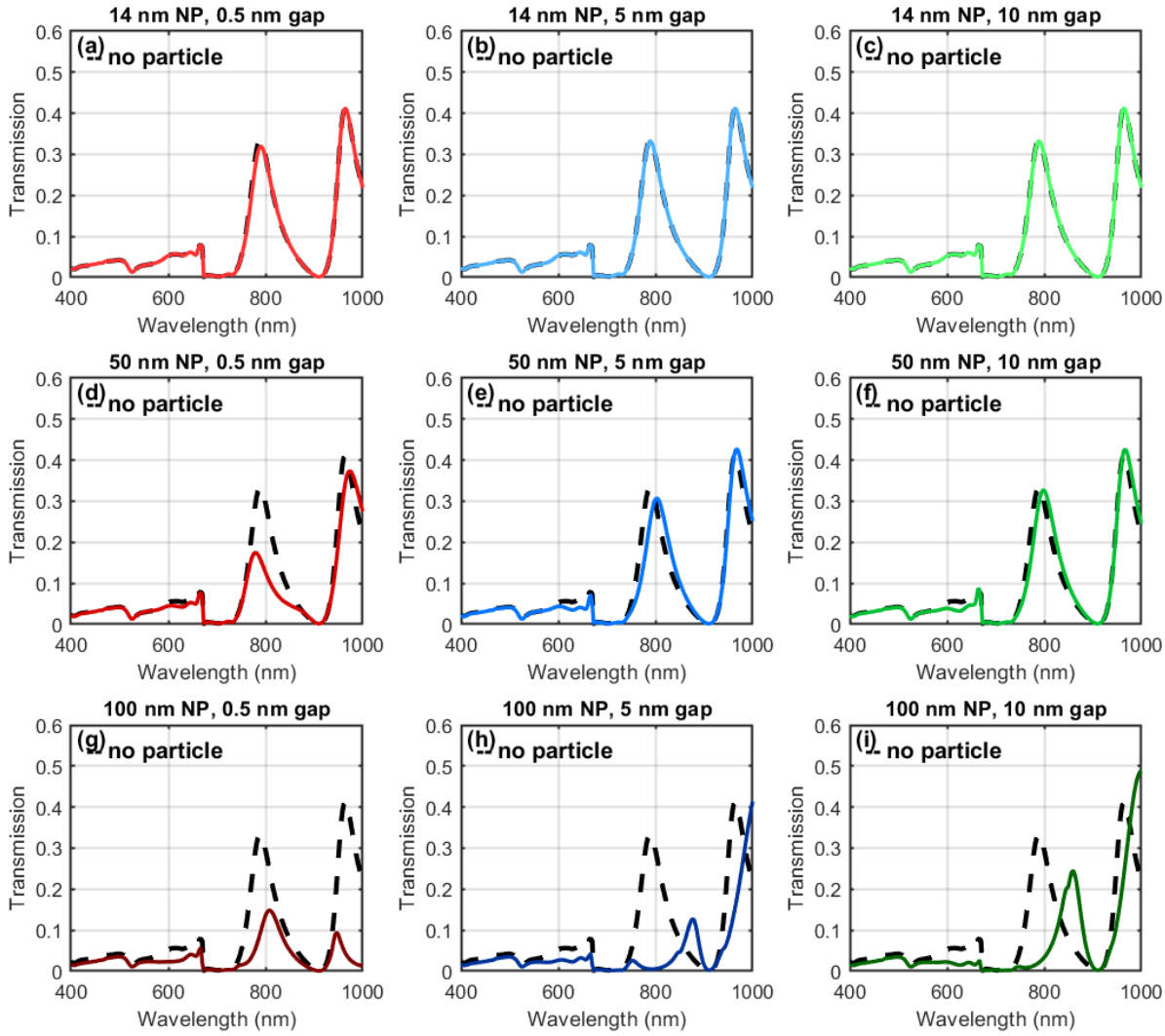

Figure 19 Transmission spectra of a hybrid nanopore in the presence of nanoparticles at different distances from the nanopore wall

By changing the gap, we can see that increasing the distance between the particle and the surface leads to a change in the transmission spectrum and a change in the shape of its maxima. At small distances (0.5 nm), the position of the maxima does not change significantly, but their intensity does. When a particle is introduced into the system, it interacts with the optical response of the pore, resulting in a response from the particle's dipole. For a particle with a diameter of 14 nm at a distance of 0.5 nm, the transmission spectrum remains relatively unchanged. However, for a particle with a diameter of 50 nm, there is a partial redistribution of energy, resulting in a decrease in the intensity of the peaks. For a particle with a diameter of 100 nm, the interaction becomes

even stronger, leading to the formation of new collective states. In this case, the energy is redistributed unevenly, suppressing the 780 nm resonance and enhancing the next longer-wavelength resonance.

As a plasmonic material, gold is prone to radiation losses under the influence of radiation, especially with an increase in diameter. The larger the particle, the more effectively the incident radiation is scattered, removing some of the energy from the localized modes of the nanopore. This further contributes to the reduction of the amplitude of individual resonance peaks and changes in their shape. In other words, the observed change in the amplitude of the peaks is also influenced by the internal redistribution of energy within the system and its partial scattering.

It is very important to note the role of the particle's surface size relative to the pore region where the interaction occurs. For example, a particle with a diameter of 100 nm almost completely covers the pore. In the case of a very small gap, the field is further amplified in this region. For a large particle, this effect becomes particularly strong, affecting the behavior of the entire system. As a result, it partially suppresses the initial resonance of the nanopore and changes the intensity distribution of the peaks in the spectrum.

As the distance between the particle and the surface increases to 5 nm, the interaction becomes significantly weaker, which is directly reflected in the transmission spectra (except for the 100 nm particle). This is because the localized EM field rapidly weakens as the distance between the particle and the surface increases, meaning that the particle is no longer in the highly localized field region. As a result, the particle's influence on the system decreases, and the spectrum gradually approaches the original case without the particle (as seen in the alignment with the dotted curve).

As mentioned earlier, for particles with a size of 50 nm, this manifests itself in a less pronounced deformation of the resonance peaks, where the particle and the pore behave more independently of each other.

Although for a particle with a diameter of 100 nm, the effect of the particle on the transmission spectrum is still present, it becomes less dominant. As the particle moves away, the resonances partially recover, and their amplitude becomes closer to the spectral characteristics without the

particle. Thus, increasing the gap leads to a transition from a strong interaction regime to a weak perturbation regime, where the particle's influence is limited.

Thus, in the cases under consideration, the maximum differences are achieved in the "large particle + small gap" mode. This confirms that the key factor is not only the presence of a particle, but also the degree of its optical coupling with the surface.

To summarize this section, the calculated spectra show that the system is sensitive to local changes in the dielectric environment. The particle changes the charge distribution on the metal surface, thereby altering the excitation conditions for plasmon modes. At small distances between the particle and the surface, the field is confined in a narrow gap, resulting in increased interaction and a shift in the resonance. As the distance increases, this interaction weakens, and the system gradually returns to its original state. Similarly, increasing the size of the particle enhances its contribution to the redistribution of the field by increasing its polarizability. While the influence of small particles is noticeable when the gap between the particle and the pore wall is small, for large particles, even as the gap increases, the resonance peaks remain shifted and modified in shape. Thus, unlike small particles, whose influence quickly dissipates as the distance increases, a large particle alters the optical response of the system over a wider range of distances.

3.4 Field enhancement in the presence of a particle

As mentioned earlier, the changes shown in the transmission spectra when a particle enters a nanopore are directly related to the redistribution of the electromagnetic field near the nanopore due to the interaction of the particle with the pore walls. The distribution of |E|^2 allows us to understand where these changes are localized and what physical mechanisms are behind them.

Figures 20-23 show that the introduction of a particle leads to a redistribution of the EM field near the pore surface. For a small particle (14 nm), even due to its small diameter, we can see a strong localization of the field on the side facing the particle. As previously shown in the transmission spectra, the field is most concentrated between the particle and the surface when the gap is small (0.5 nm). Although the interaction and amplification between the pore and the particle is very strong, and the localization of the field is also strong, it does not lead to a significant change in the spectrum. As the gap increases to 5 and 10 nm, the localization weakens, and the field becomes

more symmetrical, gradually returning to the distribution characteristic of a pore without a particle. This is consistent with the fact that the particle's influence on the spectrum decreases in this case.

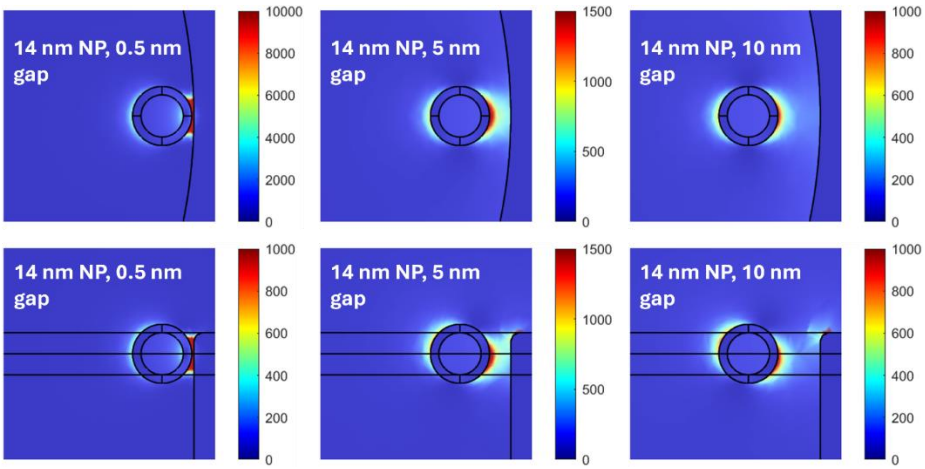

Figure 20 EM field distribution $\frac{E^2}{E_0^2}$ of the pore with 14 nm NP under 780 nm laser excitation

For medium-sized particles (50 nm) (Figure 21), the behavior becomes more pronounced. Compared to the 14 nm particle, the medium-sized particle interacts more deeply with the field localization region. In the case of a small gap, it can be seen that the EM field begins to redistribute along the entire boundary of the particle-surface interaction. This indicates that the particle is in a state of high interaction with the pore, resulting in a weakened EM field within the pore and an enhanced field near the particle. As the distance increases (5 and 10 nm), the maximum enhancement decreases, but it still remains visibly enhanced around the particle. Despite the weakening of the interaction, the EM field remains enhanced.

For a particle with a diameter of 100 nm (Figure 22), in the case of a small gap, the maximum amplification factor reaches the same order of magnitude, but the amplified EM field is completely concentrated in the interaction region between the particle and the surface, while the EM field in the pore is significantly weakened. In this case, we can talk about the redistribution of energy in the entire system. As the gap increases to 5 and 10 nm, the maximum amplification values decrease, but it can be observed that the region of highly localized field remains shifted towards the particle. Thus, even as the distance increases, the large particle continues to determine the spatial distribution of the field.

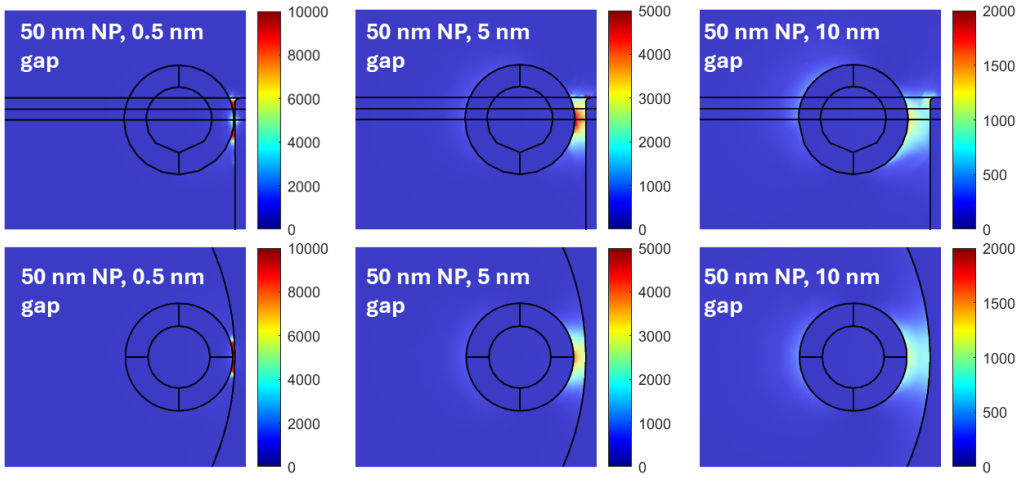

Figure 21 EM field distribution $\frac{E^2}{E_0^2}$ of the pore with 50 nm NP under 780 nm laser excitation

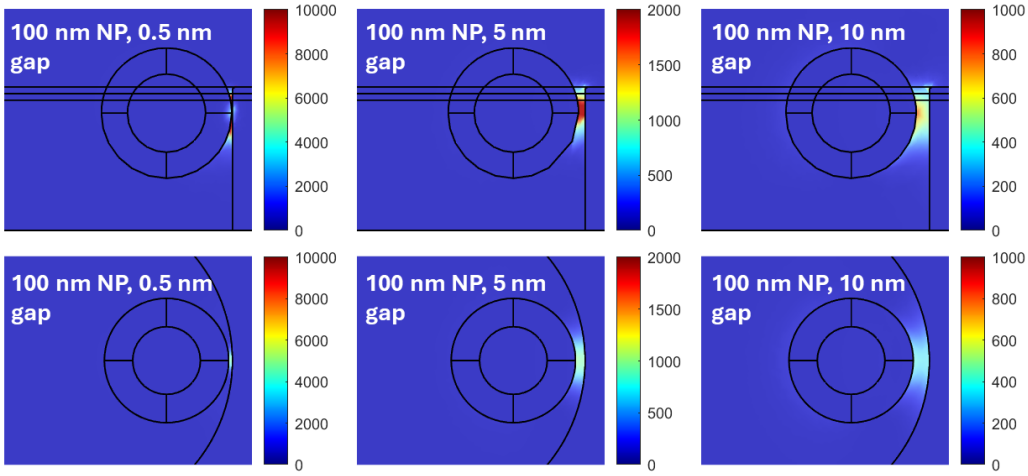

Figure 22 EM field distribution $\frac{E^2}{E_0^2}$ of the pore with 100 nm NP under 780 nm laser excitation

The results of the EM field distribution show that the maximum amplification factor depends primarily on the gap size, and the particle acts as a tool for controlling the scale of this amplification. Small particles, despite their small size, create a strong but localized amplification, while large particles can redistribute the EM field within the channel. This is well correlated with the changes in the transmission spectra (Figure 17). Local amplification has a limited effect on the shifts of the resonance peaks, while the redistribution of the field causes changes in the resonant modes.

Thus, it is the spatial distribution of the enhancement that largely determines the behavior of the system, rather than just its magnitude. These regions of local enhancement directly determine the distribution of heat generation and, therefore, will play a crucial role in shaping the temperature field and subsequent multiphysics effects.

3.5 Temperature distribution in hybrid nanopores

In hybrid nanopores, EM energy absorption occurs predominantly in the metal layers, which are also characterized by strong thermal losses, while the cobalt layer does not significantly contribute to heating, as it is mainly heated by thermal conduction. Thus, the geometry of the structure determines the spatial distribution of heating, while the variable radiation power determines how much the particle and the hybrid pore heat up.

The temperature distribution under 780 nm radiation was studied with a power density ranging from 160 to 1590 W/cm^2. As shown in Figure 23, the temperature distribution under radiation in a nanopore without a particle is formed by optical absorption. In the absence of a particle, the temperature increases smoothly with increasing laser power, but the spatial distribution remains the same, with a maximum at the geometry where the pore opening is concentrated, and then the temperature decreases linearly with distance from the center.

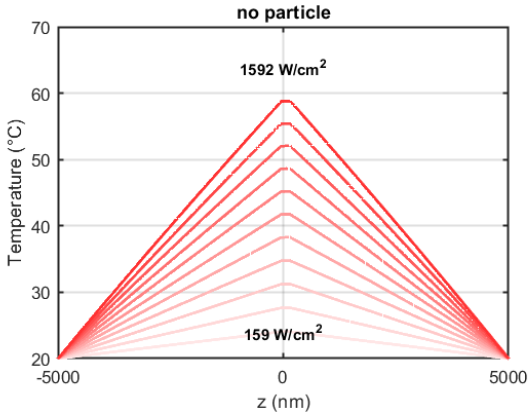

Figure 23 Dependence of temperature inside the bare nanopore (without a nanoparticle) on laser power density

The key result to understand is that the temperature increases linearly with the laser power density: as the intensity increases from 159 to 1592 W/cm², the maximum temperature increases from 30°C

to 60 °C. The shape of the profile remains constant, indicating a stationary heat transfer regime that is also determined by the geometry and other physical properties of the system, which affect the redistribution of energy, while the power determines the amplitude of heat transfer.

With the introduction of a particle in the simulated system, the temperature distribution changes, but mostly with an increase in the particle diameter (Figure 24). Similar to the effects described above, the particle's influence on temperature is not an exception, as it alters the local distribution of $|E|^2$ and, consequently, the distribution of the heat source. However, compared to the electromagnetic field, temperature is more sensitive to changes, as thermal conductivity smooths out local irregularities. As a result, the position and size of the particle lead to noticeable variations in the maximum temperature and profile shape.

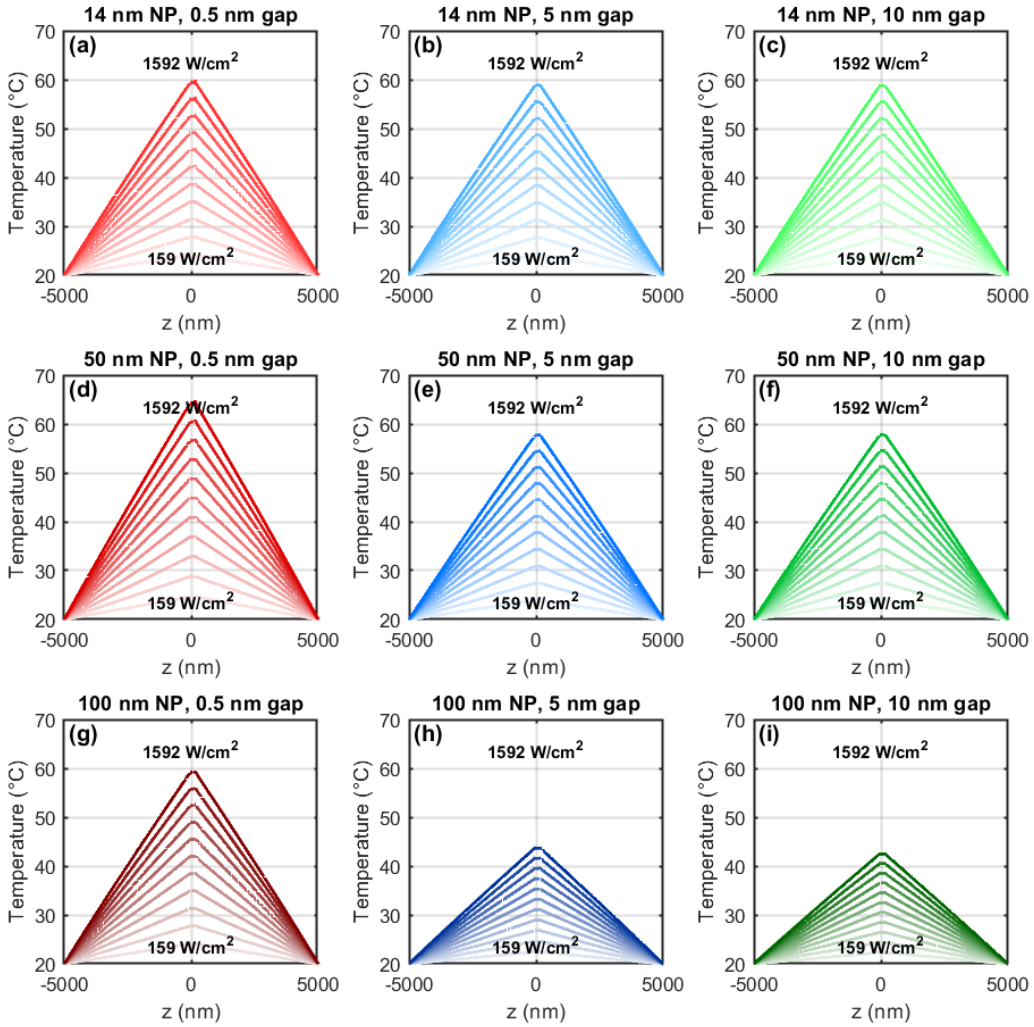

Figure 24 Dependence of temperature inside the nanopore in the presence of a nanoparticle, as a function of particle diameter and gap distance, on laser power density

For small particles with a diameter of 14 nm (Figure 24 a), the temperature distribution is barely different from the case of a nanopore without a particle (Figure 23). Even with a small gap (0.5 nm), despite the strong local field enhancement up to 10^4, the effect on temperature is limited.

Small particles have a negligible effect on the integral heat generation, and the temperature is mostly determined by the pore geometry rather than the presence of the particle. As the gap increases (Figure 24 b-c), there is almost no difference, indicating that small particles play a minor role in shaping the thermal field.

More pronounced changes can be observed for particles with a diameter of 50 nm (Figure 24 d-f). At a gap of 0.5 nm, the temperature increases by approximately 5 degrees compared to the case without a particle. This is due to the fact that the particle itself is larger in area and interacts with a more significant region of the field, increasing the overall effective interaction volume where absorption occurs. As the gap increases, the temperature decreases, which correlates with a decrease in electromagnetic interaction. In this case, the difference with a system without a particle is almost not noticeable.

As it was shown in the case with transmission spectra, particles with a diameter of 100 nm show the most distinct behavior compared to particles of small and medium diameter (Figure 24 g-i). In this case, the temperature distribution differs qualitatively from all previous cases. With a small gap and a large particle diameter, the maximum temperature does not increase, but rather decreases significantly. This is primarily due to the fact that a large particle contributes to the distribution of energy in such a way that it is highly localized in a narrow interaction region and partially reduced within the pore itself. As a result, the overall absorption in the system decreases.

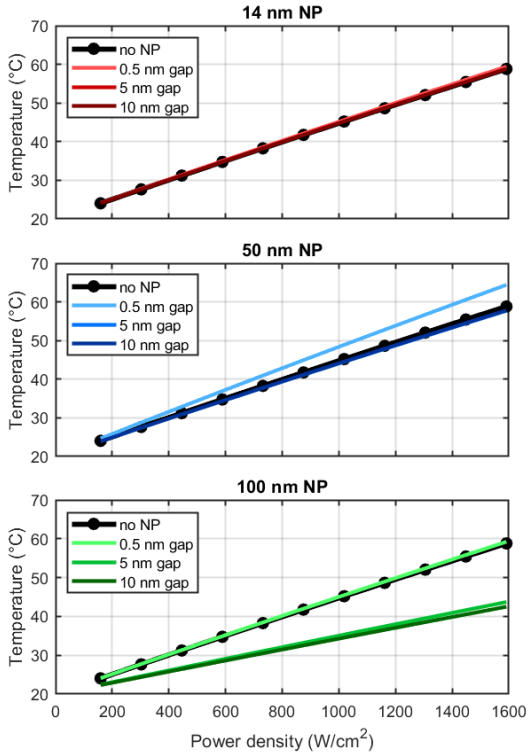

Figure 25 Temperature vs power density

As the interaction distance increases from 5 to 10 nm, the temperature decreases significantly (almost by 45 degrees) compared to smaller particles. This is likely due to the reduced localization of the field in the pore region and the increased localization of the particle, which reduces the efficiency of heating. As a result, the large particle does not enhance heating but rather may suppress it by redistributing energy.

The obtained temperature distributions showed that there is a fundamental difference in spatial scales between the localization of the electromagnetic field and the formation of the temperature profile. The electromagnetic field, which is amplified by the plasmonic response, rapidly decays at distances of the order of tens of nanometers from the surface. At the same time, the temperature still depends on the local heat source, but it also strongly depends on the heat transfer to the surrounding environment, forming a broad distribution that reaches hundreds of nanometers or more. Moreover, it was found that even a highly localized field amplification does not necessarily lead to a proportional increase in temperature, as the contribution to heating is determined not only by the maximum $|E|^2$, but also by the volume of the region where energy is absorbed, as well as the geometry of the nanopore itself.

3.6 Conclusion

In this section, the optical properties of hybrid magneto-plasmonic nanopore have been considered, the distribution of the electromagnetic field inside the pore with and without a particle, and the distribution of temperature. This allows us to gain a comprehensive understanding of the mechanisms of energy localization and redistribution in the system in the presence of a particle for further calculations. It has been shown that the properties discussed are determined not so much by the magnitude of the local field amplification, but rather by the spatial distribution formed by the geometry of the structure and the materials it is made of. We have also examined how the electromagnetic distribution is converted into thermal energy.

The results show that the interaction of a particle with the pore walls can vary from weak to strong, depending on the particle size and distance from the surface. Moreover, despite the observed changes in the EM field distribution and transmission spectrum, the particle's influence on the temperature field is relatively minor. Even when the EM field is highly localized (with a distance of less than 5 nm between the particle and the pore wall), the temperature profile remains similar

to that of a hybrid pore without a particle, especially for smaller particles. This is because the temperature in this system is primarily determined by the nanopore and its geometry, rather than by the local maxima of $|E|^2$.

The calculated results are fundamentally important, as they show that in the system under consideration, the presence of a particle does not lead to dramatic changes in the temperature distribution, despite the strong local redistribution of the electromagnetic field. This is particularly useful when transitioning to magnetic trapping simulations, where the system is simplified to use the temperature distribution calculated for a structure without a particle, without compromising physical accuracy. This simplifies the task by eliminating the need to consider the particle's inverse effect on the thermal field, which can be challenging to implement in real-world settings.

The calculated results show that plasmonic nanopores are highly sensitive to local changes in the dielectric environment, which can be observed through the optical response even for particles with small diameters. This makes such structures attractive for single molecule detection, where the detection system must be sensitive to even small disturbances. It is important to note that the distribution is relatively stable, as the temperature can be controlled based on the radiation used or adapted to suit the needs of the system without critically affecting the objects being studied.

For further calculations of the magnetic field and its effect on trapping, one of the important factors is the dependence of magnetization on temperature. Since it has been established that the temperature in the system is primarily determined by the geometry of the nanopore and the radiation power, rather than by the presence of a particle, this allows us to consider the magnetic distribution as a function of external parameters. On the other hand, this means that the magnetic field and its gradients can be calculated with and without the particle, and then used to analyze the forces acting on the particle.

The spatial inhomogeneity of temperature also affects the inhomogeneity of magnetization, creating magnetic field gradients. These gradients determine the magnetophoretic forces that interact with the particle during trapping. Thus, plasmonic heating serves as a tool for controlling the magnetic field through temperature changes, in addition to directly generating magnetic forces.

The particles themselves have different magnetic moments depending on their size. In the trapping problem, it is the properties of the particle (size and magnetic moment) that determine its response to a given magnetic field, while the field itself is generated independently of the particle. This separation of roles allows us to consider the system in a simplified setting, where the field is predefined and the particle is a passive object moving within the field.

So far, it has been established that the multiphysics is divided into several stages: calculating the optical and temperature fields without a particle, determining the magnetic response, and then trapping the particle.

4. MULTIPHYSICS MODELING OF MAGNETO-PLASMONIC TRAPPING OF CORE–SHELL NANOPARTICLES IN A PLASMONIC NANOPORE

4.1 Introduction

The ability to not only detect, but also control or, in other words, manipulate the transport of nanoscale objects is one of the key challenges in research related not only to nanopores, but also to other nanoscale biosensing and lab-on-chip systems[118,119]. In particular, nanopores, which are the primary focus of this work, have the potential to perform single-molecule analysis, as well as control the transport of nanoparticles and locally manipulate objects within sub-wavelength volumes.

Hybrid magneto-plasmonic nanopores, as already discussed in Chapter 3, are capable of strongly localizing the electromagnetic field near the nanopore edge and walls by exciting localized and surface plasmonic modes. This is due to the formation of plasmonic hotspots, which contribute to high field gradients and, consequently, optical gradient forces. This is an ideal starting point for trapping nanoparticles in a hybrid nanopore. The specific geometry of the nanopore further enhances the spatial confinement of the field and allows for the localization of the trapping region within a confined nanofluidic volume.

Optical trapping is famous for its high efficiency, but there are a number of limitations[120]. For large particles (100 nm or more), the influence of Brownian motion and viscous drag increases. Increasing the laser power not only enhances optical confinement, but also leads to increased plasmonic heating and thermal gradients, which can destabilize the trapping.

One of the solutions to overcome the limitations and increase the trapping capability is the use of magneto-plasmonic systems, where the optical and magnetic properties together can effectively control nanoscale objects. This work focuses on Fe_3O_4@Au core–shell nanoparticles, where the magnetic properties are provided by the Fe_3O_4 core with the ability to attract particles over long distances, while the gold shell (as gold is known to be an ideal plasmonic material) provides strong EM field confinement when interacting with the nanopore walls due to the localized near-field.

In such systems, trapping depends not only on the optical and magnetic forces acting on the particle, but also on viscous drag and thermally induced transport, which can change the course of

the process. For example, thermophoretic drift, which occurs due to strong local plasmonic heating, can induce trapping destabilization and particle escape from the hotspot region.

Nowadays, the experimental study of such systems is also known as a non-trivial task, as the direct simultaneous analysis of electromagnetic fields, magnetic fields, temperature gradients, and nanoparticle dynamics requires significant effort and specialized equipment. Therefore, the study of magneto-plasmonic trapping requires the use of multiphysics modeling, which combines electromagnetic simulations, magnetic field calculations, heat transfer modeling, and particle tracing dynamics to predict the possible behavior of the system and assist in the interpretation of the results.

In this chapter, a comprehensive multiphysics simulation of magneto-plasmonic trapping of Fe_3O_4@Au core–shell nanoparticles in a plasmonic nanopore is performed. The optical and magnetic trapping forces, thermophoretic effects, trajectories of nanoparticles, and the influence of particle size and laser power on trapping capabilities are investigated.

4.2 Description of the multiphysical model

Geometry and materials

The hybrid magneto-plasmonic structure is a 250 nm nanopore array in a multilayer Au/Co/Au/SiN membrane with a 250 nm period. The environment is assumed to be water, where the flow and speed are not controlled externally.

Fe_3O_4@Au core–shell nanoparticles of three sizes were selected as trapping objects based on published data and their potential for trapping:

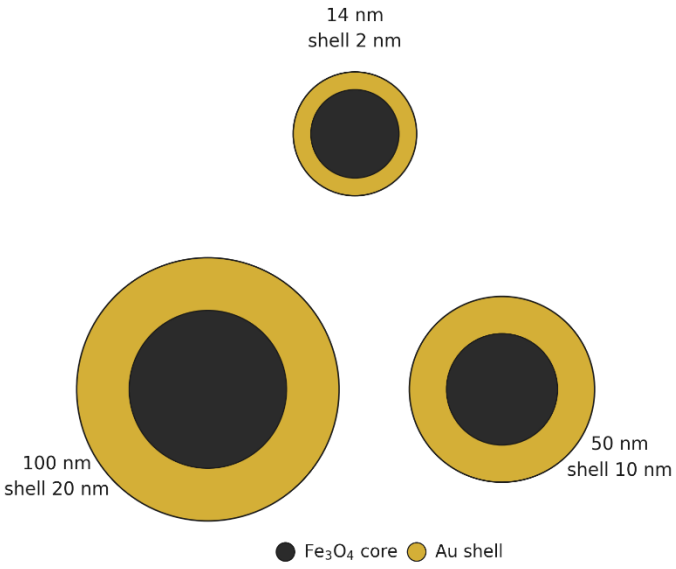

Figure 26 Core-shell nanoparticles

The gold shell provides plasmonic properties, while the magnetic core of Fe_3O_4 determines the magnetophoretic response of the particle. More details about nanoparticles can be found in Chapter 2.

Forces acting on a particle

The particle's motion was taken into account when considering several physical forces (Eq. 10):

$$F_{total} = F_{opt} + F_{magn} + F_{therm} + F_{drag}$$

Assumptions during calculations

As mentioned in the Methods and Workflow section, in this work, the particle was considered during the calculations as a point-particle approximation, where it is represented as a point object moving in pre-calculated fields that define the trapping conditions. This approach is justified by the features of the software.

Moreover, due to this assumption the following effects were not considered:

- partilcle's influence on surrounding electric and magnetic fields;

- Brownian motion;
- hydrodynamic wall effects;
- possible interparticle interactions.

First, the electromagnetic field distribution was calculated based on the laser power to determine the location of hot spots and the temperature gradient. Then, the magnetic field distribution was calculated based on the temperature dependence of the magnetic properties. The resulting fields were used to calculate the optical, magnetic, and thermophoretic forces acting on the particle. More information on the calculations and boundary conditions can be found in the Methods and Workflow section.

4.3 Spatial localization of traps

Localization of plasmonic "hot spots"

When the hybrid magneto-plasmonic structure is optically excited by electromagnetic radiation, highly localized plasmonic modes are created near the edges of the pore, as shown in Chapter 3. As a result, a highly localized EM field is created near the edges of the nanopore, as can be seen in Figure 28.

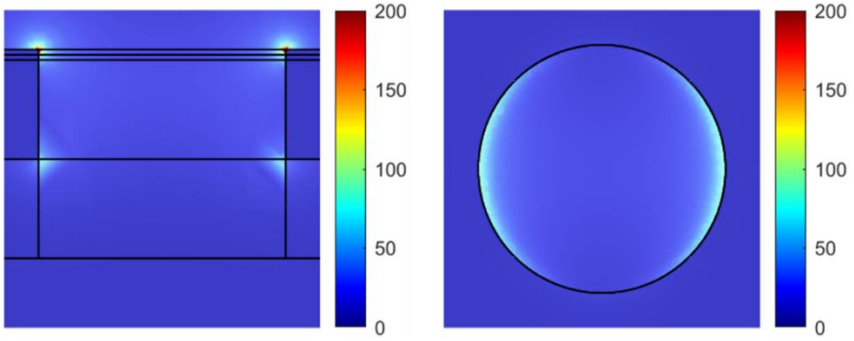

Figure 27 EM field enhancement $\frac{E^2}{E_0^2}$ in bare hybrid nanopore (distribution in XY and XZ planes (D=250 nm, P=550 nm). Reproduced from Figure 18 (Section 3.2):

It is at the plasmonic hotspots that the maximum field gradients occur, which determine the localization of the optical trapping forces.

Spatial distribution of the magnetic field

Like the EM field, the magnetic field also demonstrates localization near the nanopore walls (Figure 29), but in a different region corresponding to the cobalt layer.

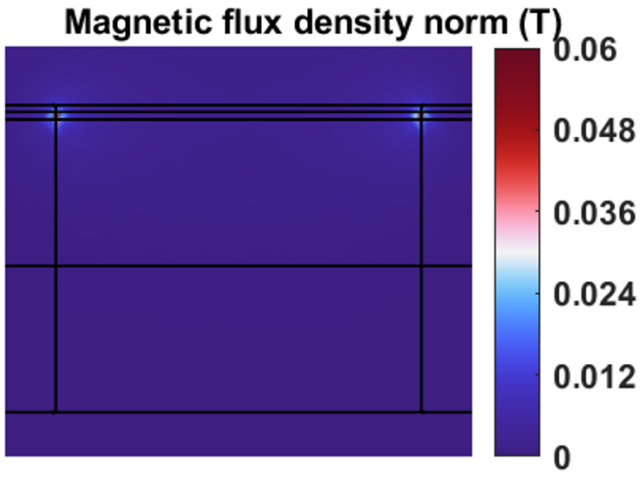

Figure 28 Distribution of the magnetic flux density norm |B| in the plasmonic nanopore region

As can be seen in Figure 29, the maximum values of |B| spatially overlap with the plasmonic hotspot regions (Figure 28), which potentially makes the combined action of optical and magnetic trapping a strong mechanism for particles trapping.

Spatial localization of trapping-related field gradients in the nanopore region

To examine the spatial localization of the trapping mechanisms in more detail, the distributions of the electromagnetic and magnetic fields were calculated along the central z-axis of the nanopore, and special attention was paid to analyzing the distributions of the corresponding field gradients along a line located as close as possible to the edge of the nanopore (coordinates $x = -124, y = 0$), since the optical trapping force and the magnetophoretic force are determined by spatial gradients $| E |^2$ and B^2.

Figure 30 shows the distributions of B^2, $| E |^2$, and their spatial derivatives along the central axis of the nanopore and the line close to the edge of the pore.

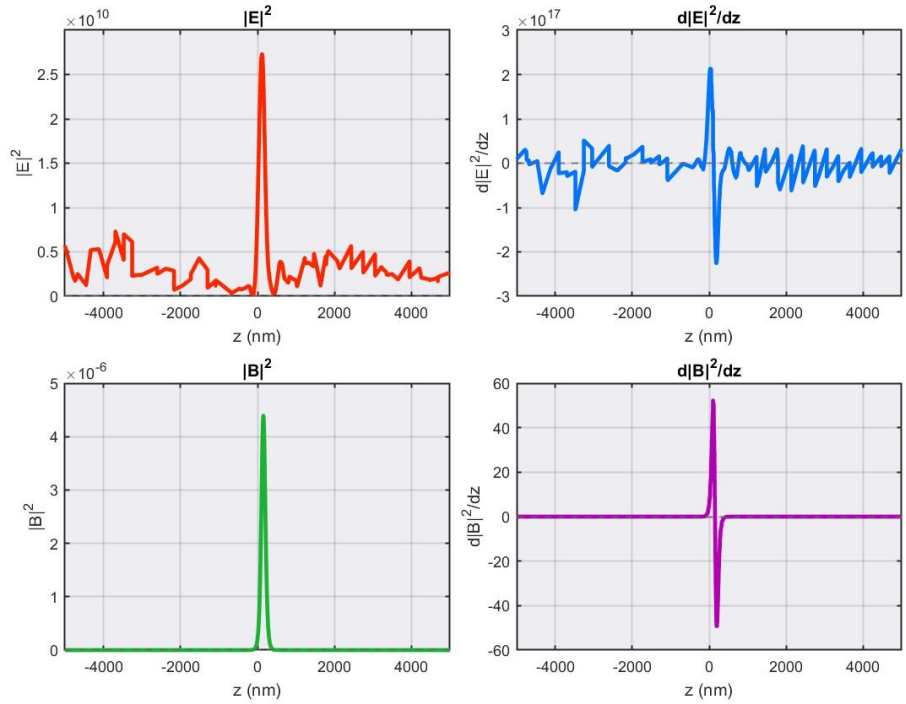

Figure 29 Electric and magentic field gradients in different nanopore regions

The analysis of the distributions $d(|\ E\ |^2)/dz$ and $d(B^2)/dz$ once again shows that in this region that the maximum trapping-driving gradients occur, which determine the optical and magnetophoretic trapping forces. As the distance from the edges of the nanopore increases, the field gradients decrease more rapidly, thereby reducing the trapping efficiency.

The overlapping of electromagnetic and magnetic fields at the edges of the nanopore forms a stable trapping region for Fe_3O_4@Au core–shell nanoparticles.

Potential energy landscape

To quantify trapping capabilities, it is necessary to evaluate the potential energy, which is primarily determined by optical and magnetic trapping mechanisms. This analysis of the potential energy landscape allows for the identification of the spatial localization of the trapping region, where the depth of the trap, as well as the size of the particle and the intensity of the laser radiation, critically influence the trapping conditions. As in the previous section, these values were calculated in different areas of the nanopore (in the center and at the edges of the nanopore).

In this work, the magnetic and optical components of the potential energy were calculated separately for each particle, as well as for different laser powers. The magnetic potential was determined by the distribution of the magnetic field within the nanopore region, while the optical potential was calculated based on the spatial distribution of the electric near-field intensity.

Figure 31 shows the magnetic trapping potential distributions for particles of different diameters. Figures 32-34 show the optical trapping potentials for particles with diameters of 14, 50, and 100 nm at different laser powers (the potential energy calculated for all power densities is listed in SI).

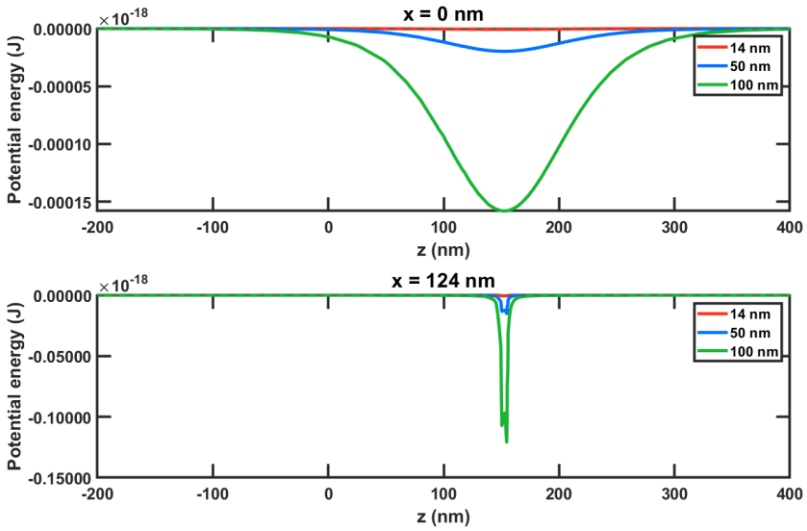

Figure 30 Magnetic potential

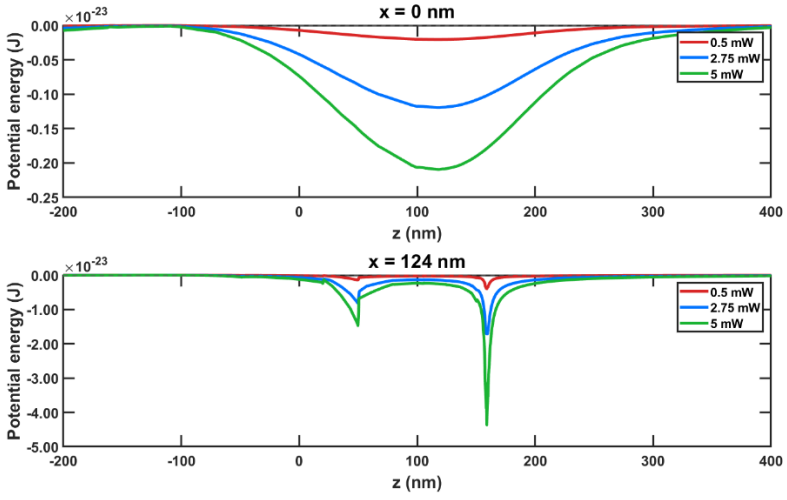

Figure 31 Optical potential for 14 nm NP

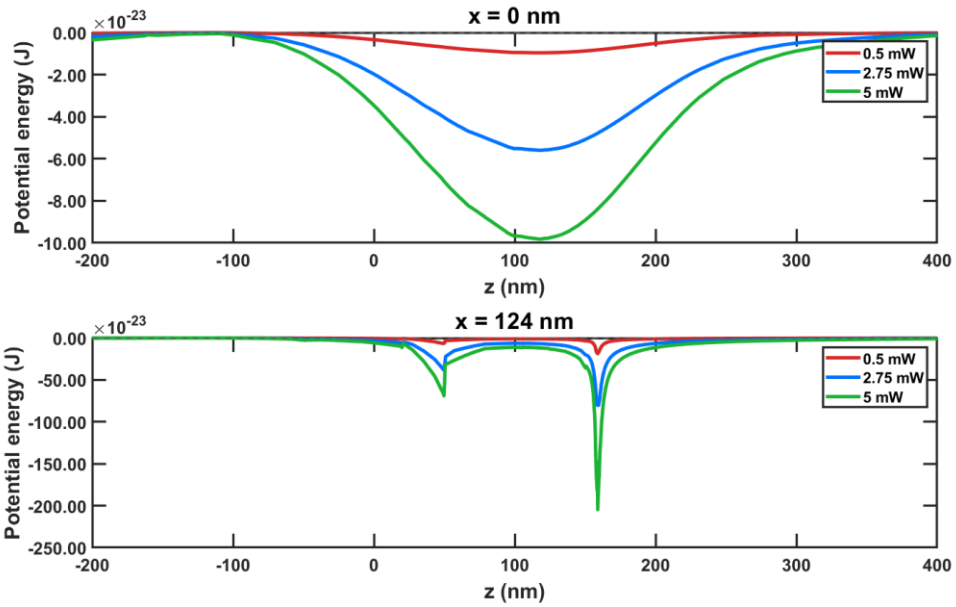

Figure 32 Optical potential for 50 nm NP

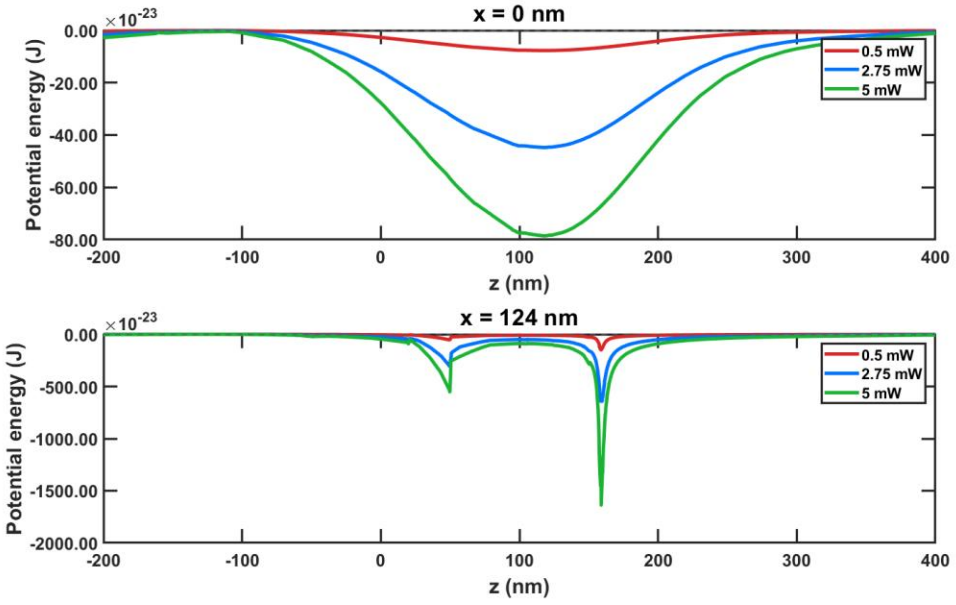

Figure 33 Optical potential for 100 nm NP

The obtained results clearly demonstrate that the magnetic potential contributes to a larger long-range region that forms an attractive region near the nanopore entrance. Moreover, as the particle diameter increases, the trapping potential deepens significantly due to the volumetric scaling of the magnetophoretic interaction.

If we compare the smallest (14 nm) and the largest (100 nm) particles, the magnetic trapping potential remains relatively weak for the smallest particle, while a significantly deeper potential well is formed for the larger particle, providing stable magnetic confinement.

In Figures 32-34, the optical potential is distributed in such a way that its more localized trapping nature is visible. Compared to magnetic trapping, the optical potential is concentrated more near the walls of the nanopore with a gold layer and is characterized by a sharp decrease in potential energy at the layer transition region.

The bigger the laser power becomes, the more consistent the optical trapping potential becomes for all particle sizes. It is also worth noting that the most pronounced increase in the depth of the potential well is observed for larger particles due to the increase in the effective polarizability of the particles.

Another size dependent parameter that is important to mention is that an increase in size not only contributes to an increase in the depth of the trapping potential, but also to an increase in the spatial localization of the trapping region. For example, for a 100 nm particle, deeper potential wells are formed for both magnetic and optical trapping.

For all the particles considered, the trapping potential tends to be more localized in the nanopore edge region ($x = 124$ nm) compared to the central region of the nanopore ($x = 0$ nm). This further highlights the role of plasmonic effects (both local and collective) in shaping the stable trapping region.

The obtained results prove that magnetic and optical attraction, acting together, can form a stable trapping region near the nanopore edge. At the same time, the depth of the trapping potential is determined by both the particle size and the laser power.

4.4 Magnetic trapping dynamics

Before considering the trajectories of particles affected by optical radiation of different powers, the regime without laser radiation (trapping is affected only by magnetic fields) was initially investigated. In this case, the motion of particles is determined exclusively by magnetophoretic attraction.

The calculations were performed using the Particle Tracing for Fluid Flow module, taking into account the combined effects of magnetophoretic and drag forces. The initial coordinates of the particle release were set at the top of the computational domain, close to the entrance to the nanopore (-75,0,300), to reduce the calculation time, as it is assumed that the particle has already reached this region.

The trapping trajectories of Fe_3O_4@Au core–shell nanoparticles were calculated taking into account their different diameters in a magnetic field. Magnetic, optical, viscous, and thermophoretic forces were considered in the simulations (Figure 30).

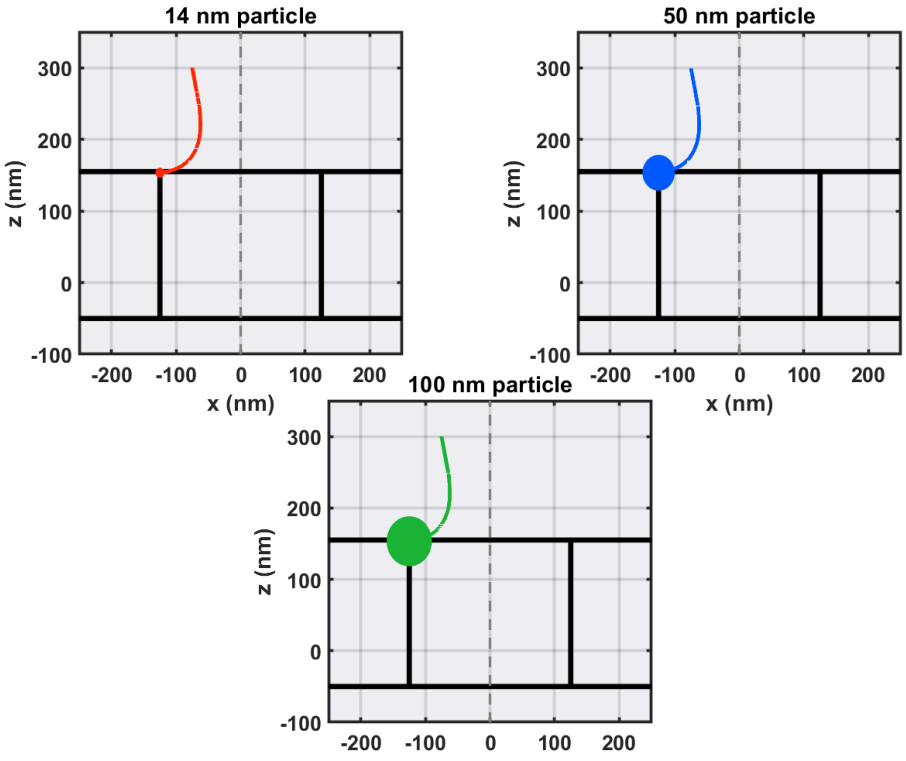

Figure 34 Trajectories magnetic forces

From Figure 35 it can be seen that, first, the trajectories of particles of different diameters have a similar trajectory and are directed towards the same trapping region, which is located near the edge of the nanopore to the left of the center. As previously mentioned, the magnitude of the magnetic force acting on the particles depends on the particle size, but the resulting data can be interpreted correctly and is determined by the specific distribution of force fields in the system, as well as the features of the software itself.

As shown in Figures 32-34, the distribution of forces is determined by the geometry of the nanopore structure and the distribution of local electromagnetic fields near the nanopore. At the same time, parameters such as the position of the plasmonic hotspot and the regions of maximum magnetic gradient are distributed in the pore independently of the size of the particles (since the interaction of the particles with the pore walls is not taken into account when calculating the trajectories). This means that the direction of the resulting force at each point in space remains almost constant.

Thus, it can be concluded that despite the particle diameter, the force field is directed and oriented towards the same trapping region. Changing the particle size during the calculation does not affect the shape of the trajectory, but it does affect the dynamic characteristics of the motion:

- speed of movement;
- trapping time;
- trapping stability;
- thermophoretic drift sensitivity.

It follows that an increase in the size of a particle leads to an increase in its velocity as it approaches the trapping-region. Accordingly, larger particles reach the trap more quickly and may exhibit more stable trapping.

The invariance of the spatial trajectory can be explained by the fact that the trap locations are determined by the geometry of the pore itself, which remains constant for all particles, while the size of the particle determines the efficiency and dynamics of capture.

Another important factor that determines the trajectory is the flow rate of water, which is equal to 0 in this work. Therefore, when considering the system without taking into account optical forces, we can say that in a simplified modeling system, the trajectories of particles are determined more by the geometry and properties of the nanopore than by the properties of the particle itself.

Moreover, small particles are strongly influenced by thermophoretic drift and Brownian motion, which can lead to destabilization trapping at high laser powers, as will be discussed later.

4.5 Magneto-plasmonic trapping dynamics

To analyze the trapping of particles involving both magnetic and optical forces, we performed simulations of the trajectories of Fe_3O_4@Au core–shell nanoparticles in the interface of viscous drag and thermophoretic effects resulting from the plasmonic heating of the magneto-plasmonic nanopore. The simulations were provided for different values of the laser power density (all simulations can be found in the SI section) to investigate the impact of photothermal effects on the trapping of particles near the nanopore walls.

The initial coordinates of the particles were set in the same way as in Section 4.4.

Figures 36-38 show the trajectories of nanoparticles obtained by the combined action of optical and magnetic trapping mechanisms.

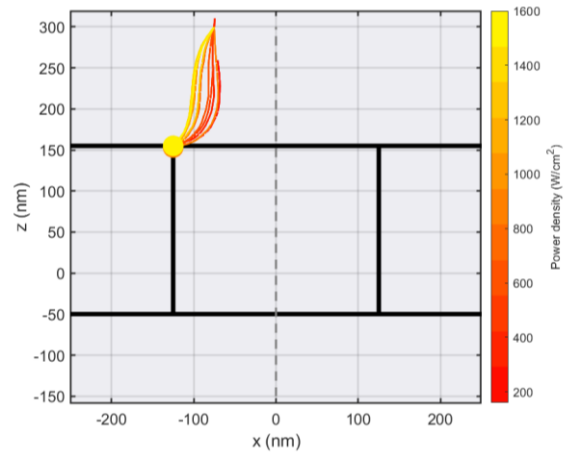

Figure 35 Trajectories for 50 nm NP

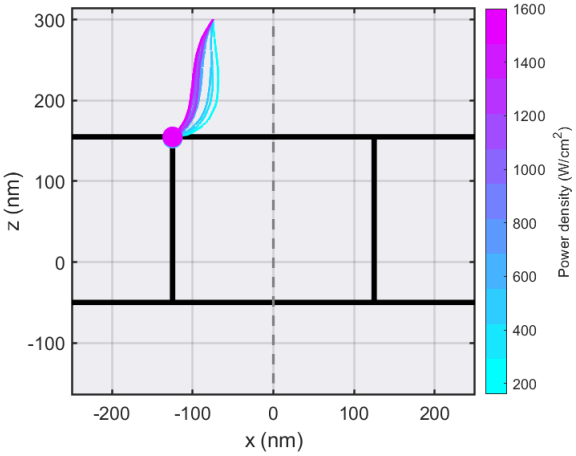

Figure 36 Trajectories for 100 nm NP

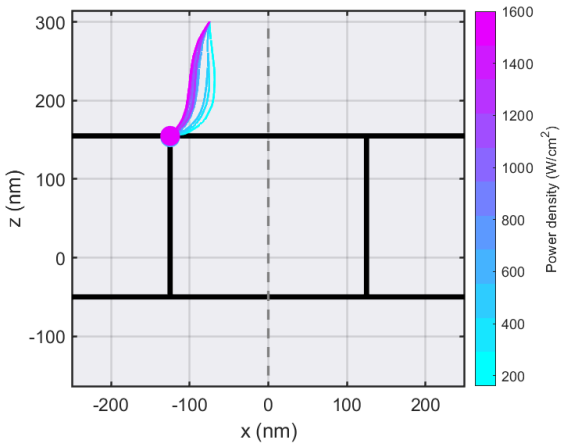

Figure 37 Trajectories for 100 nm NP

As can be seen from Figures 36-38, when optical force is added, the trajectories of the particles change significantly. The resulting plasmonic hot spots and highly localized EM fields at the edges of the nanopore form a trapping region near the nanopore walls, which contributes to a greater deviation of the trajectories towards the plasmonic hotspot.

The most pronounced effect of plasmonic effects is observed for the smallest particle with a diameter of 14 nm (Figure 33). As a result, the particle is more susceptible to photo-thermal effects under the influence of magnetic and optical forces. It has been shown that the thermally induced transport increases with the density of laser radiation. As the power increases, the metal layers of the nanopore heat up, leading to temperature gradients that cause thermophoretic drift. Due to the very small size of the particle and the relatively weak magnetic confinement, these particles are highly susceptible to thermophoretic destabilization.

At the same time, for larger particles (50 nm and 100 nm) (Figures 36-37), a more stable trapping behavior can be clearly observed. In this case, the magnetic force acts as a stable mechanism for particle retention, while the optical trapping enhances the localization of nanoparticles near the nanopore edge with increasing laser power. For these particles, factors such as their size and the magnitude of the force allow magneto-optical forces to dominate over thermophoretic transport even at elevated laser powers.

As in the previous section, it can be noted that for particles of 50 and 100 nm, the shape of the trajectories is almost identical. This is potentially attributable to the absence of externally controlled fluid flow in the model, and the particle's motion is primarily determined by the distribution of forces and the specific geometry of the nanopore. Under these conditions, the differences between the particles manifest themselves in terms of trapping stability, localization strength, and sensitivity to thermophoretic effects.

The results show that the trapping dynamics in a magneto-plasmonic nanopore is determined by a complex competition between optical confinement, magnetic attraction, and thermally induced transport. The particle size plays a key role in determining the stability of trapping and the sensitivity of nanoparticles to photo-thermal destabilization.

4.6 Forces analysis

To understand the mechanisms of particle trapping and the trajectories shown in Section 4.5, a detailed analysis of magnetic, optical, and thermophoretic forces was performed for three particles and different laser powers.

Figure 39 shows the distributions of magnetophoretic, optical, and thermophoretic forces along the nanopore axis and near the pore walls.

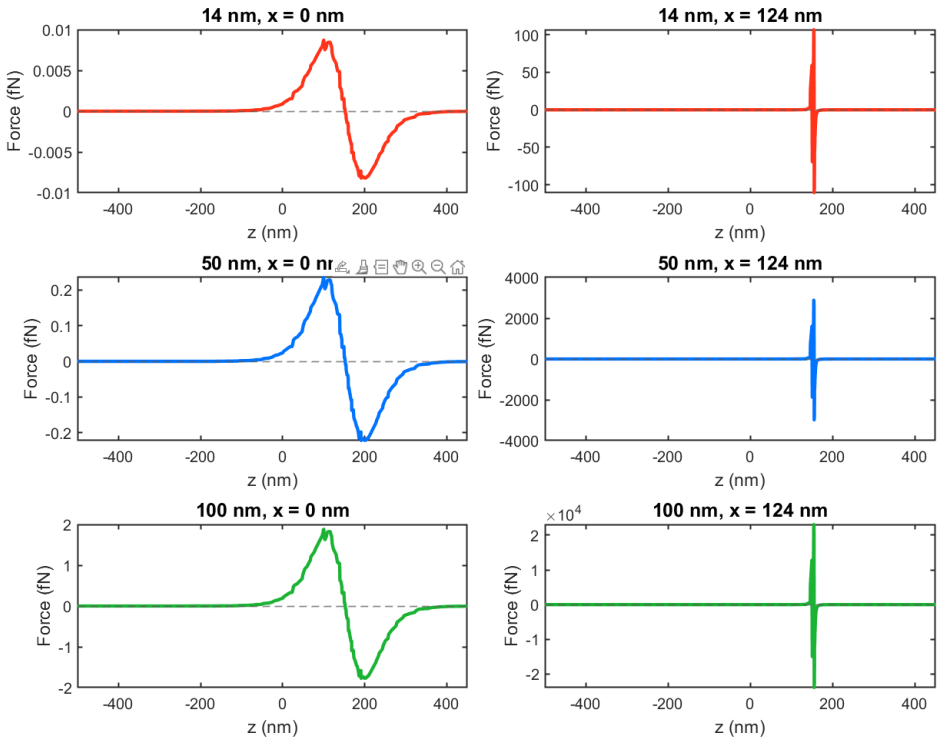

Figure 38 Magnetic force for different particles

Figure 39 shows the distributions of magnetic force for 14, 50, and 100 nm particles. The graphs show that the magnetophoretic force is localized near the nanopore edge, where the magnetic field gradients are highest. The order of the magnetic force for all particles remains approximately the same and differs little, although the magnetic force increases with the size of the particle. For the smallest particle, the magnetic force is relatively small due to the very small volume of the particle.

For 50 nm particles, we can already observe a significant increase in the magnetic force. In this case, we can say that the magnetic force is already capable of causing a stable directional movement of the particle towards the traps in the pore.

As expected, the strongest magnetic force is observed for 100 nm particles. The increase in magnetic force is due to the volumetric scaling of magnetophoretic interaction, and as a result, larger particles are capable of more stable magnetic confinement, which leads to a pronounced deviation of the particle trajectory towards the edges of the pore.

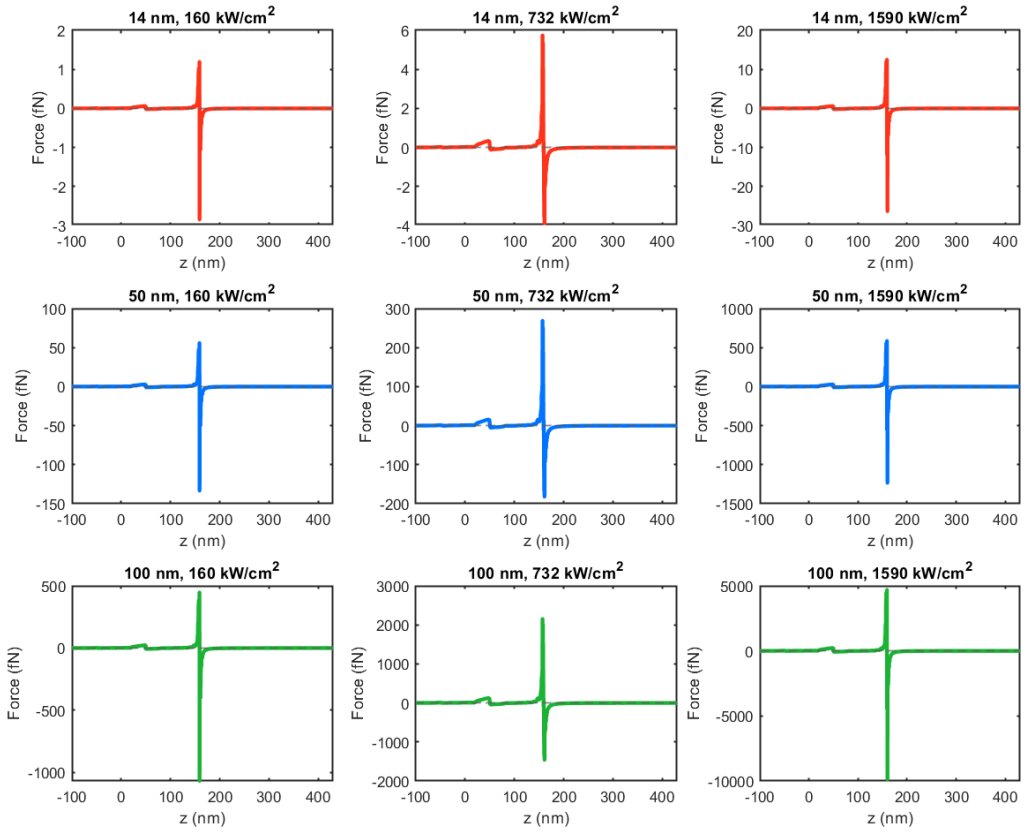

Figure 39 Optical forces near the nanopore wall

Figure 40 shows the optical force distributions for different particle sizes and laser powers at the center and edges of the pore.

Thus, the optical force is characterized by significantly stronger spatial localization near the nanopore edge, in contrast to the magnetic force. As expected, the maximum values are concentrated in the plasmonic hotspot region, where extreme gradients of electric field intensity occur.

It is observed that for all particles, regardless of size, an increase in laser power leads to an increase in optical power, as plasmonic near-field localization is simultaneously enhanced.

The weakest optical force is shown for 14 nm particles. Even though the optical trapping is enhanced by increasing the laser power, small particles remain the most sensitive to destabilizing thermal effects due to the comparatively weak conservative trapping. The largest optical force is observed for particles with a diameter of 100 nm. An increase in effective polarizability leads to a

significant enhancement of optical interaction and the formation of a highly localized trapping region.

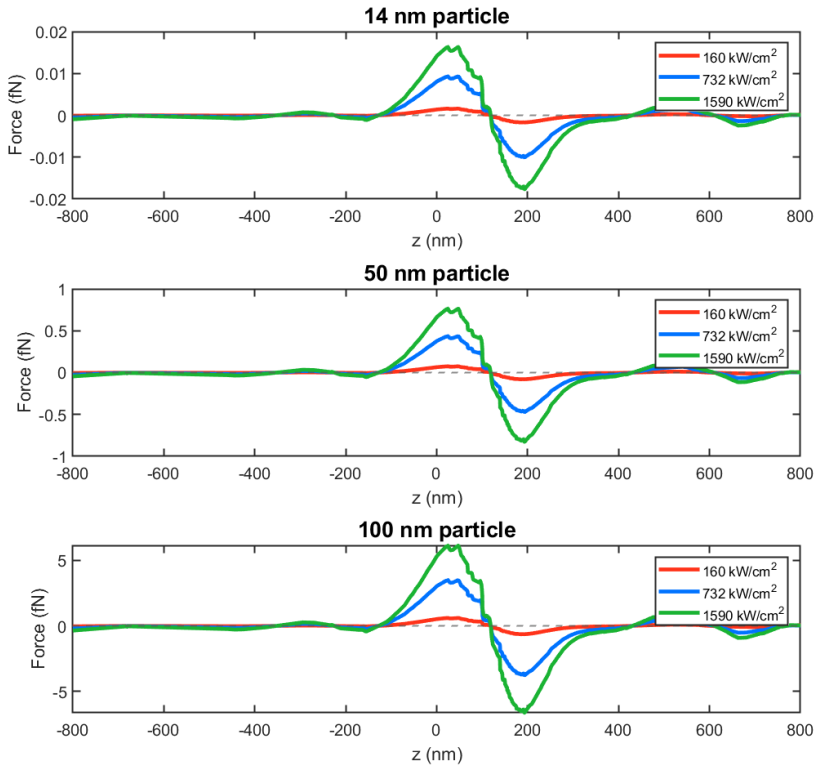

Figure 40 Optical forces in the middle of the pore

It is also must be noted a significant difference in the values of the optical force in the center of the nanopore and near its walls (Figure 40 and 41). In the center of the nanopore, the optical force is distributed more evenly and has comparatively weak gradients, while the main maximum is achieved near the nanopore edge due to the spatial localization of plasmonic hotspots.

This explains the observed localization of particle trajectories near the nanopore edge, as shown in the previous figures. The particles are deflected towards the region of maximum field gradient, where the optical trapping force reaches its highest values.

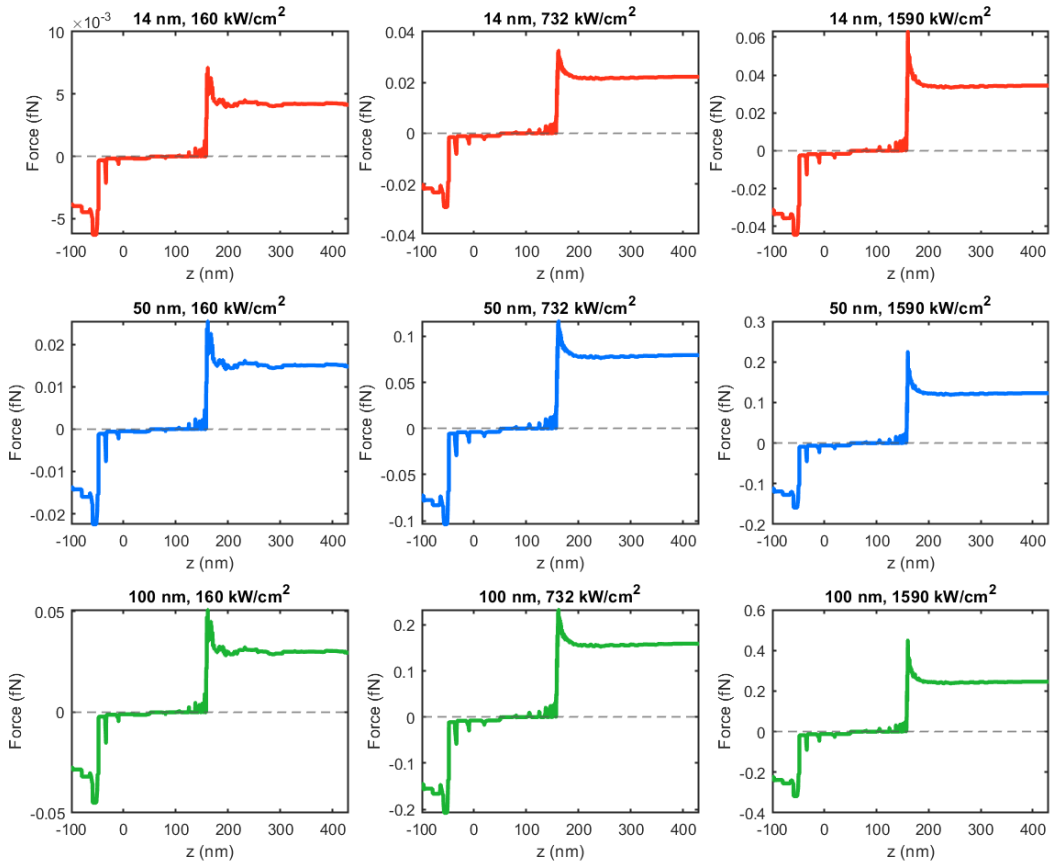

Figure 41 Thermophoretic forces near the nanopore wall

Figure 42 shows the distributions of thermophoretic force near the nanopore wall for different laser powers.

From the graphs, it can be seen that the thermophoretic force increases as expected with increasing laser power due to plasmonic heating and the increase in temperature gradients near the nanopore edge. For 14 nm particles, the thermal effect is the most significant compared to other forces. The small size of the particle and the strong thermophoretic transport cause the particle to be pushed out of the pore due to the strong temperature gradient. This effect explains the drastic change in the trajectory of a 14 nm particle as the laser power is increased (Figure 33). The increased thermophoretic drift leads to additional vertical displacement of the trajectories and partial destabilization of trapping near the hotspot region.

For larger particles of 50 nm or more, the influence of the thermal gradient remains significant, but the optical and magnetic forces still overcome this obstacle and the particle remains trapped.

4.7 Discussion

Numerical multiphysics calculations show that trapping Fe_3O_4@Au core–shell nanoparticles in a hybrid magneto-plasmonic nanopore is the result of a complex interaction between several physical processes, including electromagnetic, magnetic, and thermal effects. Unlike systems where particles are trapped using either optical or magnetic forces, where the localization of the trap is primarily determined by the gradients of the electromagnetic or magnetic field, in the hybrid system under consideration, trapping is the result of a combined effect of magnetophoretic transport and highly localized optical confinement.

The results of the electromagnetic field calculations indicated not only the localization of plasmonic hot spots, but also the formation of highly localized fields at the edges of the pore, where the maximum values of $|E|^2$ and the corresponding field gradients, which affect the optical force, occur. In the case of the optical force, it is these regions that determine the position of the trap and form the trapping area. The analysis of the distributions of $d(|E|^2)/dz$ showed that the optical force is quite strong at the edges of the pore and rapidly decays as it moves away from the nanopore.

Unlike the optical force, the magnetophoretic force has a wider range of action, performing a transport function, and ensures the capture of particles from distant regions to the trap site. Thus, magnetic and optical trapping perform two different but important and fundamental functions: the magnetic field is responsible for transport, while the highly localized EM field localizes the particle in the plasmon hot spot region.

The consideration of three types of particles with different diameters (14, 50, and 100 nm) allowed us to evaluate the dependence of the capture capability on the size of the nanoparticles. As the particle diameter increases, both the magnetic interaction and the optical retention increase, as the forces scale with the increase or decrease in particle size. While the particle size is the primary factor in the magnetic force, the polarizability of the particle is the determining factor in the optical force. Therefore, a 100 nm particle will exhibit the most stable and predictable localization, where the deepest potential wells of retention.

For particles of small diameters, the conservative forces of confinement are much weaker, which makes these particles less resistant to thermal effects. By increasing the laser power, not only does the optical force and the ability to capture increase, but it also causes a strong local heating of the metal layers of the pore, resulting in a strong temperature gradient and, consequently, a change in the trajectories of small particles due to increased thermophoretic transport.

The obtained temperature distributions, in agreement with the EM field distribution maps, showed that the maximum heating is localized near the region of highly localized EM fields. Although the maximum temperature values are not very high, they are sufficient to create temperature gradients and thermophoretic drift, especially in the case of small nanoparticles.

The results of the calculations show that the power of the laser radiation has a dual effect on the stability of the capture, depending on the diameter of the particle. At low powers, optical capture may not be sufficient to capture nanoparticles, while at high powers, thermal destabilization mechanisms may dominate, depending on the size of the particle. Therefore, stable capture is a result of careful planning and consideration of all the physical properties of the system under study, where a properly selected radiation source provides sufficient capture forces to overcome the thermophoretic contribution.

It is important to note that in the performed calculations, the electromagnetic and thermal fields were calculated without taking into account the interaction with the nanoparticles themselves, which directly affect the field distribution. Within the framework of the point particle approximation, the nanoparticles were considered as material points moving in pre-calculated force fields.

Meanwhile, in a real system, the presence of a nanoparticle inside a nanopore close to its walls can change the local electromagnetic response of the system. It was also estimated in Chapter 3 that Core-shell particles of Fe_3O_4@Au can further enhance the local field due to the plasmonic interaction between the edge of the nanopore and the gold shell of the nanoparticle. As a result, there is an additional enhancement of the local field, a redistribution of the optical confinement forces, and a change in temperature due to the plasmonic properties of the particle. Thus, large nanoparticles can significantly affect the local temperature distribution, redistributing the

temperature within the pore. The gold shell of Fe_3O_4@Au, with its plasmonic properties, acts as an additional local heating source. In real experiments, this can lead to:

- additional local heating;
- changes in temperature gradients;
- enhancement of thermophoretic transport;
- changes in the viscosity of the medium.

Most probably these effects are most pronounced for larger particles, as their size becomes comparable to the size of the region near the nanopore, where strong EM field gradients are concentrated. Under these conditions, the trapped particle can redistribute electromagnetic fields by participating in plasmonic interactions with the nanopore.

Another limitation of the model may be the lack of consideration of Brownian motion. For nanoparticles, especially those of small diameters, thermal fluctuations have a critical impact on the retention dynamics. This may be particularly evident for particles with a diameter of 14 nm, as the potential wells of the trap remain relatively shallow. In real experiments, Brownian diffusion leads to the chaotic displacement of nanoparticles within the trap region, significantly reducing the retention time and, in critical cases, causing the particle to escape from the trap.

In addition, the model did not consider the flow of the liquid. On the one hand, this helps to see the trajectories of the particles under the influence of the forces determined by the geometry of the nanopore, but on the other hand, in real nanofluid systems, convection, electroosmotic flow, and local thermally induced fluid motion can significantly change the dynamics of particle transport.

However, despite these limitations, the calculations allowed us to see the main physical mechanisms that determine magneto-plasmonic trapping in nanopores, as well as to track and analyze the role of particle size, laser power, and thermal effects in shaping the stability of trapping.

The obtained results demonstrate the potential of magneto-plasmonic nanopores for controlling the transport of nanoobjects and their localization in traps, selective capture, biosensing, single-

particle analysis, and nanofluidic applications, with the ability to adjust and control parameters for transport mechanisms.

Further research can be focused on accounting for the redistribution of the nanoparticle-induced field, particle-field interactions, Brownian dynamics, hydrodynamic transport, and collective effects during the simultaneous confinement of multiple nanoparticles in plasmonic nanopore systems.

4.8 Conclusions

In this chapter, the multiphysics magneto-plasmonic trapping of Fe_3O_4@Au core–shell nanoparticles in a hybrid magneto-plasmonic nanopore was simulated. It was demonstrated that the particle trapping is determined by both magnetophoretic transport and the localized EM field and temperature gradient caused by plasmonic heating.

It has been found that an increase in the diameter of the trapped particles leads to an increase in the probability of particle capture and retention, while for small nanoparticles, the probability of capture is strongly influenced by thermophoretic transport. It has been shown that an increase in the laser power density both enhances optical trapping and promotes plasmonic heating, creating a competition between trapping forces and thermal destabilization.

5. Three-Dimensional Nanopores for ICR and EM field confinement

5.1 Introduction

Unlike the well-studied 2D nanopores, three-dimensional nanopores are currently of particular interest for nanofluidics, plasmonic nanophotonics, and biosensor systems, as nanopores provide an opportunity to control electrical, ionic, optical, and thermal processes in subwavelength volumes[121,122]. Unlike 2D structures, the three-dimensional geometry of a nanopore exhibits pronounced spatial localization of physical fields in the aperture region, thereby enabling the controlled transport of nanoscale objects within a confined volume.

Plasmonic nanopores are usually of particular interest, as the metallic coating of the nanopores excites localized surface plasmons. As a result, regions of highly amplified localized electromagnetic fields are formed at the edges of the nanopore. This localization of high-intensity fields contributes to the creation of high gradients, which determine the optical response of the system and also affect local heating and, consequently, interactions with molecules and nanoparticles.

This chapter focuses on numerical calculations and the relationship between the geometry of a three-dimensional nanopore and the distribution of physical fields within the pore. The 3D shape of a nanopore directly affects ion transport, electromagnetic field localization, temperature distribution, and most importantly, the efficiency of optical amplification. Therefore, numerical simulations are an essential tool for studying such systems.

5.2 Modeling workflow

Nanopore's geometry

In the calculations, the geometry of the Al_2O_3 and SiO_2 nanopores under consideration is described as three-dimensional cone-shaped nanopores with wall shapes that are characterized as concave, straight, and convex. This shape was chosen based on experimental data. The SEM images of the 3D nanopores (Figure 43) were used to account for and replicate the geometry for the calculations.

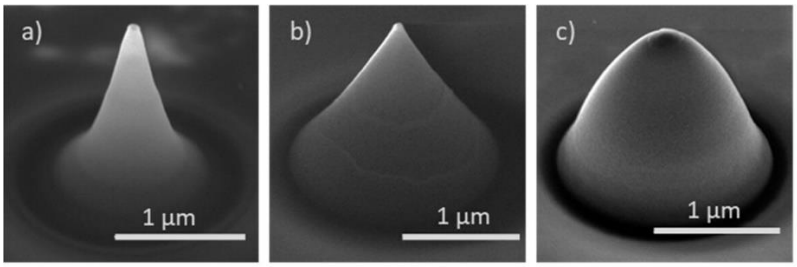

Figure 42 Electron microscopy analysis of metal oxide nanopores with different shapes. SEM micrographs of Al_2O_3 nanopores with concave (a), straight (b), and convex (c) edge profiles

The geometry of the structure is determined by the half-angle of the cone in the aperture region of the nanopore. Thus, various profiles with angles ranging from 15° to 80° were investigated, as this allows for the study of the influence of nanopore shape on the spatial distribution of physical fields.

The diameter of the narrowest pore opening varied from a few nanometers to tens of nanometers, while the channel length was characterized by a length of 1 micrometer.

For modeling ion transport, calculations were performed in 2D axisymmetric, while for calculating the EM field enhancement and temperature distribution in plasmonic nanopores, calculations were performed in 3D.

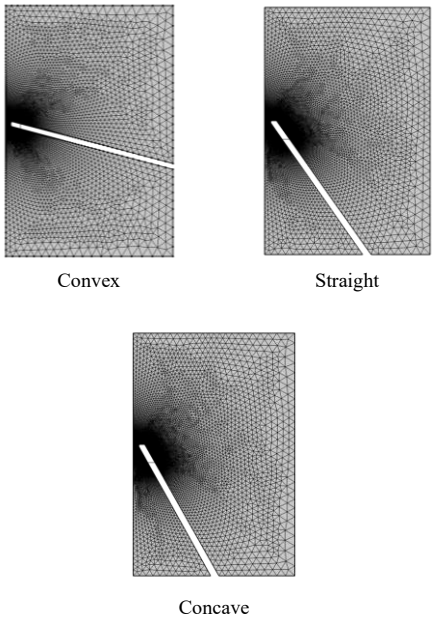

Figure 43 Geometry and mesh of modelling system in COMSOL[122]

The use of different geometric profiles allows us to understand the effect of nanopore shape on the distribution of electric field, temperature gradients, and transport properties of the system.

5.3 Modeling of ICR in 3D nanopores

The numerical simulations of ionic transport through the nanopore were provided using COMSOL Multiphysics software. The size of the simulation boxes (Figure 44) are 1200×800 nm for straight, convex and concave Al_2O_3 and SiO_2 nanopores. The reservoirs are filled with water solution consisting of KCl electrolyte (Table 1). The thickness of all the nanopores is 30 nm. The diameter of the open part of the nanopore for simulations was 76 nm for Al_2O_3 and 44 nm for SiO_2 nanopores. A triangular mesh was applied to the whole model. The minimum and maximum mesh sizes, that were set on the interior walls of the nanopore, were equal to 0.1 nm and 1 nm, respectively.

Table 1 – Diffusion coefficients and molar concentration of ions in electrolyte solution[122]

Ion	Diffusion coefficient, m^2/s	Molar concentration
K^+	1.96e-9	10 mM
Cl^-	2.03e-9	

The temperature of the system was set as $298\ K$. The dielectric constants of water was equal to 80. The applied voltage varies from -1V to 1V. The surface charge density of Al_2O_3 was set from -0.06 to -0.1 C/m^2 and for SiO_2 from -0.02 to -0.04 C/m^2. The surface charge was applied on the tip of the nanopore (both inside and out).

To describe the behavior of ionic current occurs in nanopore in electrolyte solutions Poisson-Nernst-Planck (PNP) equations (Eq. 2, 3, 4, 5) were used. Equations explain the behavior of the electric potential on the entire domain (Poisson equation, Electrostatics module) and ion flux in the electrolyte solution (Nernst-Planck, Transport of Diluted species module, fluid domain only).

PNP equations were coupled together using Multiphysics coupling in COMSOL (Space charge density coupling, Potential coupling). The ion current inside of the narrowest of the nanopore was calculated using:

$$I = \int \left(z_1 \vec{J}_1 + z_2 \vec{J}_2\right) \cdot \vec{n} dS \qquad (30)$$

Electric potential (working and ground electrodes) and fixed concentration boundary conditions were applied on top and bottom parts of reservoirs (top as a working electrode, bottom as a ground). The space charge density of electrolyte solution according to the Nernst-Planck equation describes the excess charge of solution in presence of ions. It was set on the whole domain containing water electrolyte solution.

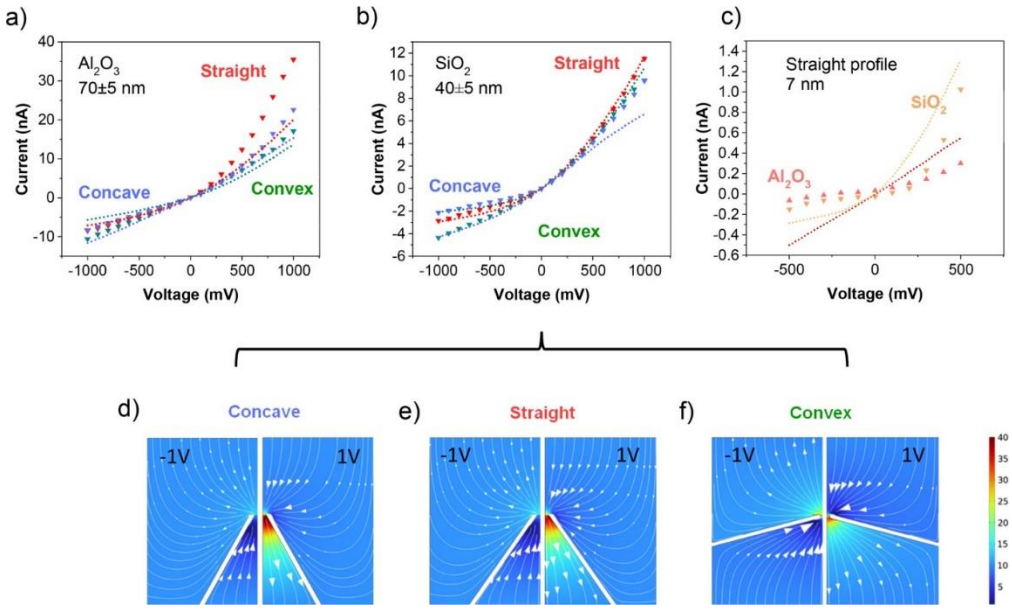

Figure 44 Ionic current rectification: measured (triangles) and simulated (dotted lines) I–V characteristics of the three nanopore geometries in a 10 mM KCl electrolyte. (a–c) Current voltage curves for nanopores with different shapes and materials as described in the legends. (d–f) Simulated concentration profiles of K^+ [mol/m^3] and total flux (streamlines) for a SiO_2 nanopore with 40 nm diameter with (d) concave, (e) straight, and (f) convex profile[122]

Figure 45 shows the experimental and calculated results of a study of ion current rectification in three-dimensional dielectric nanopores of various geometries. Nanopores with concave, straight, and convex wall profiles formed on the basis of Al_2O_3 and SiO_2 were considered. To interpret the experimental data, numerical simulation using the finite element method was additionally

performed using the Poisson–Nernst–Planck equations describing the distribution of electric potential, ion concentrations, and ion flux density inside the nanochannel.

Figures 45 a and b show the volt-ampere characteristics of the studied nanopores in a 10 mM KCl solution. For all structures, there is a pronounced nonlinearity and asymmetry of the current dependence on the applied voltage, which indicates the presence of an ion rectification effect. With a positive bias, the current value is significantly higher than with a negative polarity. This behavior is associated with the asymmetric redistribution of ions inside the conical nanopore and the difference in the processes of accumulation and depletion of charges depending on the direction of the external electric field.

The most pronounced rectification effect was obtained for nanopores with a straight wall profile. For structures made of Al_2O_3 with a diameter of about 70 nm, the current at positive voltage significantly exceeds the values observed for concave and convex geometries. A similar trend persists for SiO_2 nanopores with a diameter of about 40 nm. This indicates that the shape of the nanochannel has a decisive effect on the local distribution of ion fluxes and the formation of conduction asymmetry.

Particularly strong straightening is observed for small-diameter nanopores. Figure 45c shows the results for straight nanopores with an aperture of about 7 nm. In this case, the channel size becomes comparable to the thickness of the double electric layer, as a result of which the surface charge of the walls begins to dominate the bulk ion transfer. The overlap of the electric double layers leads to a significant change in the distribution of ion concentration inside the nanopore and a sharp increase in the asymmetry of conductivity. Rectification coefficients of the order of 7 were obtained for SiO_2, while for Al_2O_3 they were about 4.9, which significantly exceeds the values typical for planar nanopores.

To clarify the physical nature of the observed effect, the spatial distributions of the ion concentration K^+ and the lines of the total ion flux were calculated. The corresponding results are shown in Figures 45d–45f. The color maps reflect the local ion concentration, and the current lines show the direction of charge transfer within the system. The simulation demonstrates that the key parameter is the opening angle of the nanopore near the aperture. For concave structures, it is

minimal, for straight lines it occupies intermediate values, and for convex structures it reaches maximum values.

Changing the angle of the walls significantly affects the nature of mass transfer inside the channel. At small opening angles, ion transport inside the nanopore becomes more limited, which leads to increased accumulation or depletion of charges at different voltage polarities. As a result, states of high and low conductivity are formed, providing a pronounced rectification effect. For convex geometries, the transfer between the inner and outer regions of the nanopore becomes less limited, as a result of which the asymmetry of the ion concentration distribution weakens.

The nanopore material and the amount of surface charge have an additional effect on the transport characteristics. In the numerical model, lower surface charge densities were used for SiO_2 compared to Al_2O_3, which led to varying degrees of ion rectification. A change in the surface charge directly affects the distribution of the electric potential near the channel walls and, as a result, the local ion concentration and the conductivity of the nanopore.

Thus, the results show that the transport properties of three-dimensional nanopores are determined not only by the size of the aperture, but also by the complex interaction of channel geometry, surface charge, and local electric field distribution. Controlling the shape of the nanopore and the choice of dielectric material make it possible to purposefully change the characteristics of ion transfer, which opens up opportunities for creating highly sensitive nanofluidic sensors, memristor devices, and single-molecular analysis platforms.

5.4 Modeling of electromagnetic processes in 3D plasmonic nanopores

In this work, numerical modeling was used to analyze the localization of the electromagnetic field, thermal effects, and the interaction of molecular fluorophores with a plasmonic nanostructure. The focus was on studying the distribution of local fields in the aperture region of a three-dimensional nanopore and the impact of the structure's geometry on fluorescence enhancement and quenching processes. All calculations were performed using the finite element method in the COMSOL Multiphysics software environment.

The system under study was a conical nanopore formed in a dielectric membrane and coated with a metallic gold layer. Additionally, a hybrid structure consisting of gold and silicon regions was

analyzed. The use of such multi-component configurations allowed for the investigation of the influence of the coating material on the spatial localization of the electromagnetic field and the optical response of the nanopore.

Calculation of the electromagnetic field distribution

To analyze the plasmonic response, we performed calculations of the normalized field intensity distribution $\frac{E^2}{E_0^2}$ at an excitation wavelength of 635 nm. The calculations used a realistic three-dimensional nanopore geometry, taking into account the metal coating and dielectric substrate. The main goal of the simulation was to determine the regions of maximum localization of electromagnetic energy near the aperture of the structure.

The calculation results (Figure 46) showed that the excitation of localized surface plasmon modes leads to the formation of intense hot-spot regions near the metal edge of the nanopore. The strongest enhancement of the electromagnetic field is observed immediately near the edge of the aperture, while the intensity rapidly decreases with distance from the metal surface due to the attenuation of the near-field component. Simulations of EM distribution for other nanopore configurations can be found in SI.

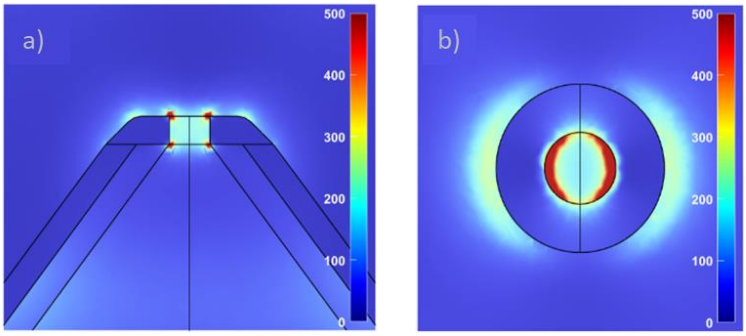

Figure 45 Distribution of electromagnetic field intensity $\frac{E^2}{E_0^2}$ in the plasmon nanopore region[121]

The obtained distributions show that the field localization region has dimensions of the order of several nanometers, which is typical for localized plasmonic resonances. This region determines the efficiency of interaction between molecules and nanoparticles with a plasmonic structure.

In addition, the effect of nanopore shape on the spatial localization of the field was investigated. Structures with concave, straight, and convex wall profiles were compared. Despite the differences in geometry, a hot-spot was formed near the nanopore aperture in all cases. However, the degree of local amplification varied: convex structures exhibited weaker field amplification, while concave and straight geometries provided more effective concentration of electromagnetic energy.

Thus, the shape of the nanopore primarily affects the magnitude of the field enhancement, while the position of the localization region remains virtually unchanged.

The effect of EM field intensity distribution near the metal surface of a nanopore

To see how the dependence of fluorescence enhancement on the distance between the fluorophore and the metal surface changed experimentally, the distributions of the local field and the modification of the decay rate of a dipole placed near a plasmonic nanopore were calculated. This approach allowed us to establish a connection between the spatial localization of the plasmonic near-field and the change in the intensity of the fluorescence signal detected experimentally.

The simulation was performed using a frequency-domain solver. The 3D configuration used a metal-coated plasmonic nanopore that corresponded to the experimental structure. A 635 nm wavelength was used to excite the system. The main objective was to determine the distribution of the local electromagnetic field near the nanopore aperture and analyze the interaction of the fluorophore with the plasmonic hot-spot region, where the EM field is highly localized.

To simulate the emission of a fluorescent source, an electric point dipole was placed inside the nanopore at nominal distances of 3, 6, and 9 nm from the metal wall of the nanopore. For each configuration, the total power dissipated by the dipole in the presence of the plasmonic structure was calculated. The power was determined by integrating the Poynting vector over the surface of a small sphere with a radius of 1 nm, centered at the position of the dipole:

$$S = \oint \mathbf{S} \cdot d\mathbf{A} \qquad (31)$$

where **S** is the Poynting vector and the integration is performed over the closed surface surrounding the dipole.

The total dipole power calculated in the presence of the nanopore was compared with that of the same dipole in a homogeneous medium without the metal nanostructure. The ratio of these two quantities gives the change in the total decay rate of the dipole near the nanostructure:

$$\frac{\Gamma}{\Gamma_0} = \frac{S}{S_0} \qquad (32)$$

where S is the total dipole power in the presence of the nanopore and S_0 is the total dipole power of the same source in a homogeneous environment. Calculations were performed for three mutually orthogonal dipole orientations, with the dipole moment aligned along the x, y, and z axes. The final value of the decay-rate modification was obtained by averaging the results for the three dipole orientations.

The calculations were performed for three mutually orthogonal dipole orientations corresponding to the directions along the x, y, and z axes. The final value of the decay rate modification was determined by averaging the results for all three dipole moment orientations.

Thus, the calculations showed that at the minimum distance between the fluorophore and the metal, the molecule is located in the area of the most intense near-field. However, due to the highly localized EM field, the contribution of non-radiative losses associated with energy transfer to the metal surface increases dramatically. As a result, instead of enhancing the signal, partial quenching of fluorescence is observed.

As the distance increases to ~6 nm, the influence of non-radiative processes decreases, while the intensity of the local electromagnetic field remains relatively high. In this configuration, the maximum enhancement of the fluorescence signal is observed. As the fluorophore moves further away from the metal surface, the near-field rapidly weakens due to the spatial attenuation of the plasmonic field, resulting in a decrease in fluorescence enhancement.

The obtained values of the modification of the total decay rate decreased from ~105 for a distance of 3 nm to ~47 for 6 nm and ~27 for 9 nm, indicating a gradual weakening of the interaction between the dipole and the metal surface as the distance from the nanopore wall increased.

It should be noted that the calculated value characterizes the change in the total decay rate and cannot be directly interpreted as a fluorescence enhancement or quenching factor. However, significantly higher values of decay-rate modification at small distances indicate an increase in non-radiative losses near the metal surface and are qualitatively consistent with the experimentally observed fluorescence suppression for the minimum DNA spacer length.

Thus, the performed modeling allowed us to explain the experimentally observed dependence of fluorescence enhancement on the distance between the fluorophore and the plasmonic surface. The results show that the maximum signal enhancement is determined by the balance between the local enhancement of the electromagnetic field and the increase in non-radiative losses near the metal.

Photo-thermal effects

The plasmonic excitation of the nanopore not only leads to an intense distribution of the EM field, but also inevitably results in thermal heating. The absorption of electromagnetic radiation by the gold-coated nanopore resulted in the local conversion of energy into heat and the formation of temperature gradients near the nanopore walls. The heating regions coincided spatially with the plasmonic hot-spot regions, and the photo-thermal effects inevitably influenced the optical response and behavior of the objects within the nanopore region.

Excitation with a wavelength of 635 nm resulted in a temperature near the nanopore aperture of approximately 38 °C at an ambient temperature of 20 °C (Figure 47-49). The temperature distribution was calculated for three different geometric configurations of the nanopore: convex, straight, and concave. The comparison of the results showed that the geometry of the structure affects not only the distribution of the electromagnetic field, but also the spatial localization of photo-thermal heating in the nanopore hot-spot.

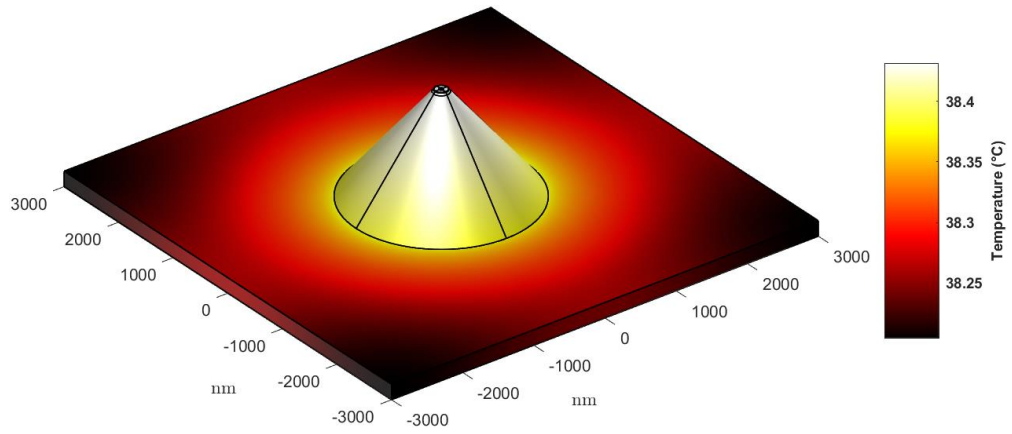

Figure 46 Simulated temperature distribution at λ = 634 nm for plasmonic nanopores (straight)

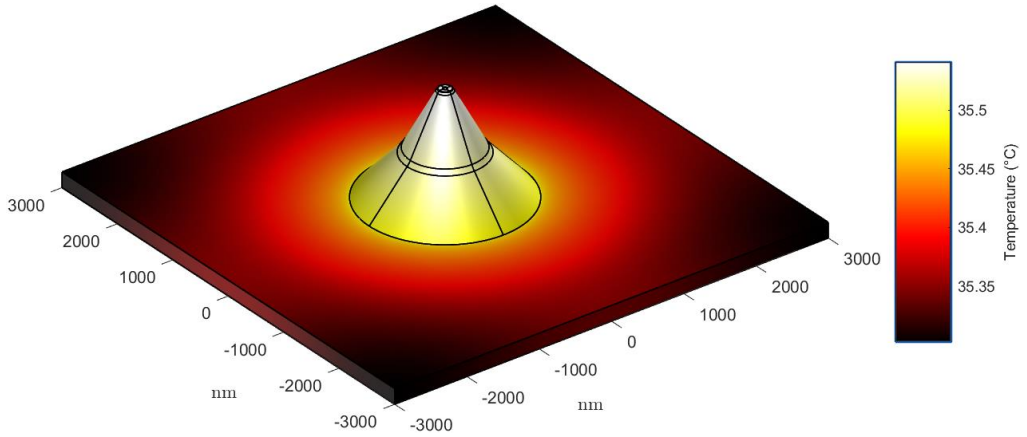

Figure 47 Simulated temperature distribution at λ = 634 nm for plasmonic nanopores (concave)

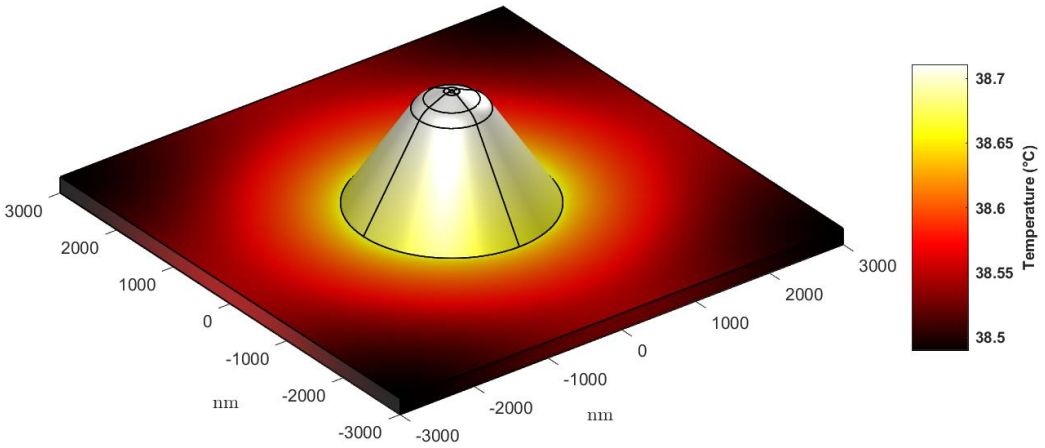

Figure 48 Simulated temperature distribution at λ = 634 nm for plasmonic nanopores (convex)

The obtained temperature distributions are shown in Figures 47-49. These figures demonstrate that the heating is non-uniform and spatially correlated with the localization region of the electromagnetic hot-spot. As expected, the maximum temperature is observed near the nanopore aperture, gradually decreasing with distance from the central region of the structure. Despite the relatively small change in the average temperature of the system, significant local temperature gradients are formed in the immediate vicinity of the metal surface due to the intense absorption of electromagnetic energy by the metal coating.

Comparing different nanopore shapes, it can be said that for straight and convex geometries, there is a more pronounced localization of temperature in the aperture region. In the case of a concave configuration, the thermal distribution becomes more spatially extended. This is due to the difference in the localization of plasmon modes and the distribution of the density of absorbed electromagnetic energy within the structure. Thus, the geometry of the nanopore affects not only the amplification of the electromagnetic field, but also the spatial structure of the thermal field in the nanopore region.

Thus, even moderate local heating can affect the interaction of molecules with the plasmonic surface. Since DNA spacers are sensitive to temperature-induced conformational changes, even a slight change in temperature can lead to a change in the effective distance between the fluorophore and the metal surface, which affects the non-radiative losses. Additionally, the presence of local temperature gradients can alter the transport processes near the nanopore and affect the stability of the interaction between molecular complexes and the plasmonic hot-spot region[121].

Hybrid Au/Si nanopores

The use of hybrid Au/Si nanopores (Figure 50) is particularly interesting because it allows for flexible control over the distribution of the electromagnetic field within the nanopores. While fully metallic nanopores provide strong enhancement of the plasmonic field, resulting in significant non-radiative losses and localized heating, hybrid nanopores create a structure where the plasmonic hot spot is predominantly localized in the Au region, while the Si region influences the redistribution of electromagnetic energy and the transport properties of the system.

The combination of different materials with different optical properties allows for the spatial separation of regions with maximum field enhancement and regions with reduced losses. This approach is particularly important for single-molecule sensing and fluorescence-based applications, where the signal efficiency is determined by the balance between local field enhancement and quenching processes near the metal surface.

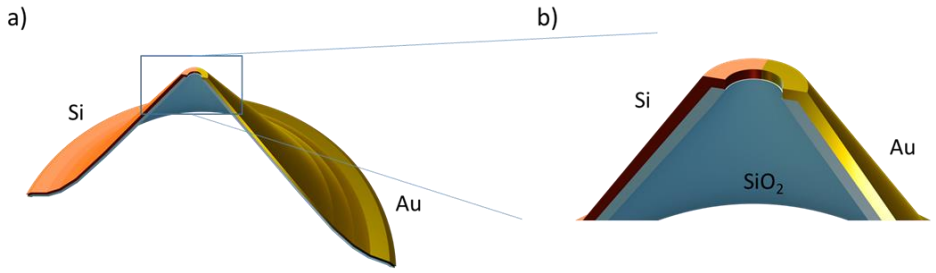

Figure 49 Hybrid plasmonic nanopore[121]

The local field distribution in a hybrid Au/Si nanopore structure was calculated (Figure 51). Figure (a) shows the longitudinal cross-section of the structure, while Figure (b) demonstrates the field distribution in the transverse direction in the aperture region.

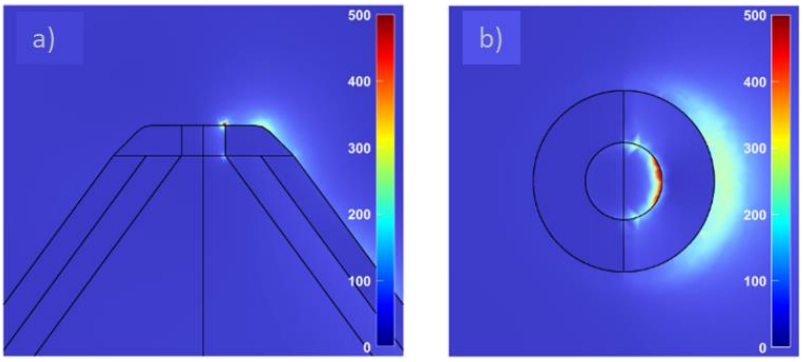

Figure 50 Simulated electric field enhancement $\frac{E^2}{E_0^2}$ at λ = 635 nm for dual-material nanopores. (a, b) Cross-sectional and top-view maps of the field intensity for a dual-material nanopore combining gold and silicon. The near field is asymmetrically localized toward the metallic side, while the dielectric region shows minimal enhancement at this wavelength[121]

The results obtained (Figure 51) show that the enhanced EM field is formed mainly in the area of the gold coating of the nanopore, since the most effective localization of surface plasmon modes

occurs in this place. As one moves away from the plasmonic region, the intensity of the near-field decreases rapidly due to spatial attenuation of the localized plasmonic field.

Indeed, it is observed that the field distribution inside the hybrid structure is spatially asymmetric. The part of the nanopore corresponding to Si is characterized by a significantly weaker field enhancement compared to the Au region. This confirms that the localization of electromagnetic energy in such structures is primarily determined by the metal part of the coating, whereas silicon acts as a material that additionally controls the spatial distribution of the field and photo-thermal effects.

Such asymmetry can potentially contribute to the formation of polarization-dependent optical response and local chiral near-field regions. Even in the absence of explicit chirality in the geometry, the combination of materials with different optical properties can lead to an asymmetric distribution of plasmonic modes near the nanopore walls. As a result, hybrid nanopores can exhibit different responses to circularly polarized light, which can be potentially useful for chirality-sensitive sensing applications.

In summary, the simulations have shown that hybrid Au/Si nanopores can not only localize the electromagnetic field in specific regions, creating spatially asymmetric near-field distributions, but also potentially control the chiral optical response.

5.5 Conclusion

Thus, studies of 3D nanopores have shown that the geometry of the nanopore directly affects the formation of the EM field distribution and, as a result, the temperature distribution and ion current rectification. The greatest localization of plasmonic hot-spots was observed near the nanopore aperture, where the maximum temperature gradients and the most pronounced asymmetry in the ion current distribution were simultaneously formed.

The calculation results confirm that three-dimensional nanopore architectures allow for flexible control of the system's transport properties by modifying the structure's geometry. In particular, convex, straight, and concave configurations exhibited distinct behavior not only in terms of EM field enhancement but also in terms of rectification behavior. This confirms that the spatial shape

of the nanopore directly influences the distribution of ion concentrations, the localization of the field, and the interaction of molecules with the nanopore surface.

In addition, hybrid Au/Si structures were studied, which were found to be capable of forming a spatially asymmetric near-field distribution, which is of interest for heterogeneous optical response and chirality-sensitive sensing. The calculation of fluorescence quenching helps to estimate the optimal distance between the fluorophore and the metal surface, as this distance achieves maximum fluorescence enhancement due to the balance between local field enhancement and non-radiative losses.

Moreover, it has been found that the new 3D nanopore systems are not determined by individual physical mechanisms, but rather by their strong multiphysics coupling. By enhancing the local EM field, the distribution of the thermal gradient is directly influenced, which in turn modifies the processes occurring near the nanopore. The geometry of the nanopore simultaneously determines both the optical confinement and the ionic selectivity of the system. Therefore, even small changes in the geometry or coating material can lead to significant variations in the overall functional response of the nanopore platform.

As a result, the results obtained confirm the need to develop and develop 3D nanopore-based systems for the transition from separate electromagnetic or ion transport models to fully coupled multiphysics approaches, which take into account the mutual influence of optical, thermal, fluidic and transport phenomena. This approach is especially important for the development of next-generation nanopore platforms designed for single-molecule sensing, guided molecular transport, polarization-selective detection, and integration of plasmonic nanopores into hybrid nanophotonic and nanofluidic devices.

6. Conclusions

This work was devoted to a comprehensive study of physical processes in plasmonic and magneto-plasmonic nanopore systems using multiphysics modeling methods. During the modeling process, the geometry of the nanopore, the materials from which it is made, the influence of the geometry on the distribution of the electromagnetic field, photo-thermal effects, ion transport, and the dynamics of processes in the plasmonic hot-spots were comprehensively examined. The results obtained provided a holistic understanding of the behavior of hybrid nanopore platforms under different conditions, highlighting their advantages, disadvantages, limitations, and potential applications.

The main part of the work was devoted to studying magneto-plasmonic trapping of Fe_3O_4@Au core–shell nanoparticles inside a hybrid magneto-plasmonic nanopore. To accomplish this task, a fully coupled multiphysics approach was implemented, which combines the calculation of electromagnetic field distribution, optical trapping, magnetophoretic transport, plasmonic heating, thermophoretic effects, and particle tracing dynamics within a single model. This approach considers the nanopore system as an interconnected multiphysics structure where optics, plasmonics, and magnetism mutually influence each other.

As a result, the calculations performed showed that the trapping dynamics is not only the result of competition between optical force, magnetic force, viscous drag, and thermophoretic transport, but it was also found that the magnetic field is a mechanism for transporting nanoparticles to the nanopore region, and the localized plasmonic near-field is responsible for trapping particles in the hot-spot region near the nanopore walls. Moreover, photo-thermal effects have a critical impact on the stability of the trapping regime and can significantly change the behavior of the system when the laser power is increased.

An additional analysis of nanoparticle trajectories showed that as the laser power increases, there is a simultaneous increase in optical confinement, as well as an inevitable increase in plasmonic heating. As a result, at high powers, there is a competition between conservative trapping and thermally induced transport. It was determined that for small particles, the thermophoretic drift becomes comparable to the trapping forces, critical, and can lead to destabilization of the trapping regime and particle escape from the nanopore hot-spot region. Thus, the simulations showed that

the effectiveness of trapping is determined not only by the magnitude of the optical field enhancement and the particle size, but also by the balance between conservative trapping forces and thermal transport effects.

As the particle size increases, the magnetic and optical forces become stronger, and the trapping potential depth and stability increase. However, small nanoparticles are significantly more sensitive to thermophoretic transport and thermal fluctuations. The results show that the influence of thermal effects becomes particularly critical for trapping small objects, where even moderate temperature gradients can significantly alter the trajectories of particles.

Another part of this work focused on comprehensive analysis of the distribution of the electromagnetic field within three-dimensional nanopore structures featuring different geometries. The simulations carried out revealed the emergence of localized plasmonic hot spots near the structure's aperture, where the highest near-field amplification was noted. It was determined that the spatial confinement of the field depends not only on the nanopore's geometry but also on the material of the nanopore. For hybrid Au/Si nanopores, an asymmetric near-field distribution was observed, resulting from the non-uniform localization of plasmonic modes inside the structure. This results highlight the potential to manipulate the optical response of nanopore systems by changing their geometry and coating composition.

In addition to evaluating the distribution of the electromagnetic field, which directly determines the distribution of absorbed energy within the structure, a study of photo-thermal effects was conducted. The calculations showed that the local plasmonic heating is spatially coincident with the regions of maximum field enhancement, leading to the formation of pronounced temperature gradients in the nanopore region. The results demonstrate that even with a small increase in the average temperature, the local thermal gradients near the metal surface can significantly affect the transport dynamics and the interaction of molecules with the plasmonic surface.

The study of photo-physical processes near the wall of plasmonic nanopores was based on the interaction of fluorophores with a localized near-field. To do this, the total decay rate of a dipole near a metal surface was calculated under the influence of radiation. The results showed that there is an optimal distance between the fluorophore and the plasmonic surface, where the maximum fluorescence enhancement is achieved. However, at the minimum distance from the metal, non-

radiative losses also increase, which is directly related to the dipole-metal coupling. By increasing the distance between the dipole and the metal wall of the nanopore, the contribution of non-radiative losses decreases while maintaining a relatively high local field enhancement. This modeling study provides a physical understanding of the spatial field localization, modification of decay rates, and the experimentally observed fluorescence behavior of three-dimensional plasmonic nanopores.

Another significant result of this work, among analysis of optical and thermal phenomena, is investigation of ionic transport properties in three-dimensional nanopore structures with different geometries. The provided calculations of ionic current rectification revealed that the nanopore's shape directly influences the electric field distribution, ion concentration, and their arrangement within the channel, as well as the degree of ionic current rectification. It was shown that altering the nanopores' geometry affects the efficiency of ionic current rectification and, at the same time, affects the localization of plasmonic modes within the nanopore region. The findings condirm that transport behavior and optical response in nanopore systems are interconnected structural characteristics.

Thus, the obtained results have shown that three-dimensional plasmonic and magneto-plasmonic nanopores are complex multiphysics systems in which optical, magnetic, thermal, and transport phenomena are closely interconnected and should be considered together when addressing complex problems at the nanoscale. The localization of the electromagnetic field directly determines the spatial distribution of photo-thermal heating, temperature gradients affect transport dynamics and trapping stability, and the geometry of the structure simultaneously controls ionic transport, field localization, and the efficiency of object interaction with the nanopore hot-spot region.

The practical significance of the work lies primarily in contributing to the development of understanding of plasmonic and magneto-plasmonic nanopore platforms and in identifying the factors that limit trapping stability, fluorescence enhancement, and transport efficiency in such structures, which affect the outcome and course of the experimental work. The obtained results can be used in the development of nanopore-based biosensors, fluorescence detection platforms,

nanofluidic devices, single-molecule analysis systems, and platforms for controlled capture of nanoscale objects.

The further development of this topic is directly related to the study of more complex fully coupled models, which take into account the reverse effect of trapped nanoparticles on the distribution of the electromagnetic field and temperature, collective effects in the interaction of multiple particles, as well as the influence of hydrodynamic flows and Brownian dynamics in real nanopore environments. Additional interest is represented by the study of chiral and polarization-selective nanopore architectures, as well as the integration of magneto-plasmonic nanopores into next-generation hybrid nanophotonic and nanofluidic systems.

References

1. He, Y., Tsutsui, M., Zhou, Y. & Miao, X. S. Solid-state nanopore systems: from materials to applications. *NPG Asia Materials 2021 13:1* **13**, 48- (2021).
2. Fried, J. P., Wu, Y., Tilley, R. D. & Gooding, J. J. Optical Nanopore Sensors for Quantitative Analysis. *Nano Lett.* **22**, 869–880 (2022).
3. Siwy, Z. S. Ion-current rectification in nanopores and nanotubes with broken symmetry. *Adv. Funct. Mater.* **16**, 735–746 (2006).
4. Single molecule sensing with solid-state nanopores: novel materials, methods, and applications - Chemical Society Reviews (RSC Publishing) DOI:10.1039/C2CS35286A. https://pubs.rsc.org/en/content/articlehtml/2013/cs/c2cs35286a.
5. Xue, L. *et al.* Solid-state nanopore sensors. *Nature Reviews Materials 2020 5:12* **5**, 931–951 (2020).
6. Guo, Z., Zhao, T. S. & Shi, Y. Generalized hydrodynamic model for fluid flows: From nanoscale to macroscale. *Physics of Fluids* **18**, (2006).
7. Haque, F., Li, J., Wu, H. C., Liang, X. J. & Guo, P. Solid-state and biological nanopore for real-time sensing of single chemical and sequencing of DNA. *Nano Today* **8**, 56–74 (2013).
8. Mayer, S. F., Cao, C. & Dal Peraro, M. Biological nanopores for single-molecule sensing. *iScience* **25**, 104145 (2022).
9. Shrikrishna, N. S. & Gandhi, S. Nanopore-based sensing for biomarker detection: from fundamental principles to translational diagnostics. *Journal of Nanobiotechnology 2025 23:1* **23**, 663- (2025).
10. Miles, B. N. *et al.* Single molecule sensing with solid-state nanopores: novel materials, methods, and applications. *Chem. Soc. Rev.* **42**, 15–28 (2012).
11. Chen, Q. & Liu, Z. Fabrication and Applications of Solid-State Nanopores. *Sensors 2019, Vol. 19, Page 1886* **19**, 1886 (2019).
12. He, Y., Tsutsui, M., Zhou, Y. & Miao, X. S. Solid-state nanopore systems: from materials to applications. *NPG Asia Materials 2021 13:1* **13**, 48- (2021).
13. Liu, M., Li, J. & Tan, C. S. Unlocking the Power of Nanopores: Recent Advances in Biosensing Applications and Analog Front-End. *Biosensors 2023, Vol. 13, Page 598* **13**, 598 (2023).

14. He, S. *et al.* Solid-State nanopore DNA Sequencing: Advances, challenges and prospects. *Coord. Chem. Rev.* **510**, 215816 (2024).
15. Xu, H. *et al.* Study of the influence of pore size on the occurrence characteristics and interphase microscopic mechanisms of fluid under the confined effect of nanopores. *Physics of Fluids* **37**, (2025).
16. Tagliazucchi, M. & Szleifer, I. Transport mechanisms in nanopores and nanochannels: can we mimic nature? *Materials Today* **18**, 131–142 (2015).
17. Lin, C. Y. *et al.* Modulation of Charge Density and Charge Polarity of Nanopore Wall by Salt Gradient and Voltage. *ACS Nano* **13**, 9868–9879 (2019).
18. Wang, D. & Wang, G. Dynamics of ion transport and electric double layer in single conical nanopores. *Journal of Electroanalytical Chemistry* **779**, 39–46 (2016).
19. Yao, Y., Wen, C., Pham, N. H. & Zhang, S. L. On Induced Surface Charge in Solid-State Nanopores. *Langmuir* **36**, 8874–8882 (2020).
20. Lan, W. J. *et al.* Voltage-Rectified Current and Fluid Flow in Conical Nanopores. *Acc. Chem. Res.* **49**, 2605–2613 (2016).
21. Han, W. & Chen, X. A review: applications of ion transport in micro-nanofluidic systems based on ion concentration polarization. *Journal of Chemical Technology and Biotechnology* **95**, 1622–1631 (2020).
22. Gilboa, T. & Meller, A. Optical sensing and analyte manipulation in solid-state nanopores. *Analyst* **140**, 4733–4747 (2015).
23. Zhang, J. & Zhang, L. Nanostructures for surface plasmons. *Advances in Optics and Photonics, Vol. 4, Issue 2, pp. 157-321* **4**, 157–321 (2012).
24. Shi, X., Verschueren, D. V. & Dekker, C. Active Delivery of Single DNA Molecules into a Plasmonic Nanopore for Label-Free Optical Sensing. *Nano Lett.* **18**, 8003–8010 (2018).
25. Jonsson, M. P. & Dekker, C. Plasmonic Nanopore for Electrical Profiling of Optical Intensity Landscapes. *Nano Lett.* **13**, 1029–1033 (2013).
26. Seo, D., Kim, D., Seo, S., Park, J. & Kim, T. Analyses of Pore-Size-Dependent Ionic Transport in Nanopores in the Presence of Concentration and Temperature Gradients. *ACS Appl. Mater. Interfaces* **15**, 2409–2418 (2022).
27. Liu, J. *et al.* The evolutionary strategies for enhanced nanopore sensing. *TrAC Trends in Analytical Chemistry* **201**, 118837 (2026).

28. Ying, Y. L. *et al.* Nanopore-based technologies beyond DNA sequencing. *Nature Nanotechnology 2022 17:11* **17**, 1136–1146 (2022).
29. Goto, Y., Akahori, R. & Yanagi, I. Challenges of Single-Molecule DNA Sequencing with Solid-State Nanopores. *Adv. Exp. Med. Biol.* **1129**, 131–142 (2019).
30. Davenport, M. *et al.* The Role of Pore Geometry in Single Nanoparticle Detection. *ACS Nano* **6**, 8366–8380 (2012).
31. Maugi, R. *et al.* A methodology for characterising nanoparticle size and shape using nanopores. *Nanoscale* **12**, 262–270 (2019).
32. Arjmandi, N., Van Roy, W., Lagae, L. & Borghs, G. Measuring the Electric Charge and Zeta Potential of Nanometer-Sized Objects Using Pyramidal-Shaped Nanopores. *Anal. Chem.* **84**, 8490–8496 (2012).
33. Roozbahani, G. M., Chen, X., Zhang, Y., Wang, L. & Guan, X. Nanopore Detection of Metal Ions: Current Status and Future Directions. *Small Methods* **4**, 2000266 (2020).
34. Bacri, L. *et al.* Dynamics of Colloids in Single Solid-State Nanopores. *Journal of Physical Chemistry B* **115**, 2890–2898 (2011).
35. Luo, J., Remy, A. & Zhang, Y. Iontronic Devices from Biological Nanopores to Artificial Systems: Emerging Applications and Future Perspectives. *Chem. Rev.* **125**, 11840–11877 (2025).
36. Salehirozveh, M., Dehghani, P. & Mijakovic, I. Nanopore-Based Neurotransmitter Detection: Advances, Challenges, and Future Perspectives. *ACS Nano* **19**, 24404–24424 (2025).
37. Heydaryan, K. *et al.* Nanopore/Nanocavity-Based Structures as Surface-Enhanced Raman Spectroscopy (SERS) Platforms. *Plasmonics 2024 20:3* **20**, 1401–1417 (2024).
38. Tada, A., Takeuchi, N., Shoji, K. & Kawano, R. Nanopore Filter: A Method for Counting and Extracting Single DNA Molecules Using a Biological Nanopore. *Anal. Chem.* **95**, 9805–9812 (2023).
39. Ramanathan, A. A., Aqra, M. W. & Al-Rawajfeh, A. E. Recent advances in 2D nanopores for desalination. *Environmental Chemistry Letters 2018 16:4* **16**, 1217–1231 (2018).
40. Tian, X. K. *et al.* Exploring synergistic sintering factors and nanopore regeneration of calcium-based thermochemical energy storage materials. *Solar Energy Materials and Solar Cells* **263**, 112593 (2023).

41. Ying, Y. L., Yang, C. N., Liu, W., Wu, X. Y. & Long, Y. T. Understanding single-molecule reactions using nanopore-based techniques. *Nat. Chem.* **17**, 1450–1461 (2025).
42. Howorka, S. & Siwy, Z. Nanopore analytics: sensing of single molecules. *Chem. Soc. Rev.* **38**, 2360–2384 (2009).
43. Gershow, M. & Golovchenko, J. A. Recapturing and trapping single molecules with a solid-state nanopore. *Nature Nanotechnology 2007 2:12* **2**, 775–779 (2007).
44. Zapata Herrera, M., Aizpurua, J., Kazansky, A. K. & Borisov, A. G. Plasmon Response and Electron Dynamics in Charged Metallic Nanoparticles. *Langmuir* **32**, 2829–2840 (2016).
45. Maier, S. A. & Atwater, H. A. Plasmonics: Localization and guiding of electromagnetic energy in metal/dielectric structures. *J. Appl. Phys.* **98**, (2005).
46. Masson, J. F. Portable and field-deployed surface plasmon resonance and plasmonic sensors. *Analyst* **145**, 3776–3800 (2020).
47. Hartland, G. V. Optical Studies of Dynamics in Noble Metal Nanostructures. *Chem. Rev.* **111**, 3858–3887 (2011).
48. Zayats, A. V. & Smolyaninov, I. I. Near-field photonics: surface plasmon polaritons and localized surfaceplasmons. *Journal of Optics A: Pure and Applied Optics* **5**, S16 (2003).
49. Luo, X., Tsai, D., Gu, M. & Hong, M. Extraordinary optical fields in nanostructures: from sub-diffraction-limited optics to sensing and energy conversion. *Chem. Soc. Rev.* **48**, 2458–2494 (2019).
50. Capolino, F. Theory and Phenomena of Metamaterials (Google eBook). **8**, 974 (2010).
51. Ding, F., Yang, Y., Deshpande, R. A. & Bozhevolnyi, S. I. A review of gap-surface plasmon metasurfaces: Fundamentals and applications. *Nanophotonics* **7**, 1129–1156 (2018).
52. Radziuk, D. & Moehwald, H. Prospects for plasmonic hot spots in single molecule SERS towards the chemical imaging of live cells. *Physical Chemistry Chemical Physics* **17**, 21072–21093 (2015).
53. Taylor, A. B. & Zijlstra, P. Single-Molecule Plasmon Sensing: Current Status and Future Prospects. *ACS Sens.* **2**, 1103–1122 (2017).

54. Weber, W. H. & Ford, G. W. Optical electric-field enhancement at a metal surface arising from surface-plasmon excitation. *Optics Letters, Vol. 6, Issue 3, pp. 122-124* **6**, 122–124 (1981).
55. Le Ru, E. C. & Etchegoin, P. G. Rigorous justification of the |E|4 enhancement factor in Surface Enhanced Raman Spectroscopy. *Chem. Phys. Lett.* **423**, 63–66 (2006).
56. Wang, X., Huang, S. C., Hu, S., Yan, S. & Ren, B. Fundamental understanding and applications of plasmon-enhanced Raman spectroscopy. *Nature Reviews Physics* **2**, 253–271 (2020).
57. Jauffred, L., Samadi, A., Klingberg, H., Bendix, P. M. & Oddershede, L. B. Plasmonic Heating of Nanostructures. *Chem. Rev.* **119**, 8087–8130 (2019).
58. Garoli, D., Yamazaki, H., MacCaferri, N. & Wanunu, M. Plasmonic Nanopores for Single-Molecule Detection and Manipulation: Toward Sequencing Applications. *Nano Lett.* **19**, 7553–7562 (2019).
59. Park, T. H. *et al.* Optical Properties of a Nanosized Hole in a Thin Metallic Film. *ACS Nano* **2**, 25–32 (2008).
60. Murray-Méthot, M. P., Ratel, M. & Masson, J. F. Optical Properties of Au, Ag, and Bimetallic Au on Ag Nanohole Arrays. *Journal of Physical Chemistry C* **114**, 8268–8275 (2010).
61. Baltar Henrique, T. M. C. M., Drozdowicz-Tomsia, K. & Goldys, E. M. Plasmonic Properties of Periodic Arrays of Ag Nanocylinders and Dimers, and the Effects of an Underlying Ag Layer. *The Journal of Physical Chemistry C* **122**, 22083–22093 (2018).
62. Koya, A. N. *et al.* Novel Plasmonic Nanocavities for Optical Trapping-Assisted Biosensing Applications. *Adv. Opt. Mater.* **8**, 1901481 (2020).
63. Roxworthy, B. J. *et al.* Application of plasmonic bowtie nanoantenna arrays for optical trapping, stacking, and sorting. *Nano Lett.* **12**, 796–801 (2012).
64. Belkin, M., Chao, S. H., Jonsson, M. P., Dekker, C. & Aksimentiev, A. Plasmonic Nanopores for Trapping, Controlling Displacement, and Sequencing of DNA. *ACS Nano* **9**, 10598–10611 (2015).
65. Spitzberg, J. D., Zrehen, A., van Kooten, X. F. & Meller, A. Plasmonic-Nanopore Biosensors for Superior Single-Molecule Detection. *Advanced Materials* **31**, (2019).

66. Huang, J. A. *et al.* SERS discrimination of single DNA bases in single oligonucleotides by electro-plasmonic trapping. *Nature Communications 2019 10:1* **10**, 5321- (2019).
67. Kerman, S. *et al.* Raman fingerprinting of single dielectric nanoparticles in plasmonic nanopores. *Nanoscale* **7**, 18612–18618 (2015).
68. Roesel, T., Dahlin, A., Piliarik, M., Fitzpatrick, L. W. & Špačková, B. Label-free single-molecule optical detection. *npj Biosensing 2025 2:1* **2**, 32- (2025).
69. Douaki, A. *et al.* Modular Plasmonic Nanopore for Opto-Thermal Gating. *Adv. Opt. Mater.* **13**, 2402189 (2025).
70. Nicoli, F., Verschueren, D., Klein, M., Dekker, C. & Jonsson, M. P. DNA Translocations through Solid-State Plasmonic Nanopores. *Nano Lett.* **14**, 6917–6925 (2014).
71. Belkin, M. & Aksimentiev, A. Molecular Dynamics Simulation of DNA Capture and Transport in Heated Nanopores. *ACS Appl. Mater. Interfaces* **8**, 12599 (2016).
72. Guo, W., Tian, Y. & Jiang, L. Asymmetric Ion Transport through Ion-Channel-Mimetic Solid-State Nanopores. *Acc. Chem. Res.* **46**, 2834–2846 (2013).
73. Trivedi, M. & Nirmalkar, N. Ion transport and current rectification in a charged conical nanopore filled with viscoelastic fluids. *Sci. Rep.* **12**, 2547 (2022).
74. Van Den Berg, A., Craighead, H., Yang, P., Siwy, Z. S. & Howorka, S. Engineered voltage-responsive nanopores. *Chem. Soc. Rev.* **39**, 1115–1132 (2010).
75. Liu, Z., Zhang, Z. & Liu, G. Electrokinetic ion rectification in the coupling asymmetric charged nanochannel. *Electrochim. Acta* **460**, 142568 (2023).
76. Lanzavecchia, G. Customized 3D Nanopore Fabrication for Advanced Electrical and Optical Applications.
77. Wang, J., Zhang, M., Zhai, J. & Jiang, L. Theoretical simulation of the ion current rectification (ICR) in nano-pores based on the Poisson–Nernst–Planck (PNP) model. *Physical Chemistry Chemical Physics* **16**, 23–32 (2013).
78. Sapunova, A. *et al.* Investigation of ion transport in solid-state nanopores with different properties using COMSOL modeling. 100 (2024) doi:10.1117/12.3022400.
79. Guo, W., Tian, Y. & Jiang, L. Asymmetric Ion Transport through Ion-Channel-Mimetic Solid-State Nanopores. *Acc. Chem. Res.* **46**, 2834–2846 (2013).
80. Cheng, L. J. & Guo, L. J. Ionic Current Rectification, Breakdown, and Switching in Heterogeneous Oxide Nanofluidic Devices. *ACS Nano* **3**, 575–584 (2009).

81. Lan, W. J. *et al.* Voltage-Rectified Current and Fluid Flow in Conical Nanopores. *Acc. Chem. Res.* **49**, 2605–2613 (2016).
82. Rezaei, M., Azimian, A. R. & Semiromi, D. T. The surface charge density effect on the electro-osmotic flow in a nanochannel: a molecular dynamics study. *Heat and Mass Transfer 2014 51:5* **51**, 661–670 (2014).
83. Tseng, S., Li, Y. M., Lin, C. Y. & Hsu, J. P. Salinity gradient power: influences of temperature and nanopore size. *Nanoscale* **8**, 2350–2357 (2016).
84. Roy, Y., Warsinger, D. M. & Lienhard, J. H. Effect of temperature on ion transport in nanofiltration membranes: Diffusion, convection and electromigration. *Desalination* **420**, 241–257 (2017).
85. Maccaferri, N., Vavassori, P. & Garoli, D. Magnetic control of particle trapping in a hybrid plasmonic nanopore. *Appl. Phys. Lett.* **118**, 193102 (2021).
86. Timonen, J. V. I. & Grzybowski, B. A. Tweezing of Magnetic and Non-Magnetic Objects with Magnetic Fields. *Advanced Materials* **29**, 1603516 (2017).
87. Ku, J. *et al.* Accurate calculation of major forces acting on magnetic particles in a high-gradient magnetic field: A 3D finite element analysis. *Powder Technol.* **394**, 767–774 (2021).
88. Maccaferri, N., Vavassori, P. & Garoli, D. Magnetic control of particle trapping in a hybrid plasmonic nanopore. *Appl. Phys. Lett.* **118**, 193102 (2021).
89. Koya, A. N. *et al.* Plasmonic Janus particles: A perspective on optical manipulation and biomedical applications. *J. Appl. Phys.* **137**, 210901 (2025).
90. Chen, Y. *et al.* Magnetic nanomaterials for hyperthermia-based therapy and controlled drug delivery. *Bioact. Mater.* **53**, 591 (2025).
91. Franco, A. & E Silva, F. C. High temperature magnetic properties of cobalt ferrite nanoparticles. *Appl. Phys. Lett.* **96**, (2010).
92. Guo, S. S. *et al.* Analytical model for the magnetic field and force in a magnetophoretic microsystem. *J. Phys. D Appl. Phys.* **39**, 1724 (2006).
93. Lim, J. *et al.* Magnetophoresis of Nanoparticles. *ACS Nano* **5**, 217–226 (2010).
94. Hüller, K. The spin wave excitations and the temperature dependence of the magnetization in iron, cobalt, nickel and their alloys. *J. Magn. Magn. Mater.* **61**, 347–358 (1986).

95. Van Vleck, J. H. A Survey of the Theory of Ferromagnetism. *Rev. Mod. Phys.* **17**, 27 (1945).
96. Aharoni, Amikam. Introduction to the theory of ferromagnetism. 319 (2000).
97. Getzlaff, M. Fundamentals of magnetism. *Fundamentals of Magnetism* 1–387 (2008) doi:10.1007/978-3-540-31152-2/SAVE-RESEARCH.
98. Mori, H. & Kawasaki, K. Theory of Dynamical Behaviors of Ferromagnetic Spins. *Progress of Theoretical Physics* **27**, 529–570 (1962).
99. Blundell, Stephen; Magnetism in condensed matter 2001 Oxford New York Oxford University Press ISBN 0198505922. 2001 (2001).
100. Stoner, E. C. Ferromagnetism. *Reports on Progress in Physics* **11**, 43 (1947).
101. Skomski, R. Simple Models of Magnetism (Oxford Graduate Texts). 336 (2008).
102. Khan, P. *et al.* Characterisation and Manipulation of Polarisation Response in Plasmonic and Magneto-Plasmonic Nanostructures and Metamaterials. *Symmetry 2020, Vol. 12, Page 1365* **12**, 1365 (2020).
103. Chen, C. *et al.* Enhanced Optical Trapping and Arrangement of Nano-Objects in a Plasmonic Nanocavity. *Nano Lett.* **12**, 125–132 (2011).
104. Spitzberg, J. D., Zrehen, A., van Kooten, X. F. & Meller, A. Plasmonic-Nanopore Biosensors for Superior Single-Molecule Detection. *Advanced Materials* **31**, 1900422 (2019).
105. Jauffred, L., Samadi, A., Klingberg, H., Bendix, P. M. & Oddershede, L. B. Plasmonic Heating of Nanostructures. *Chem. Rev.* **119**, 8087–8130 (2019).
106. Ciraulo, B., Garcia-Guirado, J., de Miguel, I., Ortega Arroyo, J. & Quidant, R. Long-range optofluidic control with plasmon heating. *Nature Communications 2021 12:1* **12**, 2001- (2021).
107. Zheng, F. Thermophoresis of spherical and non-spherical particles: a review of theories and experiments. *Adv. Colloid Interface Sci.* **97**, 255–278 (2002).
108. Piazza, R. Thermophoresis : moving particles with thermal gradients. *Soft Matter* **4**, 1740–1744 (2008).
109. Rikken, R. S. M. *et al.* Manipulation of micro- and nanostructure motion with magnetic fields. *Soft Matter* **10**, 1295–1308 (2014).

110. Cherry, E. M., Maxim, P. G. & Eaton, J. K. Particle size, magnetic field, and blood velocity effects on particle retention in magnetic drug targeting. *Med. Phys.* **37**, 175–182 (2010).
111. Guimarães, A. P. Magnetism of small particles. *NanoScience and Technology* 71–124 (2017) doi:10.1007/978-3-319-59409-5_3/SAVE-RESEARCH.
112. Clime, L., Le Drogoff, B., Zhao, S., Zhang, Z. & Veres, T. Magnetic nanocarriers: From material design to magnetic manipulation. *Int. J. Nanotechnol.* **5**, 1268–1305 (2008).
113. Kuppe, C., Rusimova, K. R., Ohnoutek, L., Slavov, D. & Valev, V. K. "Hot" in Plasmonics: Temperature-Related Concepts and Applications of Metal Nanostructures. *Adv. Opt. Mater.* **8**, 1901166 (2020).
114. Jones, S., Andrén, D., Karpinski, P. & Käll, M. Photothermal Heating of Plasmonic Nanoantennas: Influence on Trapped Particle Dynamics and Colloid Distribution. *ACS Photonics* **5**, 2878–2887 (2018).
115. Monisha, K., Suresh, K. & George, S. D. Colloidal Manipulation through Plasmonic and Non-plasmonic Laser-Assisted Heating. *Laser Photon. Rev.* **17**, 2300303 (2023).
116. COMSOL - Software for Multiphysics Simulation. https://www.comsol.com/.
117. Salihov, S. V. *et al.* Recent advances in the synthesis of Fe3O4@AU core/shell nanoparticles. *J. Magn. Magn. Mater.* **394**, 173–178 (2015).
118. Arima, A. Recent advances in single-particle analysis with nanopore technology. *Analytical Sciences 2025 41:5* **41**, 677–685 (2025).
119. He, S. *et al.* Solid-State Nanopore Single-Molecule Capture: Advances and Challenges. *Small* **21**, e07736 (2025).
120. Melzer, J. E. & McLeod, E. Fundamental Limits of Optical Tweezer Nanoparticle Manipulation Speeds. *ACS Nano* **12**, 2440–2447 (2018).
121. Lanzavecchia, G. *et al.* Three-dimensional plasmonic nanopores for DNA-PAINT and dual-material Au/Si architectures. *Journal of Nanobiotechnology 2026* https://doi.org/10.1186/S12951-026-04509-9 (2026) doi:10.1186/S12951-026-04509-9.
122. Lanzavecchia, G. *et al.* Tailored Fabrication of 3D Nanopores Made of Dielectric Oxides for Multiple Nanoscale Applications. *Nano Lett.* **24**, 10098–10105 (2024).

Supporting information

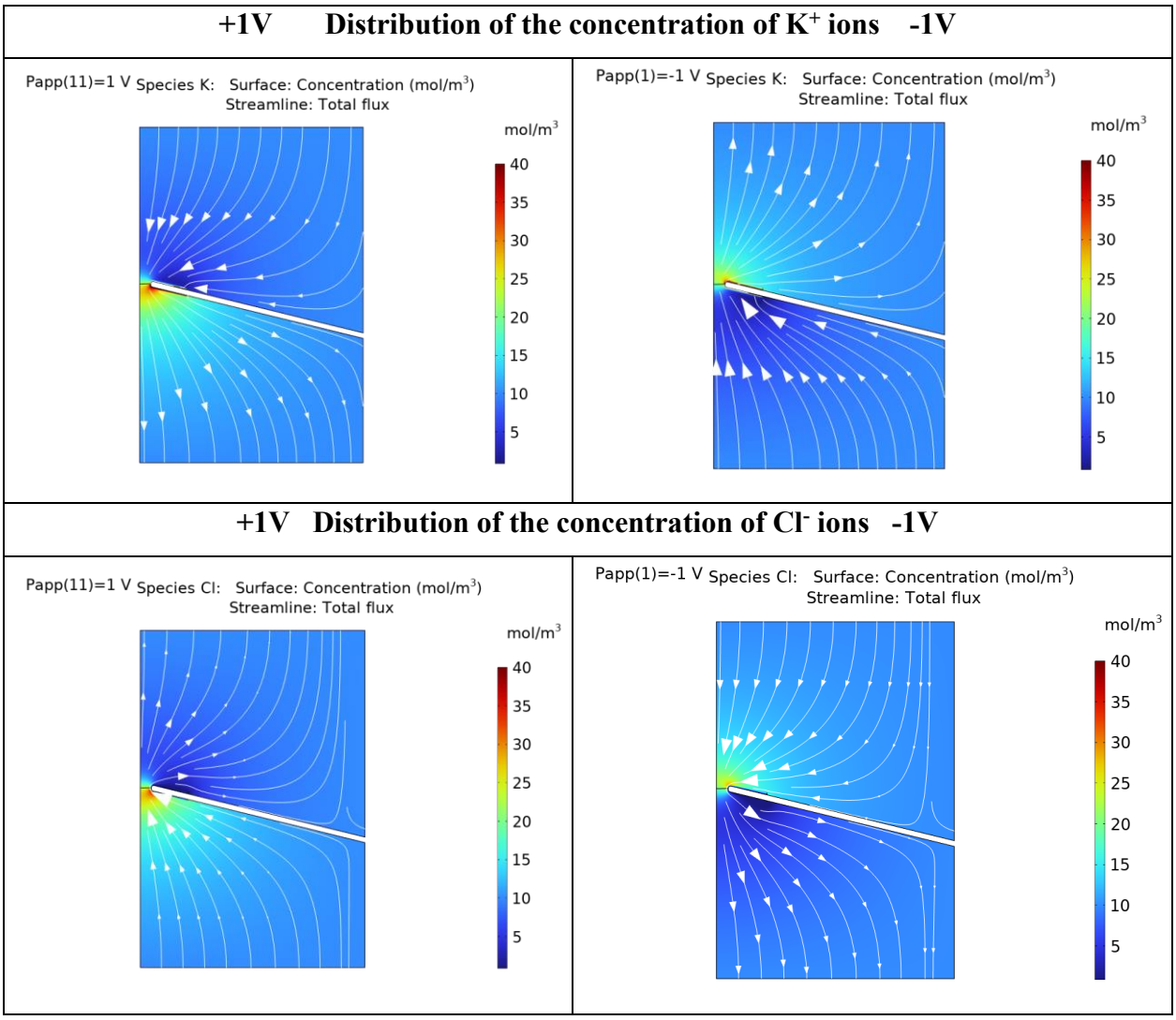

Figure S1. Al_2O_3 convex nanopore. Distribution of the concentration of ions.

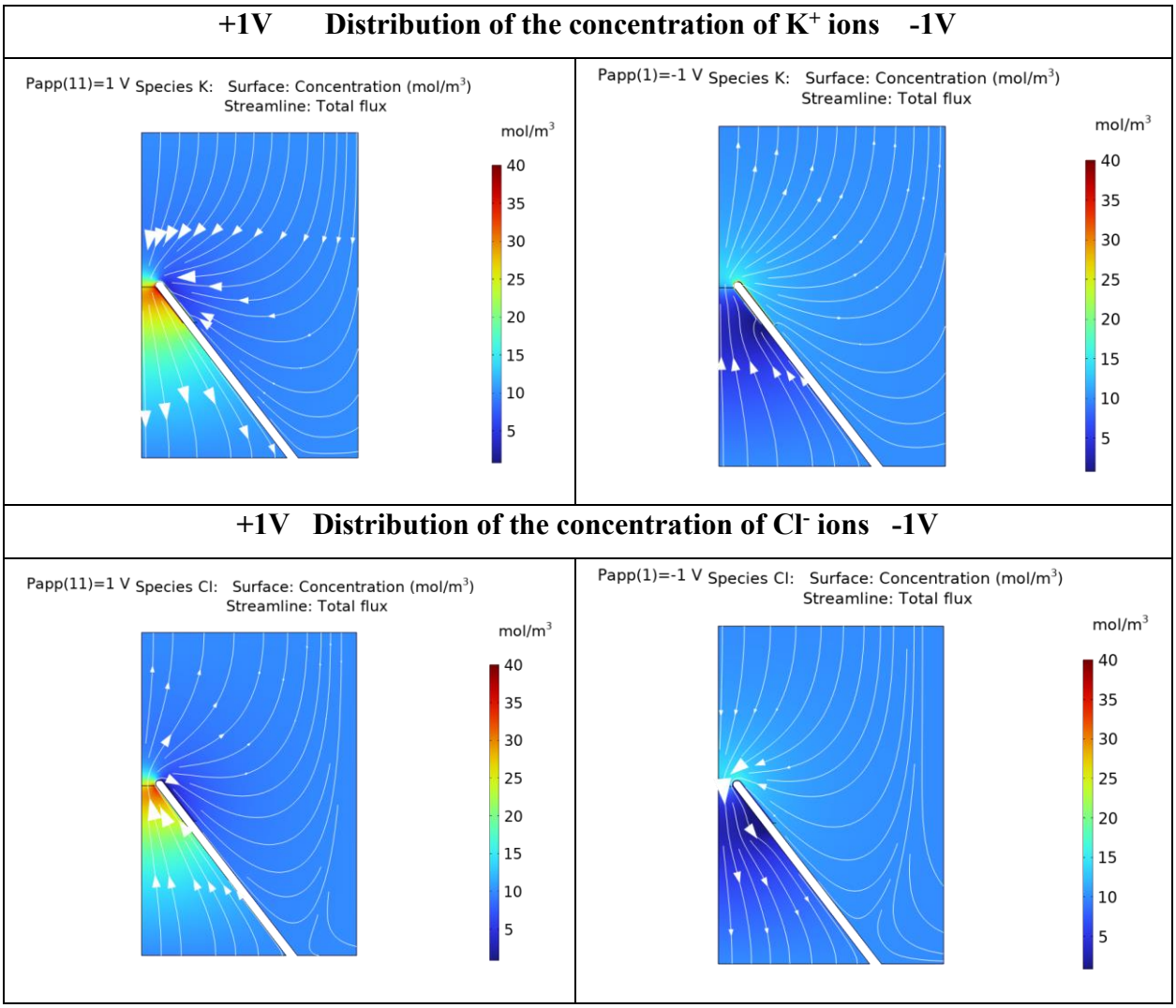

Figure S2. Al_2O_3 straight nanopore. Distribution of the concentration of ions.

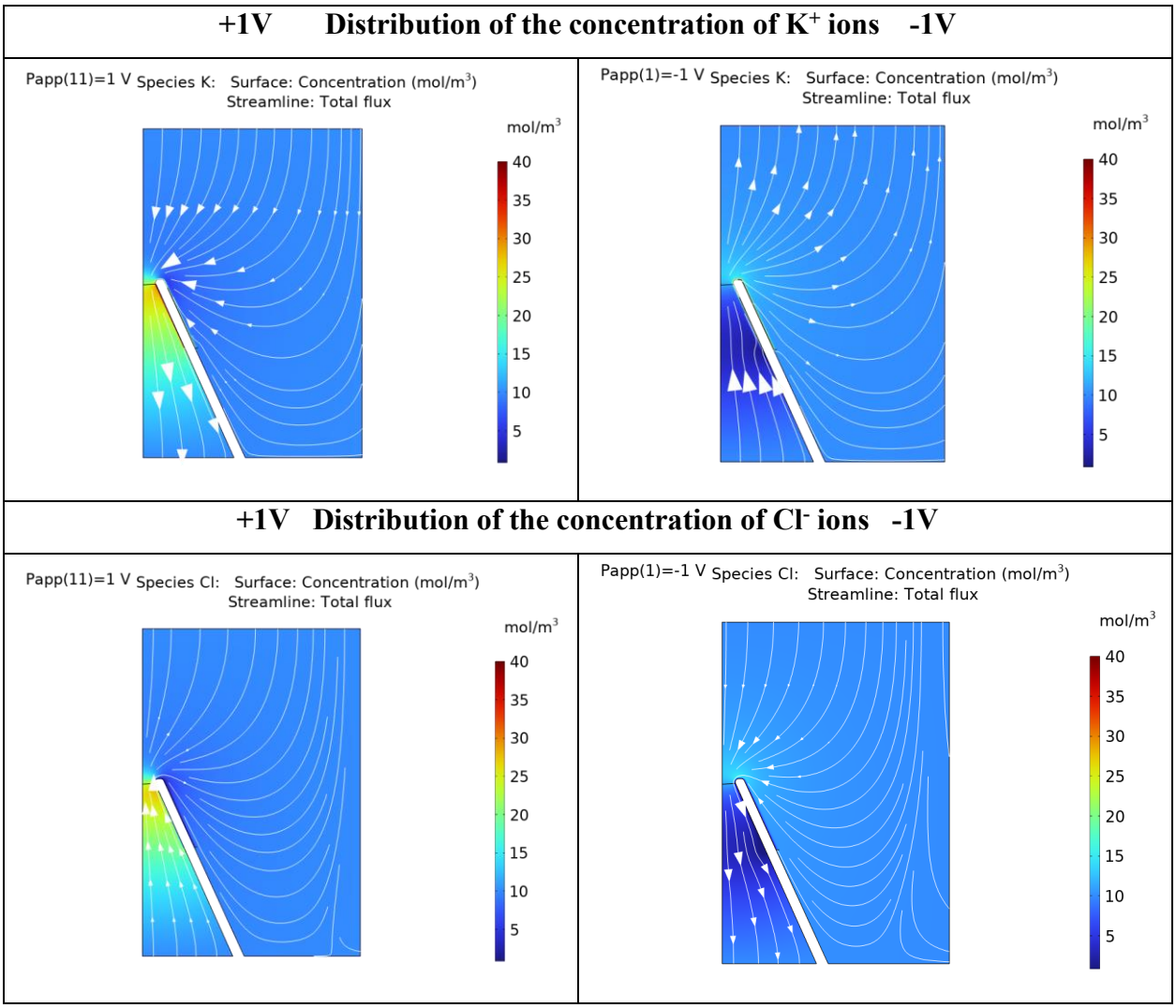

Figure S3. Al_2O_3 concave nanopore. Distribution of the concentration of ions.

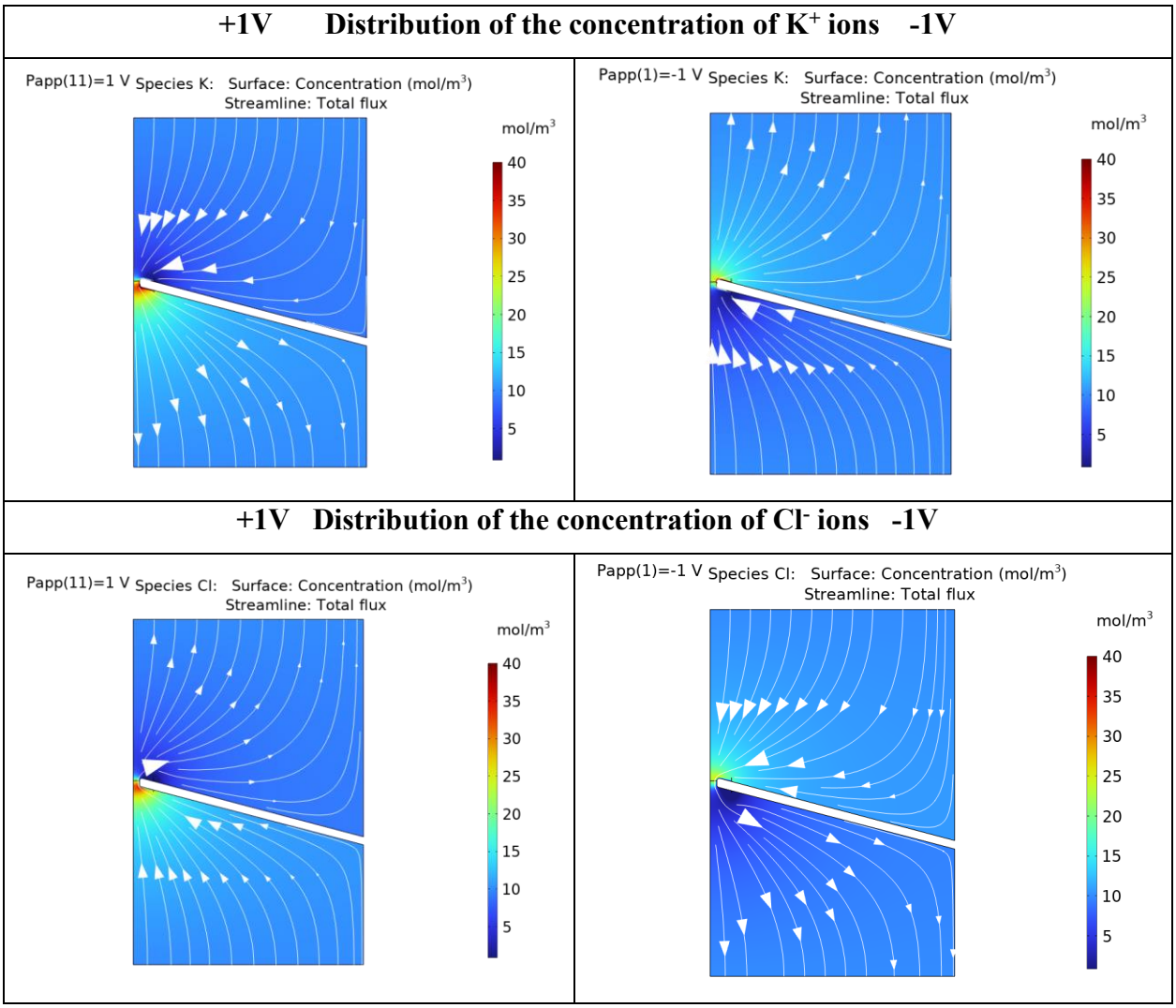

Figure S4. SiO_2 convex nanopore. Distribution of the concentration of ions.

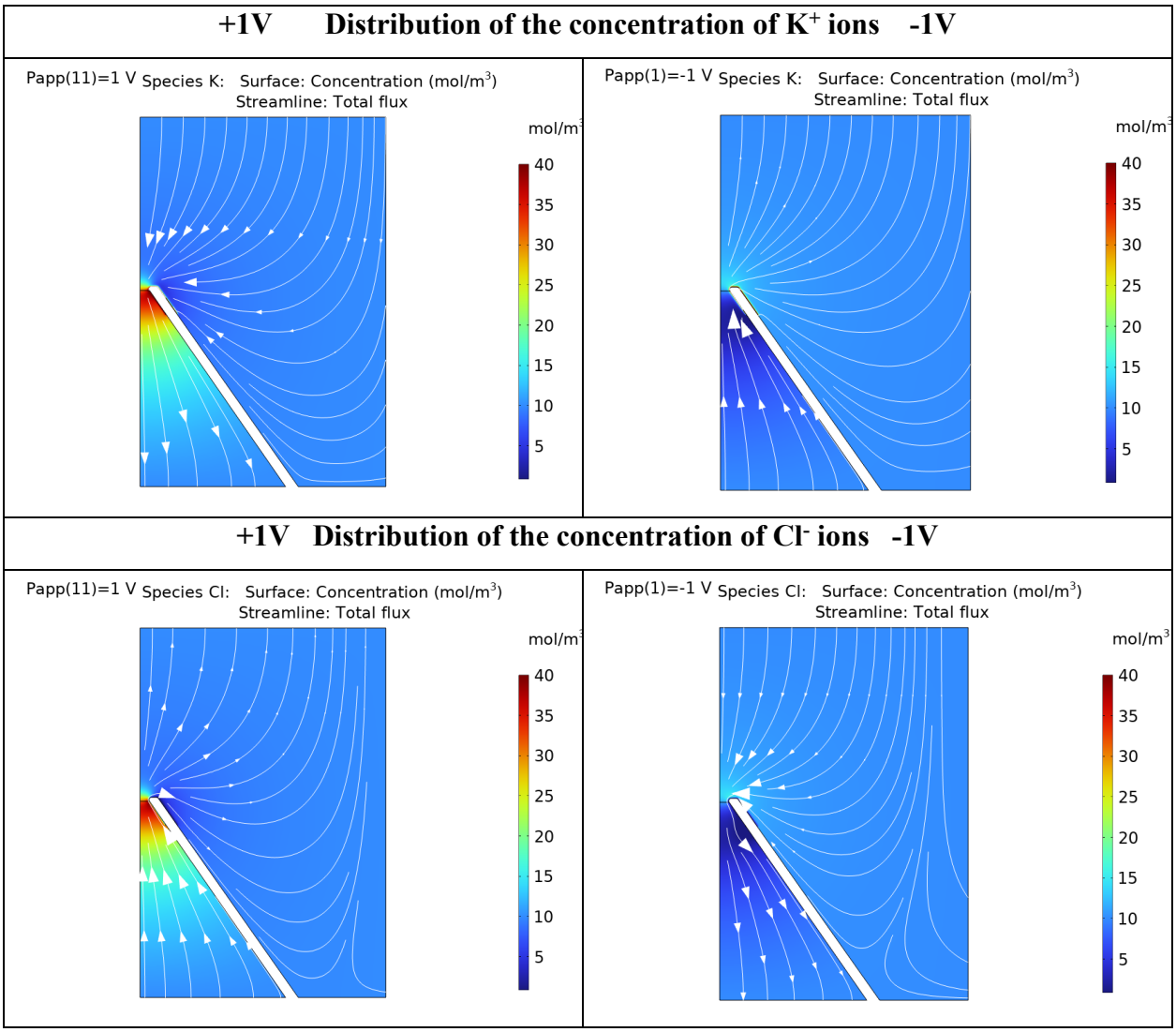

Figure S5. SiO_2 straight nanopore. Distribution of the concentration of ions.

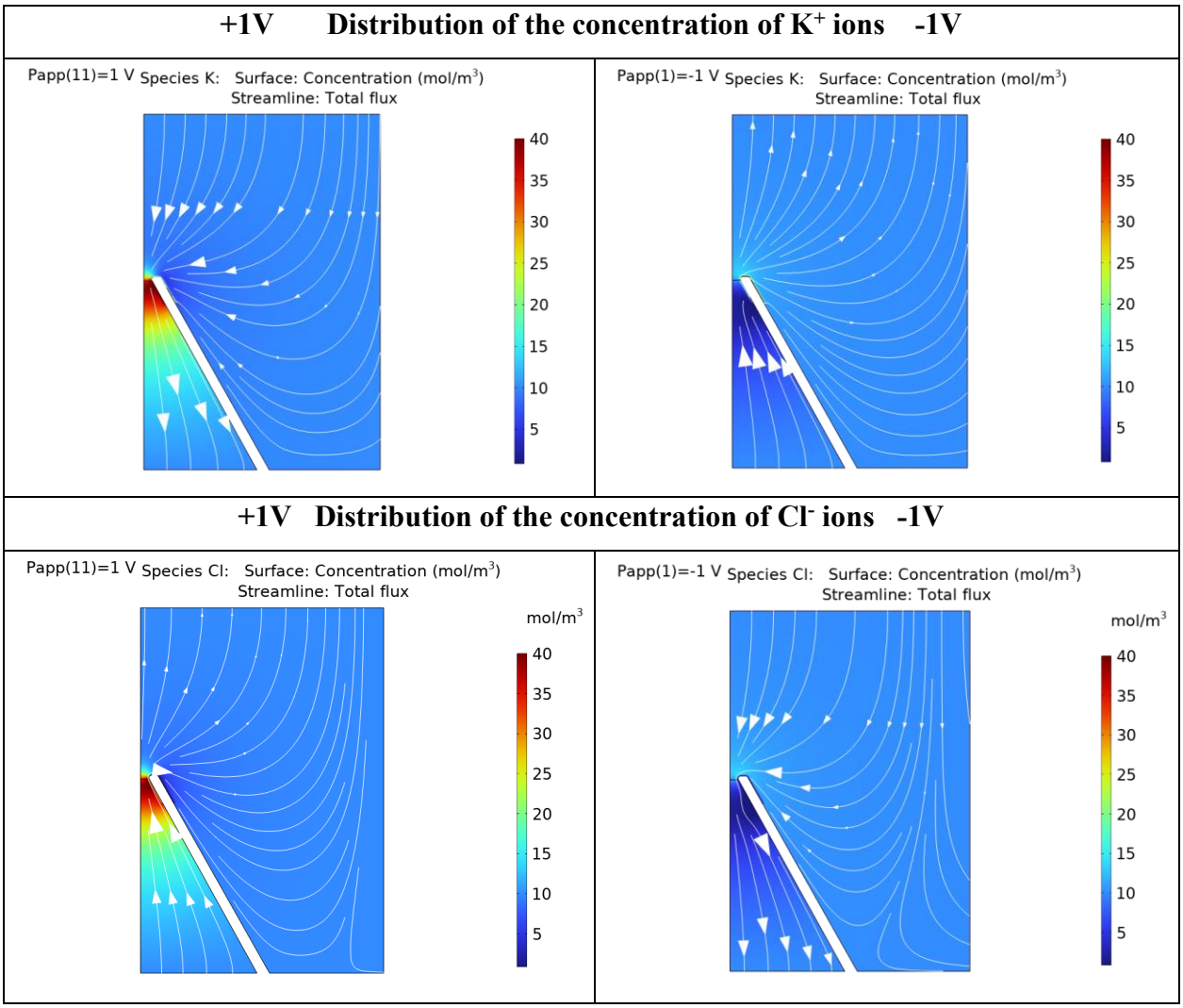

Figure S6. SiO_2 concave nanopore. Distribution of the concentration of ions.

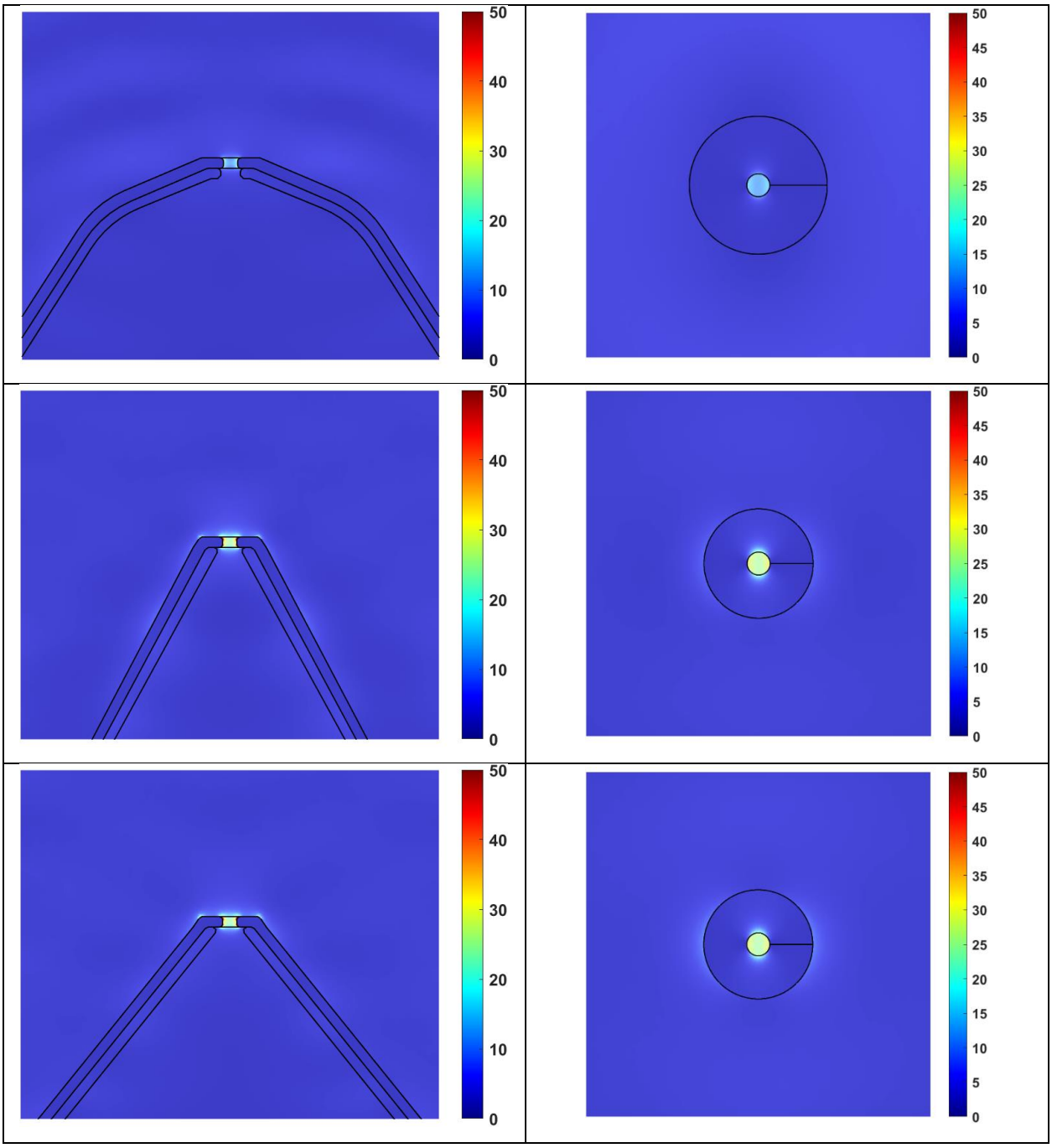

Figure S7. Simulated electric field enhancement ($|E|^2/|E_0|^2$) at λ = 634 nm for plasmonic nanopores. Cross-sectional and top-view maps of the field intensity for a gold-coated conical nanopore with rounded edges. The simulations were performed at λ = 634 nm, a wavelength selected close to the experimental illumination at 640 nm. The mode produces strong, symmetric confinement around the pore, with maximum intensity within a few nanometers from the metal

surface. (c, d) Corresponding maps for a dual-material nanopore combining gold and silicon. The near field is asymmetrically localized toward the metallic side, while the dielectric region shows minimal enhancement at this wavelength.